ELECTRODE EROSION AND ARC STABILITY IN TRANSFERRED ARCS WITH GRAPHITE ELECTRODES

A Thesis by Hongsun Seon

Department of Chemical Engineering
McGill University

Under the Supervision of Prof. R.J. Munz

A thesis submitted to the Faculty of Graduate Studies and Research
of McGill University in partial fulfillment of the requirements
for the degree of Doctor of Philosophy

McGill University
Montreal, Canada

April 2001

0-612-75678-5

ABSTRACT

Arc stability and erosion behavior were studied on a hollow graphite DC cathode in an argon atmosphere at atmospheric pressure. It was found that the arc stability is associated with the electron emission mode transition of the cathode operation. Estimation of current densities, SEM pictures, Fast Fourier Transform (FFT) of total voltage, and measurement of cathode surface temperature supported this. Stable arcs are in the thermionic emission regime while unstable arcs in the thermofield emission regime. Higher argon gas flow rate is believed to cause the shift of the mode from the thermofield emission to the thermionic emission by increasing the arc root temperature through steepening the thermal gradient at the arc root and increasing ionization phenomena inside the arc. Sharp cathode tip geometry usually leads to the thermionic emission while a rounded tip geometry encourages the thermofield emission. For the unstable arcs, the high voltage fluctuation resulted from the jumping of the arc root between different cathode spots and changes in the arc length. In the stable arcs, however, the voltage was almost constant because of the absence of arc jumping. The standard deviation of the voltage was used as the arc stability indicator and was less than 3 V for the stable arc in this transferred arc system.

The erosion rate of the cathode in this work ranged from 0.41 to 2.61 μg/C. At 150 A runs the arc stability strongly influenced the erosion rate; as the arc stability increased, the erosion rate decreased. Higher currents runs (300 and 400 A), however, showed the opposite trend because of the carbon vapor redeposition. The total erosion rates of 150 A runs were separated into the stable (E_s) and the unstable (E_u) erosion rate. The E_u was more than 3 times higher in this work. It is believed that the thermofield emission of the

unstable arcs produced more erosion because of the higher local heat flux to the cathode spots.

Résumé

La stabilité d'un arc électrique en courant continu et son comportement quand à l'érosion des électrodes est étudié sur une cathode creuse de graphite à pression atmosphérique fonctionnant en mode d'arc transféré. Dans notre étude, la stabilité de l'arc est associée à une transition du régime d'émission électronique à la cathode. Ces résultats sont en accord avec les estimations de la densité de courant à la cathode et avec une série de données expérimentales telles les observations par microscopie électronique (SEM), les signaux de tension et leur transformée de Fourrier (FFT), et les mesures de température de surface de la cathode. Les arcs stables fonctionnent en régime d'émission thermionique à la cathode alors que les arcs instables fonctionnent en régime thermo-champ. Un changement du mode d'émission passant du mode thermo-champ vers une émission thermionique est observé pour des débits d'argon plus élevé. Ce changement de régime est attribué à une augmentation de température au pied cathodique de l'arc suite au gradient thermique plus important induits dans cette région, et à une augmentation du phénomène d'ionisation dans la colonne d'arc. Habituellement, une cathode à tige pointue mène vers une émission thermionique, alors qu'un bout à géométrie hémisphérique favorise un régime thermo-champ. Les fluctuations importantes de la tension d'arc dans le cas des arcs instables sont attribués aux sauts du pied d'arc vers différents spots cathodiques d'émission et à des changements dans la longueur de l'arc. La tension d'arc reste cependant essentiellement constante dans le cas d'arcs stables et aucun saut d'arc n'est alors observé. L'écart type sur les fluctuations de tension est utilisé comme indicateur de stabilité de l'arc électrique. Cette écart type est moins de 3 V pour les arcs stables dans le présent système à arc transféré.

Les taux d'érosion de la cathode dans cette étude varient entre 0.41 et 2.61 μg/C. Pour des essais

à 150 A, la stabilité de l'arc influence grandement le taux d'érosion. Le taux d'érosion observé décroit alors lorsque la stabilité de l'arc augmente. Les essais à plus forts courants (300 et 400 A) montrent cependants une tendance inverse attribuée à une re-déposition des vapeurs de carbone. Le taux d'érosion des essais effectués à 150 A sont séparés en taux d'érosion en mode stable (E_s) et instables (E_u). Les valeurs observées durant la période instable (E_u) sont plus du triple des valeurs observées en période stable E_s. L'érosion élevée observé pour les arcs instables opérant en mode thermo-champ est attribué aux flux thermique locaux plus importants au niveau des spots cathodiques.

ACKNOWLEDGMENTS

To Professor R.J. Munz for giving an opportunity to study thermal plasma technology and his supervision with patience.

To Professor J.-L. Meunier for his good introduction course of arc physics and many comments.

To the members of the Chemical Engineering staff: P. Fong, A. Prihoda, J. Terrasi, L. Miller-Aspin, B. Hanley, L. Cusmich, A. Gagnon, W. Greenland, C. Dolan, E. Siliauskaus, B. Habib, and F. Caporuscio.

To the members of the plasma group: Tony Addona, Antonio Carlos da Cruz, Julie Filion, Patrice Nadeau, Munther Kandah, Jorg Oberste-Berghaus, Karen Sum, Sylvain Coulombe, Harbec David, Jun Yu, Alison Hanstead, Honqin Liu, Felipe Aristzabal, and Sakamon Devahastin for the useful discussions.

To summer student Arash Hooshangi for help with the experiments, the SEM analysis, and arc pictures.

To Helen Campbell for help with the SEM analysis.

To Saverio Biunno for help with the oscilloscope analysis.

To the Natural Sciences and Engineering Research Council of Canada for the financial support.

To my father for the love and the support.

To my wife Mihyune for her understanding and caring Minji and Minho.

TABLE OF CONTENTS

LIST OF FIGURES

LIST OF TABLES

CHAPTER I

GENERAL INTRODUCTION

The selection of the right thermal plasma torch is very important for the commercial viability of plasma processes. The designer of thermal plasma furnaces should deal not only with torch efficiency and electrode life but also consider the best combination of torches and furnaces for an application.

This study focuses on hollow graphite DC cathodes which are believed to be one of the most promising torch systems for the treatment of many solid wastes as well metallurgical processing. Their potential advantages include safety, high energy efficiency, compact design, and ease of scale-up.

This work was designed to study the behavior of hollow graphite cathodes including the arc electrical behavior, erosion rate, and the spontaneous transition between thermionic and thermofield electron emission. Although previous work on hollow AC electrodes has been done regarding applications in the metallurgical industries, it was believed that further study of these phenomena is needed for better understanding. The previous work concentrated on overall electrode consumption but did not examine the effects of mode transition. The erosion in at least some of those studies was the result of a combination of chemical reaction and erosion due to arc effects and was complicated by the presence of a metal bath and poorly controlled atmosphere. The present work uses graphite electrodes in a well-controlled atmosphere.

This thesis starts with a literature review on arc cathodic phenomena, considerations of arc stability of hollow graphite electrodes and erosion of graphite electrodes. Industrial applications of hollow graphite electrodes are also included. This is followed by the research objectives and the experimental methods used in this study. Chapter V presents brief thermodynamic study to identify the carbon species expected to be found in the arc atmosphere. Chapter VI on results and discussion first characterizes the arc and examines the emission mode transition. This is followed by an examination of the erosion rates of the cathode and finally the development of a correlation for erosion as a function of operating conditions under stable conditions. The last chapter gives conclusions, recommendations for further work, and contributions to knowledge.

CHAPTER II

LITERATURE REVIEW

2.1. INTRODUCTION

The term “arc stability” here means the absence or the disappearance of acoustical and electrical noise of hollow graphite electrodes used in this work. The disappearance of both types of noise indicates stable arcs, and the appearance of both types of noise means unstable arcs. The arc stability is a cathodic phenomenon and is related to mode transition in arc cathode operation. Maddever et al. (1976) and Sommerville et al. (1987) reported that for hollow graphite electrodes, the arc stability as well as the consumption rate could be controlled by the argon gas flow rate. Higher argon gas flow rate provided stable arcs and lower consumption rates.

Recently Roth (1995) stated that mode transitions, from non-thermal to thermal arcs and spontaneous mode transitions of thermal arcs, is one of the present issues of arc physics and that “the industrial uses of arcs will not be well understood until such time as the physical processes responsible for mode transitions are identified, and the criteria for the onset of mode transitions are understood in a quantitative manner”. Thus this work was designed to further study the mode transitions of thermal arcs using hollow graphite DC cathodes for better understanding of the arc stability. The arc stability is associated with the spontaneous mode transitions. It was also planned to study erosion behavior as a function of the arc stability. The difference between erosion and consumption is that erosion excludes the oxidation and the breakage of graphite electrodes.

In this section, hollow graphite electrodes and their related studies are reviewed. Firstly considerations for arc cathode phenomena connected with this work is introduced. In the next part, typical use of graphite electrodes in electric arc furnaces (EAFs) is given. This is followed by previous work on the arc stability of hollow graphite electrodes. In addition, erosion of graphite electrodes is also included. Finally some industrial applications of hollow graphite DC cathodes are introduced.

2.2. ARC CATHODE PHENOMENA

2.2.1. Modes of High Pressure Arc Cathodes

In this part, characteristics of modes of cathode operation of high pressure arcs, as opposed to vacuum arcs, are introduced because this work has been performed at atmospheric pressure. Guile (1971), Anders et al. (1991), and Coulombe (1997) reviewed the operation modes of high pressure arcs, and a summary, based on their data, about some features of the modes of high pressure arcs is presented in Table 2-1. Coulombe (1997) defined high pressure arcs as arcs in which “the medium is composed of the ambient gas filling the chamber and to some extent, the electrode erosion products”.

According to the review of Anders et al. (1991), the modes of high pressure arcs can be separated into the stationary and the nonstationary mode. The electron emission mechanism of the stationary mode is thermionic emission while that of the nonstationary mode is thermofield or field emission. The cathode electrode materials used for the stationary mode are high boiling point refractory materials, and for the nonstationary mode low-boiling point metals, such as copper and nickel, are used. They are also known as “hot cathode” and “cold cathode”, respectively. Current density of the stationary mode ranges from $10^7 \sim 10^8$ A/m^2 while that of the nonstationary mode ranges from $10^{10} \sim 10^{11}$

Table 2-1: A summary of cathode operation modes of high pressure arcs.

Mode[2]	Stationary	Nonstationary
Mechanism of electron emission [1,2,3]	Thermionic emission	Thermofield or field emission
Type of cathode[1]	Refractory	Low boiling points metals
Typical materials[1]	W, C	Cu
Operating temperature [1]	> 3500 K	Wide range, generally below 3000 K
Current Density[1]	$10^7 \sim 10^8$ A/m^2	$10^{10} \sim 10^{11}$ A/m^2
Number of arc attachment points[3]	One and diffuse over a diameter of some mm	Several and constricted over diameters of 5 ~ 20 μm
Movement of the arc attachment[3]	Fixed or slow	Rapid
Voltage characteristics[2]	No fluctuation	Great fluctuation

Data Sources;

1. Guile (1971), 2. Anders et al. (1991), 3. Coulombe (1997)

A/m^2. For the stationary mode the number of arc attachment points is one, and it is diffuse over a diameter of some mm; however, for the nonstationary mode there are several arc attachment points constricted over diameters of 5 ~ 20 μm. The arc movement in the stationary mode is slow or nonexistent, but in the nonstationary mode the movement is rapid.

Conceptually, the arc attachment points introduced by Coulombe (1997) are the same as the arc roots on arc cathodes. In thermionic emission, the single arc attachment point is the arc root. This is also termed “thermionic spot” by Anders et al. (1991). Hereafter the term “thermionic spot” is used to indicate the arc root in the thermionic emission. Otherwise, in the thermofield emission, the arc attachment points are made of macrospots, and these macrospots are composed of several cathode spots. Due to the different internal structure of the arc attachment points, different behaviors of the arc attachment points are observed. Hereafter the term “cathode spots” is used to point to the spots inside the macrospot in the thermofield emission.

The mode separation is basically related to electron emission mechanisms. In general arc cathodes can emit electrons through thermionic, thermofield, or field emission. Thermionic emission, which occurs when the cathode temperature is high and the field is low, is described by the Richardson-Dushman equation; the effects of intermediate fields on the thermionic emission are known as the Schottky effect which enhances electron emission from the cathode. Field emission occurs when the field is high and the cathode temperature is low, and is described by the Fowler-Nordheim equation. Dolan et al. (1954) reported that when both the cathode temperature and the field are high, the emission process is termed thermofield emission which is an intermediate state between the thermionic and the field emission. Most arcs have been recognized to be in the thermofield emission regime. In thermionic emission, electrons can escape from the electrode surface if they acquire sufficient energy to overcome the energy barrier. The energy is known as the work function. In field emission, electrons can tunnel the barrier because of the higher electric field.

Murphy and Good (1956) developed the generalized electron emission equation, which can be applied to the entire electron emission regimes. The equation shows that electron current density (J_e) is related to temperature, electric field strength and work function as follows:

$$J_e = e\int_{-W_a}^{\infty} D(E_c, W)N(T_c, W)dW \qquad (2\text{-}1)$$

where $D(E_c, W)$ is the emission probability for an electron with energy W, from the cathode surface material submitted to an electric field E_c and the cathode surface temperature T_c . $N(T_c, W)dW$ represents the number of electrons reaching the potential barrier per second and per unit area with energy between W and W+dW. W_a represents potential barrier energy. The Richardson-Dushman equation for the thermionic emission is a limit of the equation (2-1) when the temperature is high and the electric field is low while the Fowler-Nordheim equation for the field emission is also the limit when the temperature is low and the electric field is high. Coulombe et al. (1997) reported that the Murphy and Good equation should be used for the calculation of the thermofield emission current densities in order to increase the accuracy of numerical prediction for the arc-cathode interactions.

Anders and Jütter (1990) studied transition of the cathode mode in high pressure discharge lamps during the starting period. They used tungsten AC electrodes activated by $Ba_2CaW_3O_6$. The transition from the thermofield to the thermionic emission and vice versa is only expected to occur for hot cathodes. Guile (1971) also mentioned this mode transition. Anders and Jütter (1990) reported that the arc of the high pressure discharge lamp was usually in the thermofield emission regime immediately after the glow-to-arc transition in each half-cycle after the initial breakdown as shown in Figure 2-1. The "vapor arc mode" in the figure means the thermofield emission regime. After a time of the order of one second, however, the electrodes were sufficiently heated and thus were operated in the thermionic emission regime. This transition was detected by the sudden disappearance of the burning voltage and the barium line emission noise. The great fluctuations of the arc voltage meant that the electrodes were in the thermofield emission regime.

2.2.2. THE CATHODE REGION

Figure 2-2 shows a schematic representation of the regions of an arc. Roth (1995) defined the cathode region as a region of "potential and density gradients, with an axial extent of perhaps $d_c \approx 1$ mm". This means that the cathode region is not in the local thermodynamic equilibrium (LTE) and is characterized by steep gradients of temperatures, particle densities, and electric field in a very thin layer between the cathode and the arc. In this figure, before the arc column region, Roth (1995) presents three regions, the cathode sheath, the cathode region, and the cathode flow zone. That could be different according to researchers. Some researchers like Zhou et al. (1994) and Coulombe (1997) who performed the modeling work in the cathode region considered the cathode region as the connection region between the cathode and the arc column. For the detailed description of this region, Coulombe (1997) subdivided the cathode region into the cathode sheath zone (or the space charge zone) and the ionization zone (or the

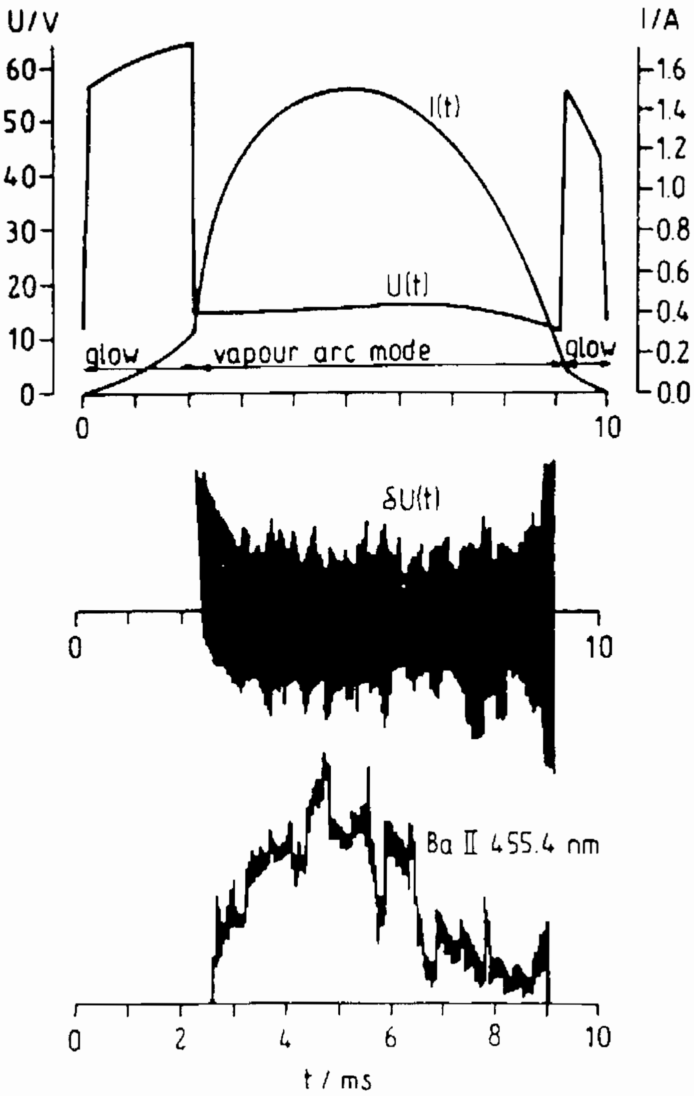

Figure 2-1: Sixth half-cycle of the current I(t), burning voltage U(t), noisy component δU(t) and barium line intensity of an electrode of a 70 W high-pressure sodium discharge lamp after the initial breakdown (Anders and Jütter 1990).

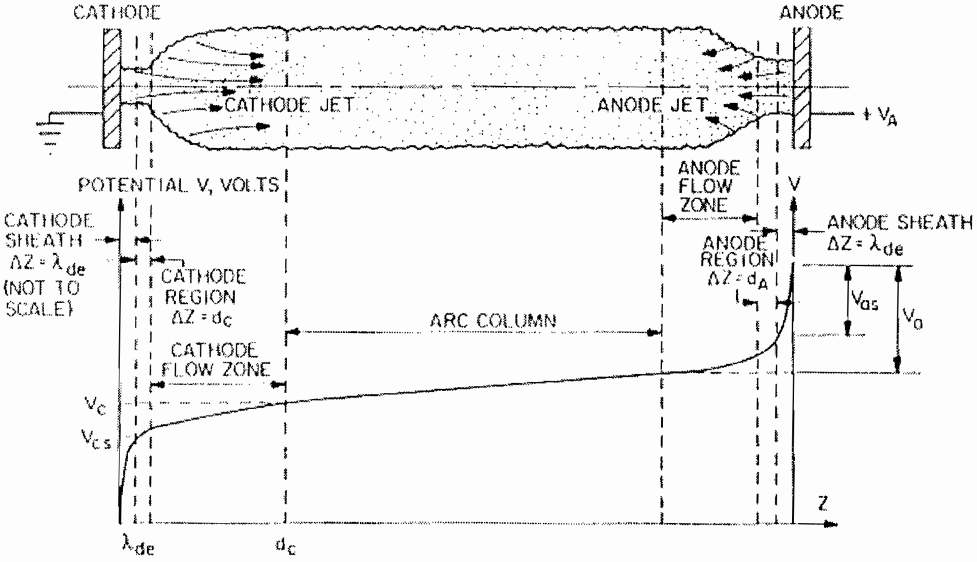

Figure 2-2: A schematic diagram of the regions of an arc (Roth 1995).

presheath zone). The cathode sheath zone can be thought as a collisionless zone, and the density of the positive ions is much greater than that of the emitted electrons because of faster movement of electrons. The positive space charge zone is, therefore, established and produces an electric field. The electric field strengths as well as the positive ion bombardment in the cathode region are recognized to be responsible for electron emission from arc cathodes.

In the cathode region, there are cathode jets which may exert a strong influence on the cathode region and sometimes on the entire arc. The cathode jets have been observed in hot as well as cold cathodes, particularly at higher current levels. Choi (1981) stated that these cathode jets might be attributed to four different sources: electromagnetically induced jets, vaporization of cathode material and/or surface impurities, ablation and explosive release of cathode material, and chemical reactions on the cathode surface producing gases. The interaction of the arc current with its own magnetic field leads to the phenomena of induced plasma jets in an arc section of variable cross section. These phenomena are not restricted to the cathode or anode region of an arc; they may also occur in other parts of the arc column where the conditions of variable column cross section are met. The induced cathode jet may serve as a stabilizing mechanism for a free-burning arc.

2.2.3. RANGES OF PHYSICAL PROPERTIES OF THE SPOTS

Even though numerous researches on thermionic and cathode spots have been reported, it is still difficult to find general agreement. This part, therefore, focuses on the ranges of physical properties of the spots; these are size, current density, and lifetime of the spots. The properties are dynamic and based on experimental results through arc tracks.

1) Size of the spots

Generally the size of the thermionic spot is bigger. According to Anders et al.'s (1991) survey on arcs in a pressure range from ultrahigh vacuum (UHV) to 10^7 Pa and in a current range from 0.1 to 10^5 A, for high pressure arcs in the thermionic regime, the thermionic spot area is between 0.1 and 10 mm^2. By assuming the thermionic spot is a circle, the diameter of the thermionic spot may be estimated to be between 0.4 and 3.6 mm. For low pressure arcs in the thermionic emission regime, they reported the range of the thermionic spot area of 0.01 ~ 1 cm^2 ; this range corresponds to a circle diameter of 1.1 ~ 11.3 mm.

For high pressure arcs in the thermofield emission regime, Coulombe (1997) reported the craters of 5 ~10 μm-diameter and some of up to 25 μm-diameter uniformly distributed along the arc trace on the copper electrode. For vacuum arcs believed in the thermofield emission regime, Kandah (1997) reported the general range of the cathode spot diameter of 0.01 ~ 100 μm. Siemroth et al. (1995) provided more detailed information about the size in vacuum arcs. They reported that in a pressure range from 10^{-4} ~ 10^{-3} Pa, the size of a macrospot on the copper electrode is 100 μm and that of the cathode spots inside the macrospot is 10μm.

2) Current density of the spots

In the thermionic emission regime, Anders et al. (1991) gave the range of current density of $10^4 \sim 10^8$ A/m^2 for both low and high pressure arcs. For high pressure arcs the current density is between $10^7 \sim 10^8$ A/m^2 which is the same range as Guile (1971). For low pressure arcs the current density is between $10^4 \sim 10^7$ A/m^2.

For high pressure arcs in the thermofield emission regime, Guile (1971) reported the range of current density of $10^{10} \sim 10^{11}$ A/m^2 as introduced in Table 2-1. For vacuum arcs, Kandah (1997) gave the general range of current density of $10^6 \sim 10^{12}$ A/m^2.

Generally the current density in the thermofield emission regime is higher than that in the thermionic emission regime. In the thermionic emission regime, the current density can be estimated through total current divided by the thermionic spot area. For the thermofield emission regime, however, several cathode spots are in the arc attachment area, resulting in the splitting of the arc. Therefore, the current density in the thermofield emission regime is based on the individual spot area and the current delivered to each spot.

3) Lifetime scale of the spots

It is especially difficult to determine general lifetime scale of the spots, but the lifetime scale may be inferred through the arc movement. As mentioned earlier for the thermionic emission regime the arc movement is slow or fixed; however, for the thermofield emission regime the arc movement is rapid. These different types of arc movement are related to the lifetime scale of the spots because the spots are the sites of electron emission.

For the thermionic emission regime, Anders et al. (1991) reported that for high pressure arcs, hopping of the thermionic spot may occur and the hopping frequency is about several Hertz. It can be inferred from the frequency that the lifetime scale of the thermionic spot may be a time of the order of decisecond. This time scale may be rough, but it can be seen that this scale is much bigger than the lifetime scale of the cathode spots in the thermofield emission regime, which is introduced in the next paragraph.

For the thermofield emission regime, the faster movement of arcs is associated with the cathode spots' extinction and reignition at new sites. This is one of the reasons for the voltage fluctuations of cold cathodes. Because arcs move irregularly, this is also referred to as "random walk". For the spots in the thermofield emission regime, two different lifetime scales are reported. One is the lifetime scale of the macrospots and the other is that of the cathode spots inside the macrospot spot. The lifetime scale of the macrospot in this regime, according to Coulombe's (1997) review, is much less than 1 ms scale and probably of the order of 1 μs. Meanwhile, Jütter (1997, 1999) reported the lifetime scale of the cathode spots is of the order of nanoseconds.

2.2.4. EROSION OF ARC CATHODES

Arc cathode erosion can be simply defined as vaporization of the cathode material and ejection of particles and molten cathode material mainly due to the localized excess heat which cannot be dissipated either by conduction through the cathode or radiation and convection from the cathode surface. In general, arc cathode erosion is considered as a necessary physical phenomenon to maintain an arc for the thermofield emission and as a consequence of the strong heat load for the thermionic emission.

In the following part previous work related to the heat transfer at the cathode spot surface, performed at Plasma Technology Research Center (CRTP), McGill University is introduced. The heat transfer as well as the current transport is very important for erosion studies because it is related to the localized heat flux. In addition, Benilov's review (1999) about the heating of hot cathodes of high pressure arcs is also mentioned.

Szente et al. (1992), who studied the erosion of copper cathodes, noted that the arc heats the cathode in four different ways: radiation, convection (from the plasma), joule heating, and ion bombardment. Among them, the joule heating and the ion bombardment have been recognized as the main source of the heat input to the cathode. The positive ions directly transport their energy to the cathode spot as shown in Figure 2-3. The transported energy is lost by vaporization of the cathode material, electron emission cooling, and conduction within the cathode. Joule heating may be appreciable with a low conductivity cathode and in the very high current density regions near the emitting areas. The radiation and convection terms are too diffuse to cause erosion and can in general be neglected for most erosion studies.

Coulombe et al. (1997) calculated the magnitude of the different source of the heat flux at the cathode spot surface on a cold copper cathode. In their calculation, for the current transport in the cathode sheath, they described that three charge carriers are related to the current transport to the cathode spot, respectively j_{ion} for the ions, j_{bde} for the back-diffusing electrons, and $j_{T\text{-}F}$ for the electrons emitted by the thermofield emission from the cathode as shown in Figure 2-3. For the energy balance on the cathode spot surface, they described that energy is transported to the cathode spot by the positive ions (q_{ion}) and back-diffusing electrons (q_{bde}); energy is lost by vaporization of the cathode material (q_{vap}), by electron emission cooling (q_{not}), and by conduction within the cathode (q_{cond}). Radiative heat exchanges from the cathode spot surface with the surroundings are ignored in comparison with the other heat fluxes. The results are presented in Table 2-2. It can be seen that the heat input to the cathode spot surface (q_{in}) is increased as the total current density (j_{tot}) is increased, and the ion bombardment is the dominant component of the heat input. For the heat loss, as the total current is increased, the electron emission cooling (q_{not}) is more important than the other heat fluxes of the heat loss. The vaporization of the cathode material (q_{vap}) is also increased, and this means increase of the erosion rate. Meanwhile, the importance of the conduction within the cathode (q_{cond}) is decreased as the total current increased.

For the heating of hot cathodes of high pressure arcs, Benilov (1999) stated that presently there is no general agreement on the dominating mechanism of the heat transfer to the thermionic spot. According to his review, for the main component of the heat input, some researchers believe that the hot cathode is mainly heated by the ion bombardment, while others consider that the thermal conduction from the arc is greater than the contribution of the ion bombardment. In any case it appears that further research about that is needed.

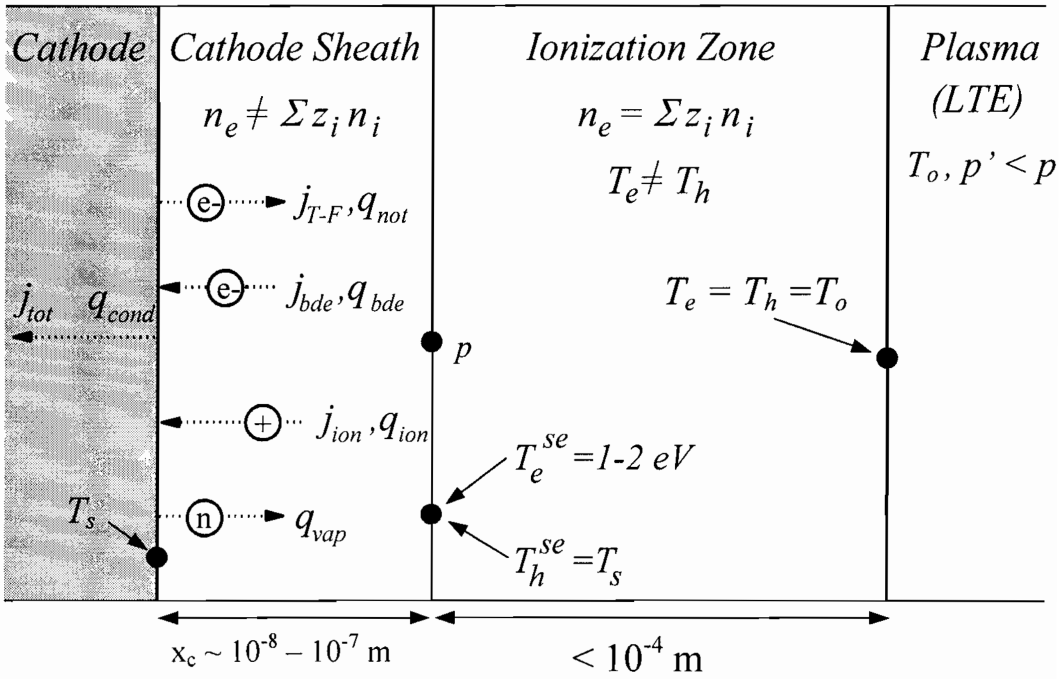

Figure 2-3: The cathode region prepared by Coulombe et al. for their modeling work (Coulombe et al. 1997).

Table 2-2: Distribution of the total heat flux to a single cathode spot on a cold Cu cathode for T_e at the cathode sheath edge = 1 eV (Coulombe et al. 1997).

V_c (V)	J_{tot} ($x10^9$ Am^{-2})	q_{in} ($x10^{10}$ Wm^{-2})	q_{ion}/q_{in}	q_{not}/q_{in}	q_{vap}/q_{in}	q_{cond}/q_{in}
7	1	1.18	0.95	0.07	0.27	0.66
7	5	3.48	0.95	0.31	0.30	0.39
7	10	5.28	0.95	0.46	0.31	0.23
15	1	1.54	~ 1	0.06	0.17	0.77
15	5	4.28	~ 1	0.26	0.18	0.56
15	10	5.93	~ 1	0.45	0.20	0.35

The erosion mechanism of arc cathodes is not yet understood perfectly because many physical phenomena occur in the very thin cathode region at the same time. The erosion phenomenon, however, may be explained by the following well-known three considerations: 1) evaporation of cathode material, 2) ejection of particles and droplets of molten cathode material, and 3) redeposition. Evaporation can be explained as being caused by the localized excess heat fluxes over the spot surface. Coulombe (1997) stated that ejection is mainly due to the ion pressure release upon the spot extinction and the onset of important thermo-capillary flows within the molten bath. Redeposition reduces the erosion rate of cathodes and may come from 1) by the condensation of vaporized cathode atoms existing in the vicinity of the arc root and 2) by the neutralization of the positive ions of cathode materials on the cathode spot surface. In case of the condensation, Zhou et al. (1994) mentioned tungsten redeposition in the form of whiskers and Meunier et al. (1987) reported copper redeposition. For copper redeposition, it was believed that the copper redeposited was part of the bulk of the cathode structure and could carry the current because no weakly bounded structure was found through their microscopic observation. Also, for fullerence synthesis the carbon redeposition, i.e. the deposition of vaporized graphite material from the anode on the graphite cathode surface, has been reported. Lefort et al. (1993) used the redeposition by the neutralization of the positive ions of cathode materials in their modeling work.

2.3. GRAPHITE ELECTRODES

Graphite electrodes are widely used in thermal plasma processing. Typically graphite electrodes have been reliably used in EAFs. Recently in case of recycling or treatment of solid wastes, graphite electrodes have been considered possibly superior to metal torches. Finally graphite arc discharges in a helium atmosphere are the one of the present methods for fullerene production.

2.3.1. General Characteristics of Graphite

Graphite is one of the four allotropes of carbon; the others are amorphous carbon, diamond, and fullerenes. Graphite is based on sp^2 structure and its structure is described as layers of carbon atoms with an interatomic distance of 0.142 nm and with an interplanar distance of 0.335 nm as shown in Figure 2-4 (Encyclopedia of Chemical Technology 1992). Each carbon atom within the layers is bonded only to three carbon atoms in a trigonal planar arrangement with 120° angles (Kandah 1997). Because each atom is formally bonded to only three neighboring atoms, the remaining valence electron (one in each atom) is free to circulate within each plane of atoms; therefore, graphite is an

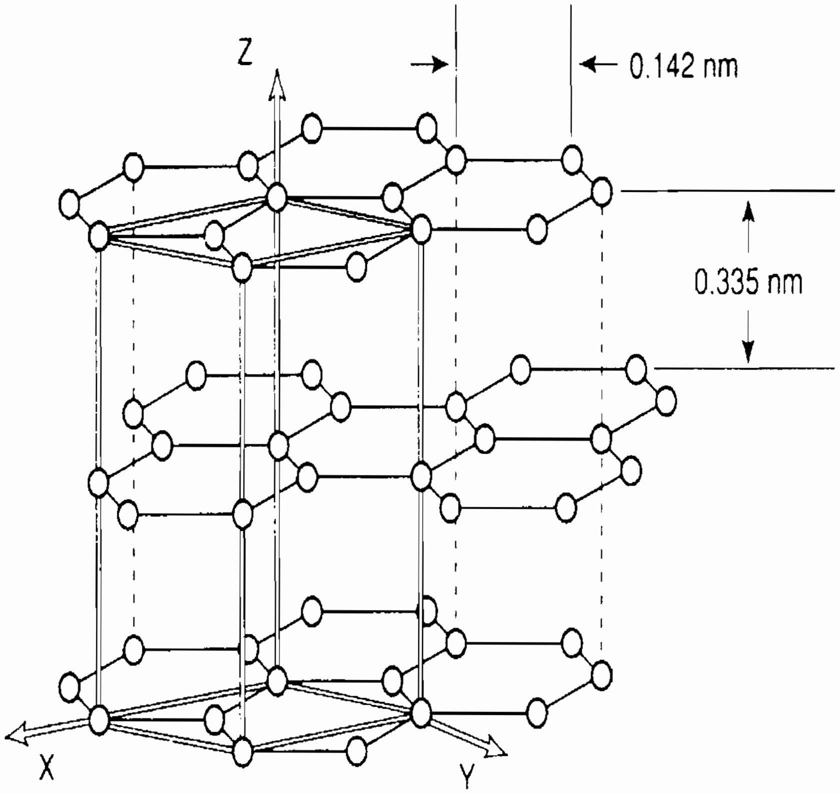

Figure 2-4: Structure of graphite (Encyclopedia of Chemical Technology 1992).

electrical conductor. In addition, separation of each layer represents a non-bonding situation, and thus graphite can be used as a lubricant.

In this work polycrystalline graphite, which is a blend of amorphous carbon and very small graphite crystals, has been used for electrodes and its general production process, provided by POCO Graphite INC., USA, is as follows. Polycrystaline graphite is made by the calcination of the raw material, i.e. petroleum coke, in large kilns to shrink it and drive out the volatile content. It is then crushed into a very fine powder and sized into different particle sizes through screens. The crushed raw material is mixed with a binder, compressed into a block, and fired at very high temperature to remove any volatile materials and to assure homogeneity. Because the coke does not melt during processing, the resultant structure is much like sand that is stuck together by a thin layer of glue. Generally polycrystalline graphite has some anisotropy; however, POCO graphite, used in this work, is isotropic.

2.3.2. Graphite Electrodes in Arc Furnaces

In this part several features of graphite electrodes in arc furnaces are introduced because graphite electrodes are typically used in EAFs. In many arc furnaces it seems that water-cooled metal electrodes may not be needed. A simple graphite electrode will be sufficient although the improvement of the arc stability is required. Barcza (1986) has reported that the arc stability can be realized if the graphite electrode is made in the form of a hollow electrode to introduce plasma gas through a small hole and the end of the graphite electrode is shaped to improve the directionality of an arc to an open bath in arc furnaces.

Compared with water-cooled metal electrodes, graphite electrodes have some advantages. Graphite electrodes are generally more massive than water-cooled metallic electrodes so that they can carry higher electrical currents. Moreover, because they are refractory, heavy water-cooling is not necessary. Sometimes water leaks of water-cooled metallic electrodes result in explosions in arc furnaces.

As is well known, graphite electrodes are consumed during the operation of arc furnaces. Through field tests, it has been reported that the consumption of the graphite electrodes in EAFs can be divided into three broad categories: tip consumption, sidewall consumption, and breakage (Lefrank et al. 1983, Schwabe 1971, Encyclopedia of Chemical Technology 1980). Figure 2-5 shows the longitudinal loss resulting from the tip consumption and the transverse loss because of the sidewall consumption in case of graphite electrodes of AC EAFs. Roughly half of the observed consumption occurs at the graphite electrode tip where the intensely hot and rapidly moving arc root produces both vaporization of the graphite and some ejection of small graphite particles. In addition, the graphite electrode tip can be eroded by contact with the liquid metal and slag. The rate of incremental tip consumption generally increases when operating current or power is increased. The sidewall of hot graphite electrodes is consumed by reaction with oxidizing atmospheres both inside and outside the EAFs, resulting in a tapering of the graphite electrode toward the arc tip. The sidewall consumption is increased by the use of many fume removal systems and by the use of oxygen in the EAFs for assisting melting or refining. Kaltenhauser et al. (1983) mentioned that since the sidewall consumption may account for 40 % or more of the total graphite electrode consumption, extensive efforts have been

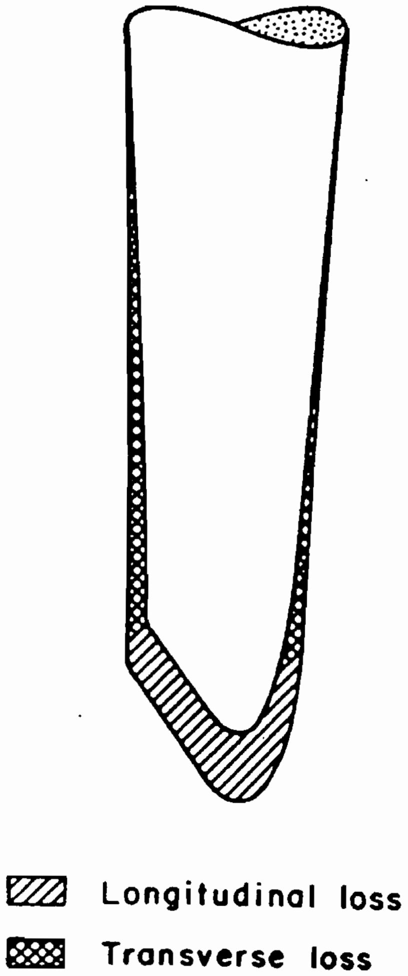

Figure 2-5: Typical consumption patterns of a graphite electrode in AC EAFs (Jurewicz 1997).

made to reduce this component of consumption through the use of oxidation retardants and electrode coating. Such efforts have had little success to date, primarily because of the extreme thermal and chemical environment to which the graphite electrode is exposed. A third form of consumption consists primarily of graphite electrode breakage resulting from excessive movement of large masses of scarp during melting or the presence of nonconductors in the charge. Although such breakage usually accounts for less than 10 % of the total graphite electrode consumption, excessive thermal shock, improper joining practice, and incorrect phase rotation may magnify this form of electrode consumption.

Owing to the development of solid state diodes and high current thyristor controlled rectifiers in the recent past, interest in DC EAFs has strongly been stimulated. As the main advantages of DC EAFs over AC EAFs, Jurewicz (1997) mentioned 1) lower graphite electrode consumption, 2) higher electrode current carrying capability, 3) reduced disturbances in electrical supply systems (less flicker), 4) uniform heat distribution, 5) the stirring effect, and 6) lower noise emission. Besides less wear on flexible power cables (less electrode movement), reduced maintenance on electrode arm of furnaces, less electrode breakage, and lower energy consumption have been mentioned. On the other hand the requirement of the bottom (bath) electrode and relatively difficult arc starting have been recognized as the disadvantages of DC EAFs. The bottom electrode may not be easily cooled and increases maintenance problems. Also, in case of insufficient electrical contact between the cathode and the bottom electrode, it may be difficult to ignite an arc. In that case a metal or a graphite rod may be used as an auxiliary electrode in the bath to establish the electrical contact between the cathode and the anode.

2.4. THE ARC STABILITY OF HOLLOW GRAPHITE ELECTRODES

Maddever et al. (1976) studied the effect of the gas injection on the arc stabilization and the consumption rate of hollow graphite AC electrodes on the laboratory and the industrial scale. For the laboratory scale the diameter of the graphite electrode was 7/8 inches and that of the hole in the graphite electrode for the gas injection was 1/8 inches. Various gases such as argon, nitrogen, carbon dioxide, and several hydrocarbons were investigated. The gas flow rates were approximately 2 ~ 3 ft^3 per hour. Among the gases, the argon gas was preferred because it provided the uniform and sinusoidal waveforms of the current, the voltage, and the power without the operating problems. Nitrogen gas enhanced pickup of that gas into the melt by a considerable degree, and hydrocarbon gases caused the blocking of the hole by the carbon deposition. The uniform and sinusoidal waveforms meant the increase of the arc stability. Experiments performed with the argon gas injection also showed the decrease of the consumption rate of the electrodes. For the plant scale the diameter of the graphite electrodes was 7 inches and that of the hole was 1/4 inches. In case of the argon gas flow rate of 40 ft^3 per hour, enhancement of the arc stability was reported as in the results of the laboratory experiments.

Sommerville et al. (1987) further studied the work of Maddever et al. (1976) and reported several general characteristics of the improvement of the arc stability of the hollow graphite AC electrodes. The characteristics are as following: 1) the waveforms of the current and the voltage are considerably smoother for stable arcs, 2) the arc can be extended easily and is less apt to be self-extinguished, 3) the arc shows the strong directional component, and follows a more confined path with less tendency to flare, 4) the acoustical and the electrical noise is decreased, and 5) the consumption rate of the graphite electrodes decreased; in their study the consumption rate was decreased from 9.99 to 8.62 lb/ton of product.

Ochs et al. (1989) studied the improvement of the arc stability of hollow graphite AC electrodes in an EAF. The power was supplied to the electrodes through two single-phase AC welders connected in parallel and rated at 1500 A, thus providing the maximum operating current of 3000 A. The structure of their hollow graphite electrodes was quite different from that of the electrodes used by Maddever et al. (1976) and Sommerville et al. (1987). Ochs et al. (1989) made multiple holes in the graphite electrode for the gas injection. The 12 holes of 1/32 inches diameter were located on the 1 inch diameter circle encompassing the electrode tip (see Figure 2-6). This tip was connected to 3 inch graphite electrodes. The inert gases of helium and argon were injected into these holes as well as windows of the EAF. The inert gases shrouded the arc, thus maintaining the arc in a vertical direction and allowing more of the heat to be directed to the melt. The gases also helped to confine the arc to the tip section while it cooled the outer portion of the electrode and decreased the consumption rate by reducing the oxidation of the graphite electrode.

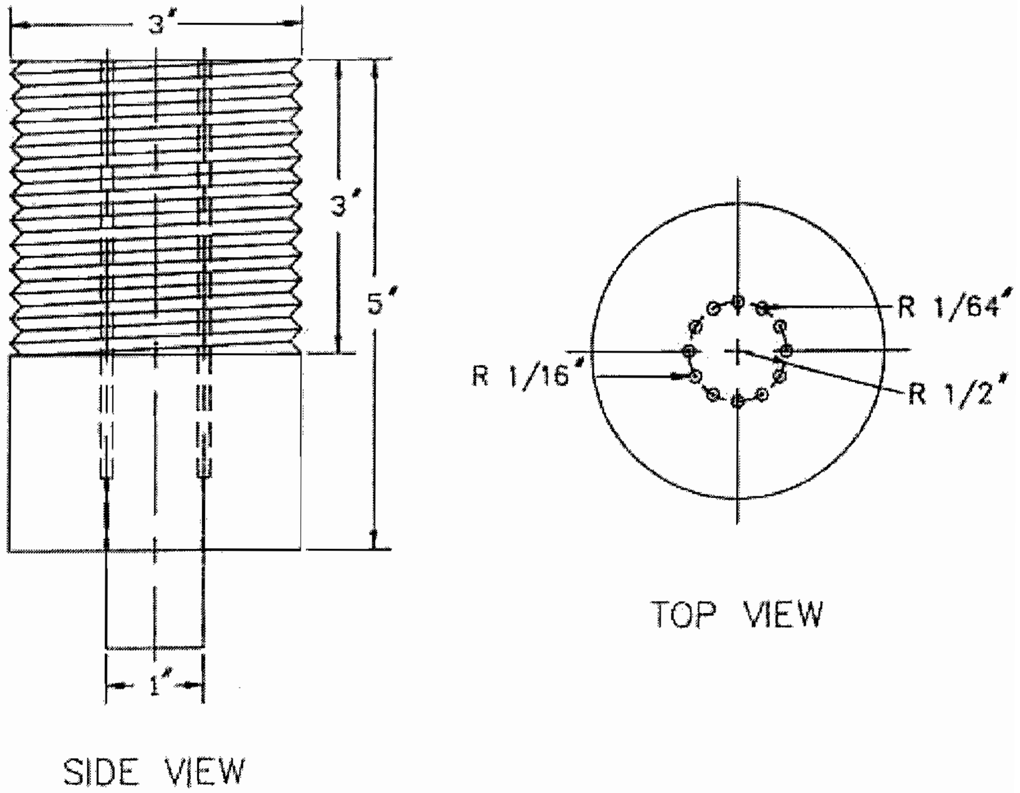

SIDE VIEW

TOP VIEW

Figure 2-6: Schematic drawings of the electrode tip with the holes (Ochs et al. 1989).

2.5. EROSION OF GRAPHITE ELECTRODES

Holm (1949) proposed an energy balance at the cathode spot to provide an explanation of the vaporization of metal and carbon cathodes, i.e. the cathode erosion. He assumed that the total energy produced in the cathode region was transferred to the cathode and neglected the relatively small radiation from the cathode. Although Holm's study is simple and has several oversimplifications, it has produced significant results, which are well-accepted today. The results are that the high vaporization from the cathode is inevitable and as the current density increases, the heat loss by vaporization is much more important than the heat loss by conduction. Later, Holm (1967) modified this energy balance by replacing the total current term with the ion current term since the main component of the input energy to the cathode spot is the positive ion bombardment.

Mentel (1977, 1977, 1978) studied the influence of vaporization upon the arc roots of high current arcs using graphite rod DC cathodes. His study provides a range of erosion rate of a graphite cathode measured in an argon atmosphere at atmospheric pressure and the temperature of graphite vapor jets. The diameters of the graphite DC cathodes were 3, 4.6, and 6.15 mm. High-speed photography of the arc roots at 1000 A in argon atmosphere showed that the cooling of the electrodes could affect the appearance of the arc roots. By changing the height of the cathode above the water-cooled collar, the cooling rate of the electrodes was controlled. The height variation was from 2 mm to 10 mm. For the strong cooling of the cathode (2 mm above the collar) the arc roots remained stable. In contrast, for the weaker cooling of the cathode (6 and 10 mm above the collar), the separation of the arc and the graphite vapor jet could be seen at the arc roots. The vapor was observed as a trail or jet and was relatively cold. The spectroscopic measurements of the C_2 molecular bands gave the vapor jet temperature was between 4000 and 5000 K. For the strong cooling, the erosion rate of the graphite cathode was increased slowly as the current density was increased; however, the erosion rate for the weaker cooling was increased greatly as shown in Figure 2-7. In addition, for the weaker cooling, it was reported that a large cathode spot developed as the current increased. It seems that the cathode spot he mentioned is a thermionic spot because his operating conditions are believed in the thermionic emission regime. The erosion rate for the height of 10 mm in Figure 2-7 was further analyzed because generally graphite electrodes are used without water-cooling. The unit of the erosion rate in Figure 2-7 is mg/(cm^2 s). This unit is converted into the μg/C unit used in this work and the results are presented in Table 2-3. The μg/C unit is the common unit in erosion studies and is independent of the arc duration. The estimated current range of his experiments in Figure 2-7 was between about 300 and 1040 A. The estimation of the erosion rate ranges from about 3.0 μg/C at 300 A to 85.7 μg/C at 1040 A. His equipment was designed to prevent the carbon redeposition from the graphite anode; therefore, these erosion rates may be thought as the erosion rate of the graphite cathode.

Lefort et al. (1993) proposed a model for graphite electrode erosion. They studied the cathode surface and its interaction with the space charge region to derive governing equations at the cathode. At the anode the equations were similar to those at the cathode. To estimate the erosion rate for the graphite cathode they assumed the cathode spot was one dimensional and was single, circular, and practically motionless. In addition, the

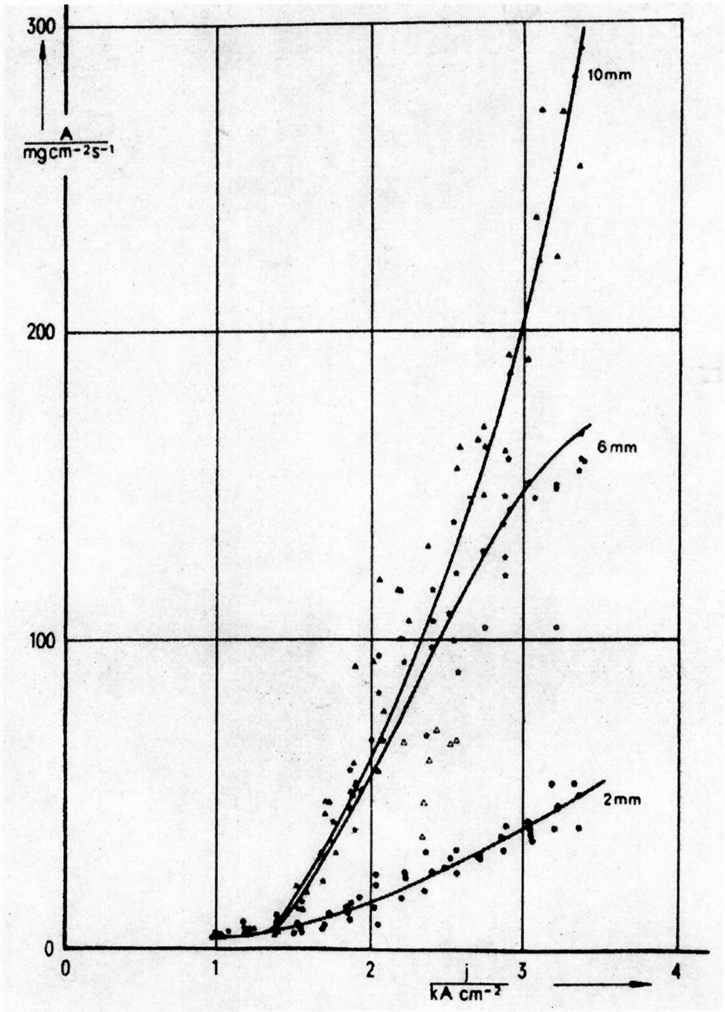

Figure 2-7: Erosion of the graphite cathodes with a diameter of 6.15 mm for different heights, h, of the electrode above the cooled collar (Mentel 1977).

Table 2-3: Conversion of the erosion rates of Mentel's work (1977).

Current density in Figure 2-7 (kA/cm^2)	Estimated current (A)$^{1)}$	Erosion rate for h = 10 mm in Figure 2-7 (mg/cm^{2}s)	Estimated erosion rate (mg/s)$^{2)}$	Estimated erosion rate (μg/C)$^{3)}$
1	297	3	0.9	3.0
2	594	63	18.8	31.7
3	891	200	59.4	66.7
3.5	1040	300	89.1	85.7

1) Conversion: the current density in Figure 2-7 (kA/cm^2) x the cross-sectional area of the graphite cathode (cm^2)

2) Conversion: the erosion rate in Figure 2-7 (mg/cm^2 s) x the cross-sectional area of the graphite cathode (cm^2)

3) Conversion: the erosion rate (mg/s) x 1000 / the estimated current (A)

cathode material was homogeneous with a perfect surface state and only cathode material evaporation was considered for erosion. The unique feature of their theoretical work is the introduction of the redeposition by the neutralization of the positive ion current. When calculating the erosion rate with considering the redeposition, they assumed all the positive ionic flux coming from the ionization region was captured and neutralized on the cathode surface. In addition, they introduced a general empirical model of the erosion rates of the graphite electrodes in AC arc furnaces as follows:

$$G = K\, I^{\alpha} \tag{2-2}$$

where G is the mass loss in kg/second; K is a constant; I is the arc current in A; α is a constant between 1 and 2. The Research Institute of French Iron and Steel Metallurgy (IRSID) modified this model for the mass losses (G) of graphite electrodes in DC arc furnaces as follows:

$$G = 6.6 \times 10^{-9} I_m^2 \qquad (2\text{-}3)$$

where I_m is the mean current calculated over a half period in A; G is in 10^{-3} kg/second. Lefort et al. (1993) compared their erosion rate estimation including the anode erosion with the IRSID model and found out their estimation was greater. They concluded that one of the reasons of the over-estimation was the lack of the information about the mechanism of the redeposition.

2.6. Applications of Hollow Graphite DC Cathode

In this part, industrial applications of hollow graphite DC cathodes have been reviewed. The tundish heating at the BGH, The Electro-Pyrolysis Inc. (EPI) Arc Furnace, the Exide High Temperature Metals Recovery (EHTMR) process of the Exide Co., the Arc Technology Company process, and the DROSCAR process of the Hydro-Quebec are introduced.

Some processes using the graphite cathodes for treatment of solid wastes are introduced because of the recent interest of the transferred arc treatment of solid wastes. In the arc treatment, graphite electrodes have been proposed for the electrodes of the transferred arc plasma and may be expected to replace water-cooled metallic electrodes because of the advantages mentioned in the earlier part. (Wittle et al. 1994, Drouet et al. 1995, Schumacher et al. 1995, Rozelle et al. 1995, Neuschutz 1996, Eddy 1999). The historical perspective and up-to-date trends of plasma technology for these applications are well reviewed by Cohn(1997), Fauchais et al. (1997), and Counts et al. (1999).

2.6.1 The Tundish Heating at the BGH

Neuschütz et al. (1996) investigated the arc heating in the tundish with a hollow graphite DC cathode in comparison with a metallic plasma torch. This study was performed at the BGH Edelstahl Siegen GmbH, a steelmaker located at Siegen, Germany. The length of the DC graphite cathode they used was 1250 mm and the diameter was 100 mm. Argon was blown at a rate of 3.6 m^3 per hour through a 20 mm hole into the arc for stabilization. The average arc voltage was 100 V and the maximum arc current was 3300 A. The electrode position was continuously adapted to keep the arc voltage constant. They reported the consumption rate of the graphite electrode by both the tip and side wear was 0.46 kg/hour after 6 months of the operation. The average current of the operation was 2000 A. Also, they reported another tip and side consumption rates of a different hollow graphite electrode of the BGH. The side wear was 0.04 kg/hour and the tip wear was 0.78 kg/hour. They analyzed that the lower side consumption rate was due to the argon gas injection, which caused the reduction of the oxygen partial pressure around the graphite electrode. Compared to metallic torches, they concluded that except for sensitive steel grades, the hollow graphite DC cathode appeared to be recommendable for all steel grades operations because the running costs were lower than with metallic torches because of less water cooling, less wear of parts like nozzles and starting electrodes, and less personnel for maintenance.

2.6.2. The EPI Arc Furnace

Wittle et al. (1994) reported that Electro-Pyrolysis Inc. (EPI), Massachusettes Institute of Technology (MIT), and Pacific Northwest Laboratory (PNL) developed DC graphite arc furnaces named EPI's Mark I and Mark II to the processing of Subsurface Disposal Area (SDA) wastes. According to their report the graphite electrode DC arc furnace is attractive because it provides the advantages of simplicity, high availability, safety, high processing rate, easy of scale-up, and versatility and thus the furnace is well suited for treating high melting point wastes containing metals. The Mark I furnace (see Figure 2-8) includes a graphite crucible with a capacity of one hundred pounds of material. A movable two-inch diameter graphite electrode is located in the center of the graphite crucible. The entire system is contained in a square carbon steel box with hot face brick and insulating brick surrounding the crucible. The Mark I furnace is capable of operating at DC power levels of 300 kW. The furnace has operated under an inert atmosphere by purging $3 \sim 4$ ft^3 per minute of N_2 through the furnace chamber. The Mark II furnace is approximately 23 feet in height and 7 feet in diameter. The furnace is a refractory lined carbon steel vessel as shown in Figure 2-9. The graphite electrode in the Mark II furnace incorporates a unique coaxial arrangement within an outer graphite electrode that is 16 inches in outside diameter and 10 inches inside diameter. The inner graphite electrode is a solid 6 inches piece of graphite. This electrode assembly has the capability to operate in the transferred arc mode or the non-transferred mode. This allowed the furnace to be easily started by operating the torch in the non-transferred mode to melt the material in the crucible. When the molten material becomes electrically conductive, the operation of the electrode can then be changed to the transferred mode of operation. The transferred mode which is a more efficient method of providing heat-energy to the material being melted.

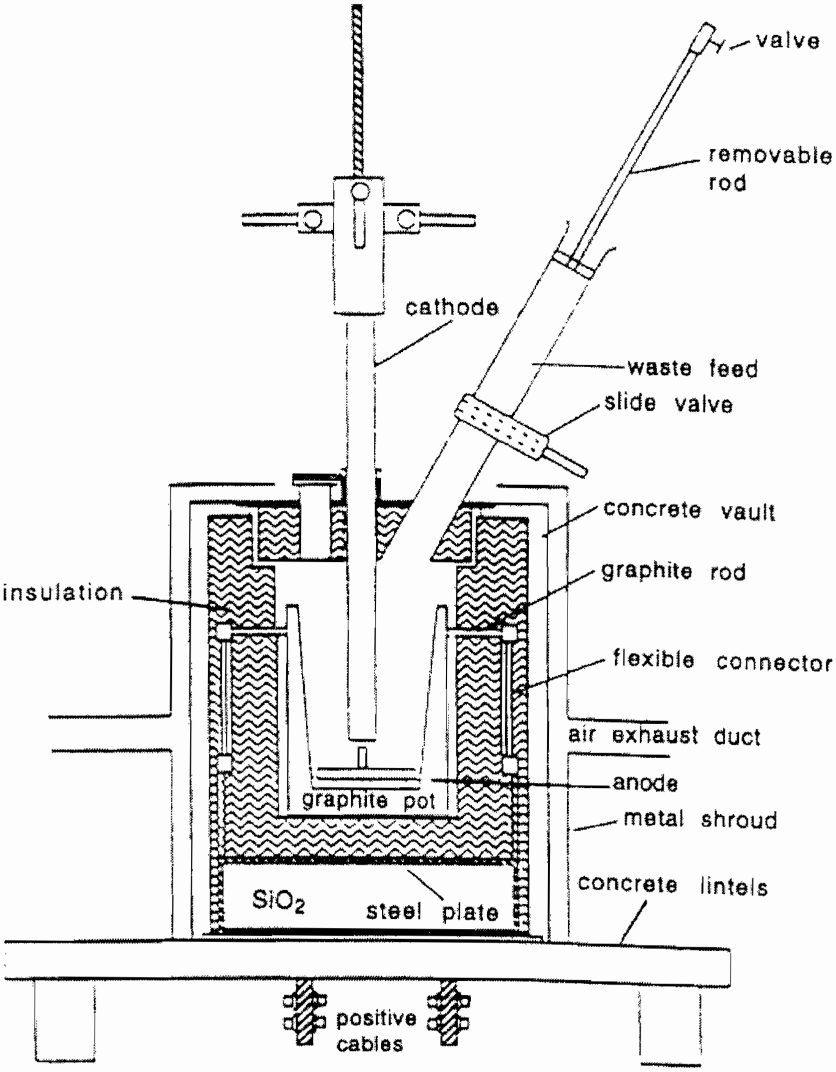

Figure 2-8: The schematic diagram of the EPI's Mark I furnace (Wittle et al. 1994).

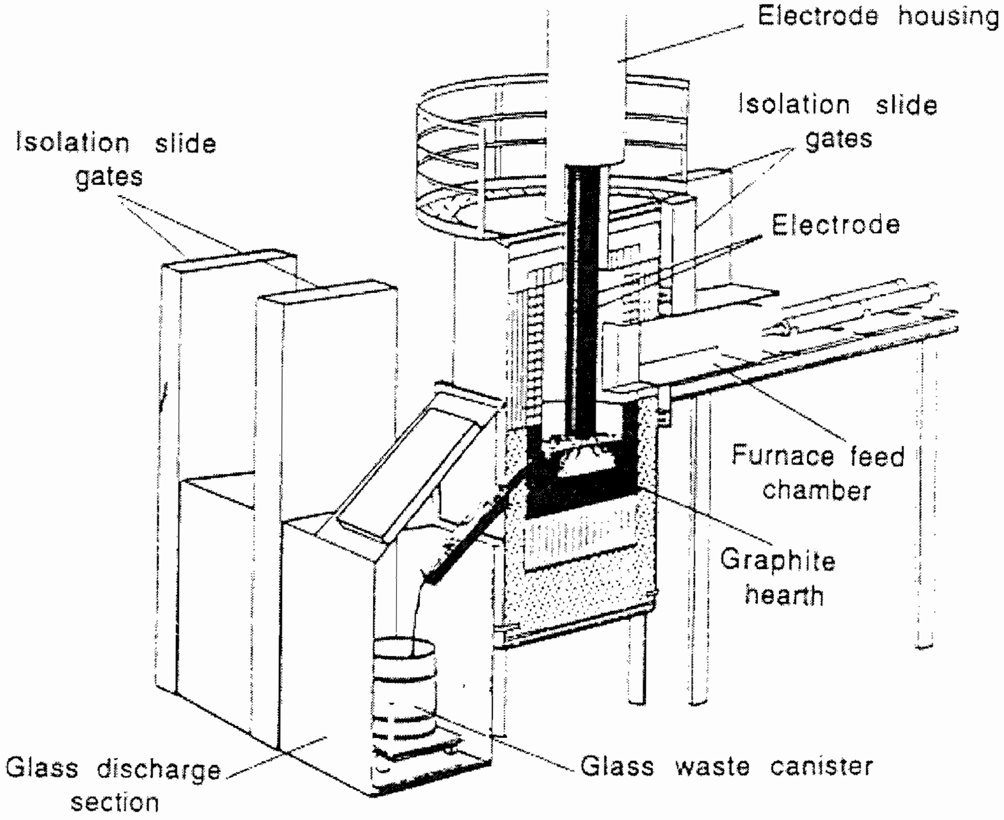

Figure 2-9: The schematic diagram of the EPI's MarkII furnace (Wittle et al. 1994).

2.6.3. The EHTMR Process

The Exide Corportion (Rozelle et al. 1995) developed the Exide High Temperature Metals Recovery (EHTMR) process to treat a variety of solid wastes and by-products containing metals by using a submerged transferred arc plasma. The process is designed to recover the valuable metals in the solid wastes for reuse and to produce a metals-depleted slag that can be marketable. The heart of the EHTMR process is a DC transferred arc plasma furnace (see Figure 2-10). This furnace features a hollow graphite DC cathode through which the solid wastes can be fed. In order to assist in solid waste feeding and to provide arc stabilization, the process is equipped with a system to feed inert plasma gas (argon) through the electrode. Solid wastes requiring fuming through the electrode were fed through the zone of maximum energy density at the arc which enhances volatilization of metals in the solid wastes. This is an inherent advantage in transferred plasma arc operations with a hollow electrode feed, which is not possible in non-transferred plasma arc operations.

2.6.4. The Arc Technology Company Process

The Arc Technology Company (UIE, 1988) developed a DC arc furnace (see Figure 2-11) for the destruction of PCB filled condensers. The furnace is a chamber, with walls made of refractory graphite, where an electric arc is initiated between a hollow graphite DC electrode and a bath of molten metals. The entire condenser is brought into the bath of metals at 1650 ^{o}C located at the bottom of the furnace (area 1). The condenser melts and releases its PCBs which are subjected to ultraviolet radiation from the plasma arc and

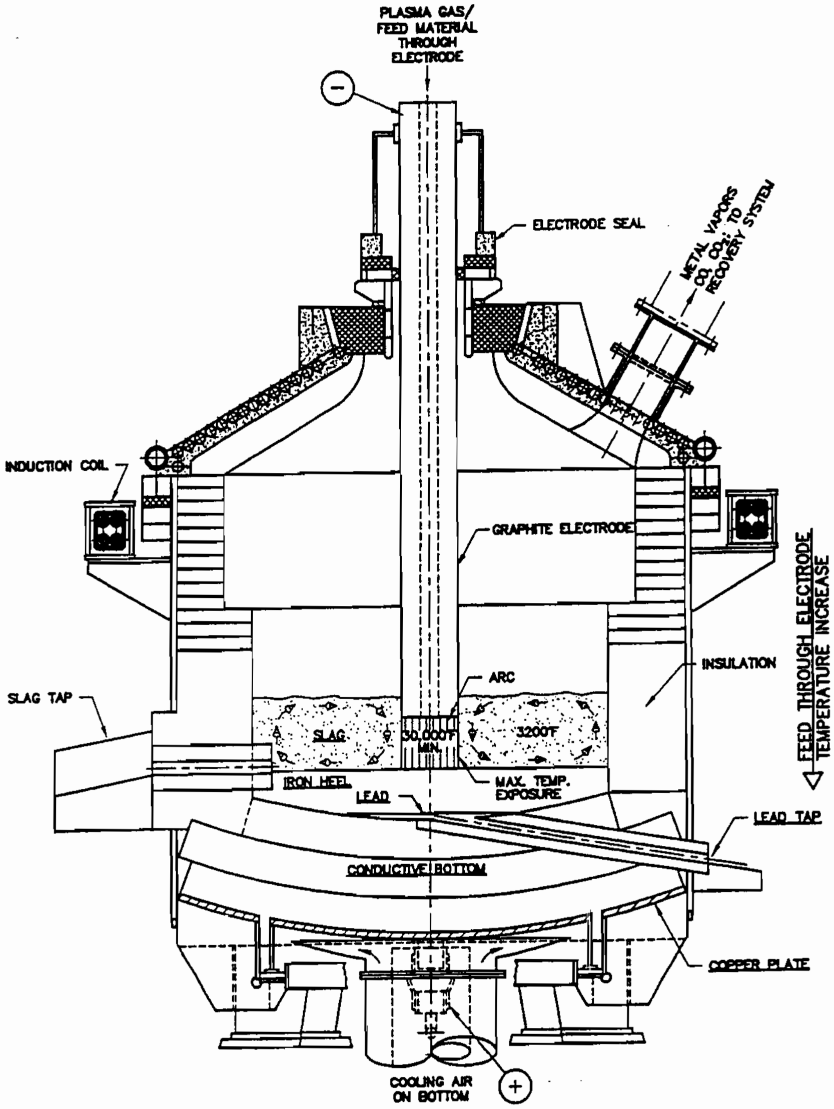

Figure 2-10: The transferred arc furnace of the EHTMR process (Rozelle et al. 1995).

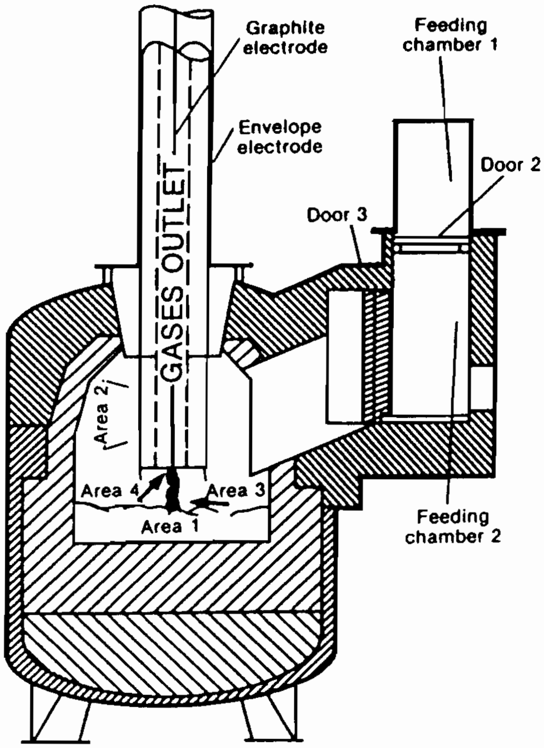

Area 1 : molten metals 1650°C
Area 2 : furnace 1650°C t_s = 1.77 s
Area 3 : gas envelope # 6100°C
Area 4 : electric arc 6100°C t_s = 3 ms
N_2 gas, noise 50 dB — Height 8 m

Figure 2-11: The transferred arc furnace of the Arc Technology Company process (UIM 1988).

to the heat from the molten metal. As a result, the PCBs are pyrolysed. The pyrolysis gases are extracted by the inside of the electrode after going through the electric arc (area 4) and its gaseous envelope (area 3). This installation has a treatment capacity of 1500 kg/hour; it produces 750 kg/hour of molten metals and 882 Nm^3/hour gases containing CO, H_2, and HCl. The gases are purified in two successive washing venturi scrubbers. The destruction efficiency of the system is 99.9999%.

2.6.5. The DROSCAR Process

Hydro-Quebec has developed a rotary DC graphite arc furnace for aluminum dross treatment. Aluminum dross occurs as an unavoidable by-product of all aluminum melting operations. Generally, depending on the operations, it represents 1 to 5 weight % of the melt and may contain as much as 75 weight % of free aluminum in the form of very small droplets entrapped in aluminum oxides. Since aluminum production is highly energy-intensive, aluminum dross recycling is very attractive. The conventional recycling process uses rotary salt furnaces heated with a fuel or a gas burner but the process is thermally inefficient and environmentally unacceptable because of salt slags. Plasma recycling treatment of the aluminum dross is thus being developed. Neuschutz (1996) and Burkhard et al. (1994) reviewed the existing aluminum dross recycling processes: the Alcan process, the Hydro-Quebec process, the BOC process, and the MGC process. Among them, only the Hydro-Quebec process named the DROSCAR process has been introduced here because the process uses graphite DC electrodes.

The DROSCAR process employs a new salt-free technology for the treatment of the aluminum dross which uses a rotary furnace heated by a DC electric arc between two graphite electrodes as shown in Figure 2-12 (Drouet et al. 1994, 1995). In Table 2-4 the optimal operating parameters of the 600 kW DROSCAR pilot plant are presented. An electric arc stretched and maintained between two graphite electrodes is used to heat the charge above the aluminum melting point. The energy transfer mechanism in the furnace is mainly radiation from the arc to the refractories and the charge. Heat transfer by conduction between the refractories and the charge also plays an important role. The furnace rotates as the dross is heated to provide mechanical stirring, which breaks the oxide film on the droplets of aluminum present in the dross and promotes agglomeration of the molten metal. Rotation also prevents formation of hot spots on the charge or refractories and improves energy transfer. On completion of the heating, the metal is tapped from the furnace through a hole in the side. The solid residues remaining in the furnace form a greyish powder which is removed by tilting the furnace forward while slowly rotating it. Gaseous and particulate emissions are significantly reduced in this technology; only 3 m^3 gas is used per tonne of the dross treated compared to 30 m^3 per tonne the dross for the air plasma torch of the Alcan process and as much as 300 m^3 per tonne of the dross for the gas or fuel burner. Argon is used, especially for arc stabilization, and helps to create an inert atmosphere inside the furnace, thereby minimizing reactions between the molten aluminum and the furnace atmosphere. The oxidation and nitrification of the aluminum can be an important source of heat but should be avoided. No salt is added to improve recovery, so the charge is not increased, additional heating energy is not required, and the amount of residues is kept as low as

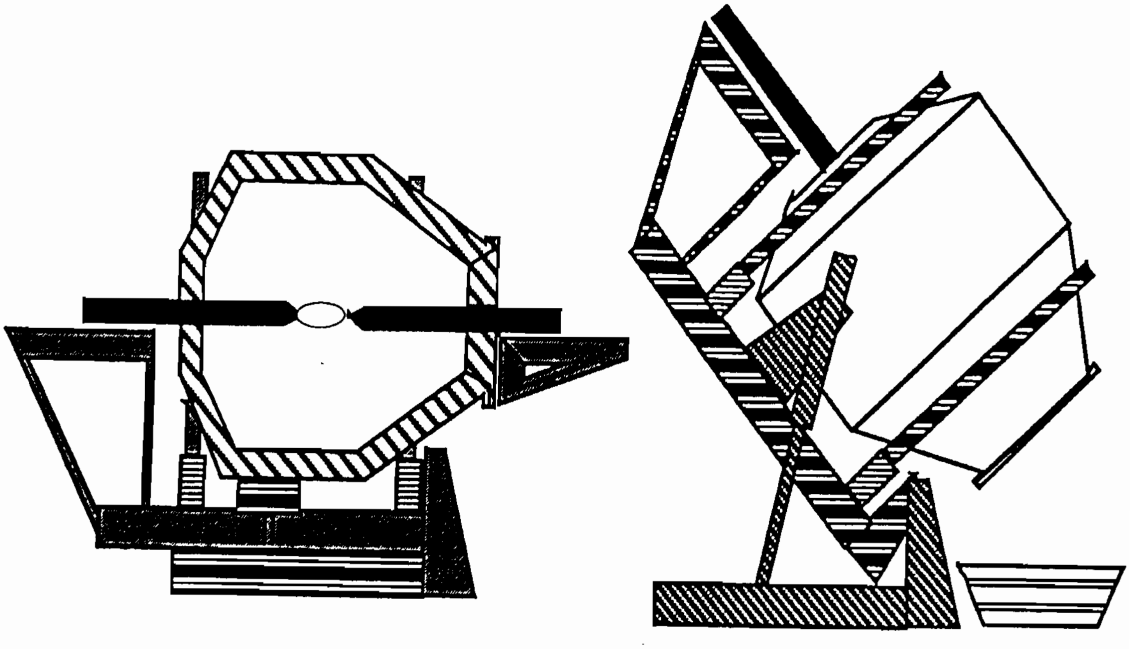

Normal Operation

Discharge

Figure 2-12: The rotary furnace of the Hydro-Quebec process (Drouet et al. 1995).

Table 2-4: The optimal operating parameters of the 600 kW DROSCAR process (Drouet et al. 1995).

Parameters	Mean
Total cycle time	70 minutes
Charging time	10 minutes
Heating time	36 minutes
Dross tumbling time	13 minutes
Aluminum (Al)tapping time	6 minutes
Residue discharge time	5 minutes
Dross treatment capacity	0.87 ton/hour
Energy consumption	371 kWh/ton-dross
Energy efficiency	74.9 %
Al recovery rate (for a 50 % Al dross)	94.7 %
Electrode consumption	0.88 kg/ton-dross

possible. Furthermore since the process uses a graphite arc, there are no-water cooled parts in the furnace, which eliminates the hazard created by possible water leaks over the molten metal.

CHAPTER III

RESEARCH OBJECTIVES

The two main objectives of this study were to examine the arc stability and erosion behavior of a DC hollow graphite cathode struck to a graphite anode in argon at atmospheric pressure. The detailed research objectives and the methodologies used are given below:

1. Arc Stability at a DC Hollow Graphite Cathode

This objective was focused on identifying the electron emission mode transition of graphite arc cathode operation by studying the characteristics of the thermionic and thermofield emission modes. Firstly, total voltage patterns, arc movement and acoustic noise were examined as a function of operating parameters. The chosen parameters were argon gas flow rate, initial interelectrode gap, arc current, and cathode tip geometry. Secondly, the characteristics of each mode were examined through the estimation of current densities, Fast Fourier Transform (FFT) of the total voltage, measurement of the cathode surface temperature, and examination of the cathode surface using scanning electron microscopy.

2. Erosion Behavior of a DC Hollow Graphite Cathode

This objective concentrated on analyzing the erosion behavior of the graphite cathode when arcing to a graphite anode in argon at atmospheric pressure. The erosion rate was measured as a function of argon flow rate, initial interelectrode gap, and arc current.

These parameters were associated with the emission mode transition and the arc stability.

Erosion rates were separated into rates for stable and unstable operation.

CHAPTER IV

EXPERIMENTAL METHODS

4.1. EXPERIMENTAL APPARATUS

The schematic diagram of the transferred arc system for this work is shown in Figure 4-1. The main components of the experimental system were a power supply, a hollow graphite DC cathode, a graphite anode, a data acquisition system to record total voltage and arc current, a gas-tight water-cooled chamber to house the graphite electrodes, an oxygen meter, and a thermohygrometer. All equipment was electrically grounded except the graphite cathode which operated at an elevated negative potential. Argon was used as the plasma gas and its rate was measured in liters per minutes (lpm) at 293 K and 1 atm.

4.1.1. Power Supply

Eight Miller SRH-444 rectifiers (Miller Electric Mfg. Co., Appleton, Wisconsin, USA) connected in series supplied the power to the graphite cathode. Because of this series connection, the arc current was limited to 400 A. Each rectifier had an open circuit voltage of 75 V and a power rating of 19.6 kW. The input voltage was three phases, 575 V at 60 Hz and the total open circuit voltage was 600 V. The rectifier was connected to a control console, which controlled the plasma gas flow rate and the power to the cathode. The console also contained a high frequency starter (HF 2000 High Frequency Arc Starter, Miller Electric Mfg. Co.) and a safety shut-off system which could be deployed in case of an emergency.

4.1.2. The Chamber

The chamber consisted of the roof, the upper chamber, the lower chamber, and the bottom. The inside diameter of the chamber was 29.5 cm, and the height was 29.0 cm.

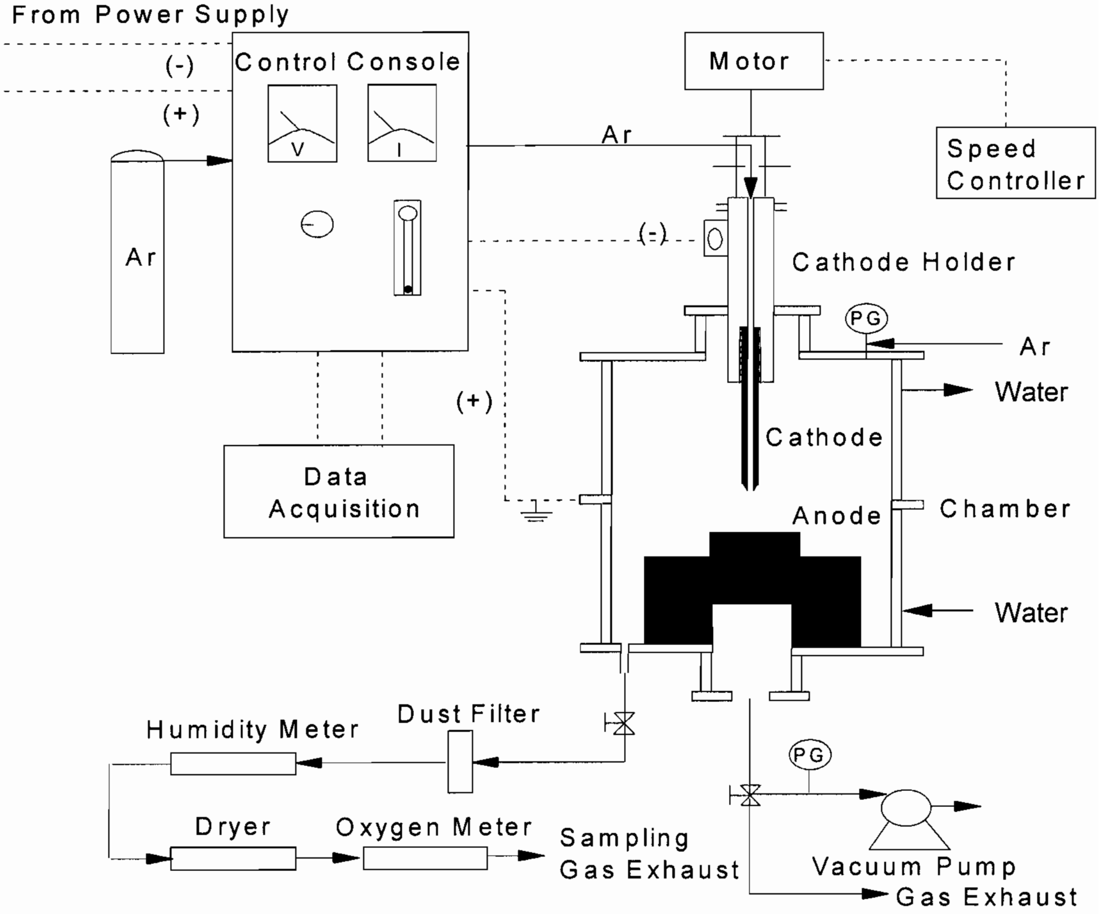

Figure 4-1: The schematic diagram of the transferred arc experimental system.

Two cooling water circuits were connected to the chamber. One was for the roof and the upper chamber, and the other was for the lower chamber and the bottom. The cooling water rate was fixed at 15.6 slpm for the upper part and 7.2 slpm for the lower part.

4.1.3. Hollow Graphite DC Cathodes

Two types of hollow graphite DC cathodes, named cathode I and cathode II, were used in this study. Schematic drawings of the graphite cathodes are presented in Figure 4-2. The length of each graphite cathode was 27.94 cm. The inner diameter of each cathode was 0.32 cm. The only difference between the two cathodes was the size of the outer diameter. The outer diameter of cathode I was 1.91 cm, and that of cathode II was 1.07 cm.

The determination of the outer diameter of cathode II was based on apparent current density. This is defined as ratio of arc current to the cross-sectional area of each cathode. Cathode II was planned to simulate a 1000 A run at real 300 A because of the current limitation of the power supply. The cross-sectional area of cathode I is 2.77 cm^2 and the apparent current density of cathode I at 1000 A is 360 A per cm^2. The outer diameter of cathode II was sized to give this apparent current density at 300 A.

Cathode II was designed to confirm that arcs in the thermionic emission regime do not show the electrical and acoustical noise. The influence of the reduction of the outer diameter of cathode I for the preparation of cathode II may be explained by considering the energy balance on the cathode spot surface. The energy balance, in general, is described by the following equation:

(a) Cathode I

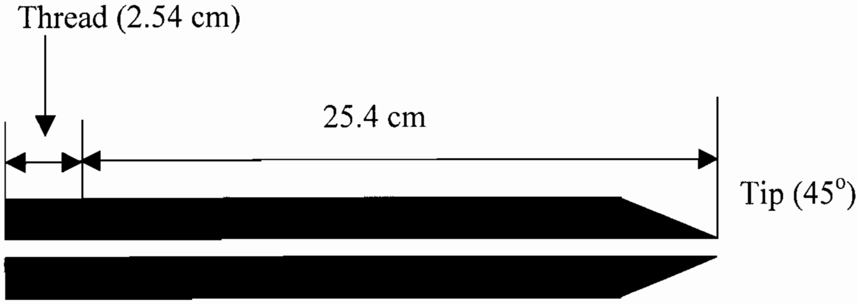

(b) Cathode II

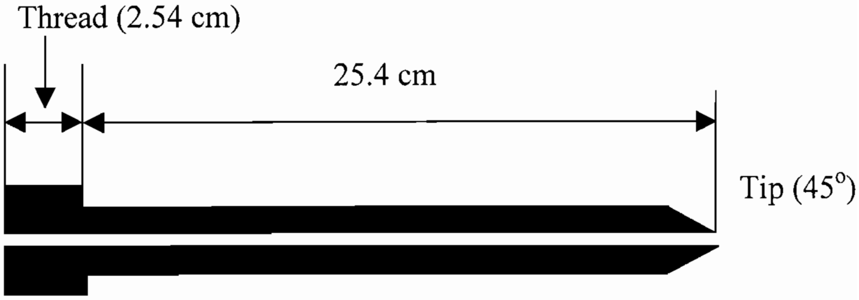

Figure 4-2: The schematic drawing of cathode I and cathode II.

$$q_{\text{ion bombardment}} = q_{\text{vaporization}} + q_{\text{conduction}} + q_{\text{electron emission}} \quad (4\text{-}1)$$

where q is the heat flux at the cathode spot surface. As discussed in chapter II, the ion bombardment is the main component of the energy input; the vaporization of the cathode material, the conduction heat loss through the cathode, and electron emission are the major components of the energy output. Among the energy output components, only the conduction heat loss depends on the geometry of a cathode. Therefore, reduction of the diameter of a cathode can decrease the conduction heat loss, thus providing a higher temperature at the arc root.

The tip of both cathodes was machined to a contained angle of 45°. Both cathodes were connected with the brass water-cooled cathode holder through a 2.54 cm long threaded section. This cathode holder was water-cooled to avoid the melting of the teflon electrical insulator, located in the roof of the chamber. The cooling water rate of the holder was fixed at 4.8 slpm. The length of the both cathodes below the water-cooled holder was 25.4 cm. Argon was injected through the hole of the cathode at flow rates of 0, 4.5, 10, and 15 slpm.

XT grade graphite, produced by POCO GRAPHITE INC., was used in this study as the material for the cathodes and the anode. The graphite is isotropic and has uniform pore size distribution. Physical properties of the graphite at room temperature, provided by POCO GRAPHITE INC., are presented in Table 4-1.

Table 4-1: Physical properties of XT grade graphite at room temperature.

Physical properties	Units	Values
Particle size	microns	20
Total porosity	(% volume)	26
Apparent density	g/cc	1.71
Compressive strength	N/mm^2	86
Flexural strength	N/mm^2	45
Electrical resistivity	μ.ohm.cm	1250
Coefficient of thermal expansion	microns/m °C	7.5
Thermal conductivity	W/m K	115

4.1.4. The Anode

The anode was a graphite disc as shown in Figure 4-3. The XT grade of the POCO Graphite Inc. was used for the anode material. The diameter was 5.72 cm, and the height was 3.18 cm.

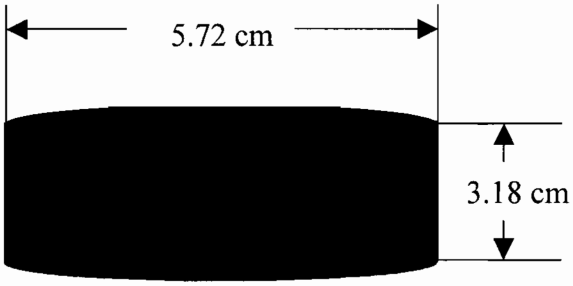

Figure 4-3: The schematic drawing of the anode.

4.1.5. Data Acquisition System

The data acquisition system consisted of a DAS-1401 data acquisition board and a standard personal computer. Control of the data acquisition system was done using a computer program written in BASIC. The sampling time of the data acquisition system was programmed as 8 seconds. The system was used to record total voltage and arc current. The data acquired were saved to an ASCII text file for later processing.

4.1.6. Oxygen Meter

Before each experiment, oxygen (O_2) concentration, relative humidity (RH), and temperature in the chamber were measured to check the purity of an argon atmosphere of the chamber. The GC-502 model of GC Industries located Fremont, California, USA was used to measure the O_2 concentration in the chamber. The measuring range of the O_2 meter is from 0 to 25 volume percent in 0.1 volume percent increments, and at constant ambient temperature the accuracy of the O_2 meter is $\pm$ 0.5 volume percent.

4.1.7. Thermohygrometer

With the O_2 meter, the 37950-10 model thermohygrometer of Cole-Parmer was used to measure the RH and temperature in the chamber. The thermohygrometer measures RH from 0 to 99.9% and temperature from 0^o to 199.9 ^oF.

4.1.8. Optical Pyrometers

For the measurement of the graphite cathode surface temperature, two types of optical pyrometers were used: single wavelength and two-wavelength pyrometers. The single wavelength pyrometer is a model of the Pyrometer Instrument Co., Inc., located in New Jersey, USA. This pyrometer is designed to adjust the filament current to match the color of the filament to that of the object, i.e. it used the disappearing filament principle of temperature measurement. The single wavelength is 0.65μm. Holman (1989) gives the schematic diagram of this type of the pyrometer as presented in Figure 4-4. The radiation from the object is viewed through the lens and filter arrangement. An absorption filter at the front of the pyrometer reduces the intensity of the incoming radiation. Figure 4-5 illustrates the disappearance of the lamp filament for the match as viewed from the eyepiece. If the filament is too cold, it needs an increase of the current; if the filament is too hot, it needs a decrease of the current. The temperature measurement is performed for the null condition.

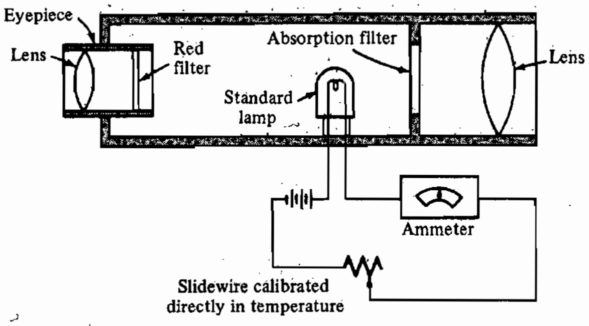

Figure 4-4: The schematic diagram of the single wavelength pyrometer (Holman 1989).

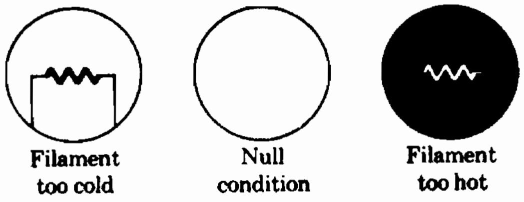

Figure 4-5: Appearance of the lamp filament in eyepiece of the single wavelength pyrometer (Holman 1989).

For the two-wavelength pyrometer, a ROS-8 model pyrometer of Capintec Instruments, Inc., located in Pittsburgh, USA, was used. It detects radiation in the near infrared region of the spectrum at 0.78 and 0.83 μm. The temperature reading of this pyrometer depends on the ratio of the intensities of the object radiation at the two selected wavelengths unlike the single wavelength pyrometer. In addition, for a gray body, knowledge of the absolute values of spectral emissivities is not needed because the emissivity of the gray body is not affected by the wavelength. In that case, Themelis et al. (1962) gave the relevant equation to determine the temperature of the gray body as follows:

$$\ln\frac{W_{\lambda 1}}{W_{\lambda 2}} = \ln[(\frac{\varepsilon_{\lambda 1}}{\varepsilon_{\lambda 2}})(\frac{\lambda_2}{\lambda_1})^5] - [(\frac{1}{T})(\frac{C_2}{\lambda_1} - \frac{C_2}{\lambda_2})] \qquad (4\text{-}2)$$

where W_λ is intensity of non-black body radiation at wavelength λ, ε_λ is emissivity of body at wavelength λ, C_2 (=1.4387 cm · K) is a constant, and T is absolute temperature, K. Equation (4-2) indicates that there should be a linear relationship between the logarithmic ratio of the monochromatic intensities and the reciprocal of the absolute temperature of the object.

4.1.9. Oscilloscope

A TDS 200-series digital storage oscilloscope, produced by Tektronix Incorporation located in Oregon, USA, was used to measure total voltage and to perform its Fast Fourier Transform (FFT) in the order of the ms and μs time scale. This oscilloscope is capable of converting a time-domain signal into its frequency components, thus allowing the FFT analysis of the total voltage measured in the time domain. The single triggering mode was used for the measurement of the total voltage and the FFT to avoid the uncertainties caused by the signal overlapping. The signals and the frequency components captured in this mode were sent to a Hewlett-Packard laser jet printer for hardcopies.

4.2. PARAMETER RANGES

In this study arc current, arc duration, argon gas flow rate, and initial interelectrode gap were used as operating variables. The ranges of these parameters are presented in Table 4-2. The actual interelectrode gap increased as the electrodes eroded and this depended on the operating conditions. The maximum length change of the electrodes was measured to examine the gap change. The maximum length change for the cathode was 0.8 cm. For the graphite anode, the maximum length change was 0.5 cm and this occurred as a hole at the anodic arc root. The plasma gas flow rate greatly influenced length change of the anode since the argon gas cooled the surface. For a flow rate of 0 slpm, the depth of the hole reached a maximum of 0.5 cm, while for a gas flow rate of 15 slpm, the anode remained flat and did not change measurably in length. The final interelectrode gap was determined by these maximun length changes as shown in Table 4-3.

Table 4-2: Parameter ranges of this work.

Operation variables	Units	Ranges
Arc current*	A	150, 300, 400
Arc duration	minutes	10, 30, 60, 90, 120
Argon gas flow rate	slpm	0, 4.5, 10, 15
Initial interelectrode gap	cm	0.5, 1.5, 3.0

*) Standard deviations: 6 A for 150 A, 8 A for 300 A, and 11 A for 400 A.

Table 4-3: The ranges of the final interelectrode gap.

Initial interelectrode gap	Final interelectrode gap
0.5 cm	1.3 ~ 1.8 cm
1.5 cm	2.3 ~ 2.8 cm
3.0 cm	3.8 ~ 4.3 cm

4.3. THE ARGON ATMOSPHERE

Before erosion measurements, the chamber was repeatly filled with pure argon (33 slpm) and evacuated to – 20 in Hg while maintaining a lower argon flow rate (3 slpm). The cycle was repeated five times after which argon was fed at a flow rate of 3 slpm and the chamber pressure was kept slightly above atmospheric pressure. Normally, the oxygen concentration was at the lower limit of the meter 0.1 % and the RH at 1.0 % at 20 ^{o}C. The argon gas was high purity (99.999 %) from PRAXAIR Technology Inc., located

Danbury, Connecticut, USA. Estimation of the graphite consumption mass loss because of the oxygen and the humidity in this argon atmosphere was performed and the procedure is given in Appendix 1. The estimated consumption mass loss was $4.60 \times 10^{-3} \sim 4.54 \times 10^{-2}$ g and was neglected; therefore, the mass change of a graphite cathode before and after a run was directly used for the calculation of erosion rate.

4.4. ARC OBSERVATION

A white screen and lens were used to produce an image of the arc and a digital video camera was employed to record the arc. The bi-convex lens (focal length = 20 cm and diameter = 5 cm) and the screen were installed in front of the window of the upper chamber. The lens produced an inverse image of the arc on the screen. The digital camera was TV 203 model of SONY and had special digital effects that enabled to focus very sharply on the image regardless of the surrounding lighting, etc. At any time the exposure time on the camera could also be changed to produce darker or brighter images. These recorded images were transferred to a computer for further analysis.

4.5. MEASUREMENTS

4.5.1. Measurement of Total Voltage and Arc Current

Total voltage of an arc was measured using a divider circuit. The divider was connected across the cathode and anode at the output of the high frequency generator. Arc current was measured using a shunt which was placed in series with the anode. The outputs of both devices were connected to the data acquisition system.

4.5.2. Measurement of Erosion Rate of the Cathodes

The erosion rate of an electrode (E), in general, has been defined as the mass loss normalized to the total electric charge passing through the cathode and is presented as the following equation:

$$E = \frac{M(\tau)}{\int_0^\tau I(t)dt} \tag{4-3}$$

where M(τ) is the total mass loss of the electrode for an arcing time τ; I(t) is the arc current evolution (Kim, 1995). In this work, the integration in Equation (4-3) was not needed because the average arc current could be obtained from the data file of each run. Therefore, the equation (4-3) was simplified as the following equation:

$$E = \frac{\Delta M}{t * I} \tag{4-4}$$

where ΔM is the total mass loss of the cathode for arc duration, t; I is the average arc current. The total mass loss was determined by measuring the cathode weight before and after each experiment.

4.5.3. Measurement of Cathode Surface Temperature

For the measurement of the cathode surface temperature using the single wavelength pyrometer, a blackbody hole was prepared just above the cathode tip as shown in Figure 4-6. The diameter of the blackbody hole for the both cathodes was 1 mm; the depth of that was 5 mm for cathode I and 2 mm for cathode II. The filament of the single pyrometer was focused on the blackbody hole and thus the color comparison between the filament and the hole was possible. When the two colors were matched, the temperature was recorded.

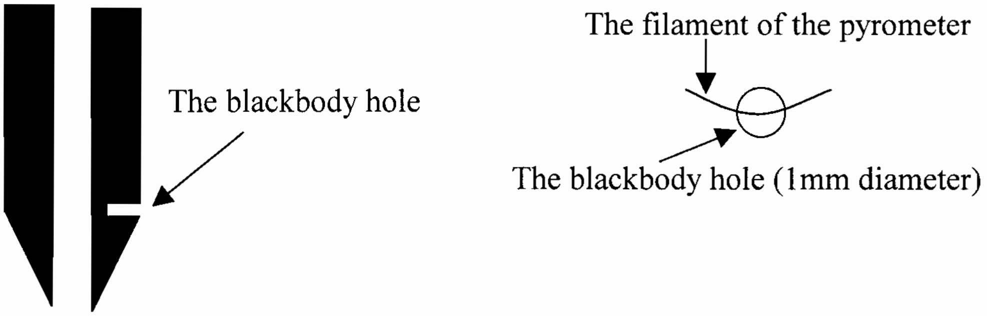

Figure 4-6: The position of the blackbody hole and the overlapping of the filament and the hole.

The two-wavelength pyrometer was installed in front of the widow located in the upper chamber, and it was connected to a strip chart recorder (Graphtec Corp., SR6211) to record the cathode surface temperature. The target size for this temperature measurement was about 5 mm determined using the figure of "target diameter vs. distance to target" in the manual of the two-wavelength pyrometer, provided by Capintec Instrument, Incorporation. The recorder output of the pyrometer is between 0 and 1 V DC full scale. Normal recording paper speed of the chart recorder was 1 mm per minute. Chen (1991), previously used the pyrometer, reported that the intensity of the plasma arc could interfere with the measurement of the surface temperature of a body. Therefore, to estimate the cathode surface temperature without the effect of the arc radiation, the cooling curve of the cathode was recorded. In that case, the recording paper speed was increased to 500 mm per minute as soon as the plasma was shut off.

4.6. EXPERIMENTAL PROCEDURE

4.6.1. Pre-Experimental Preparation

1) The inside of the chamber was cleaned with a vacuum cleaner to remove any debris left from the previous experiment. The cathode and the anode were weighed and their masses were recorded. A new cathode was used for the measurement of the erosion rate. The remainder of the apparatus components were cleaned and assembled. The electrical isolation of the cathode was verified.
2) Argon gas was injected into the chamber according to the procedure previously mentioned for the argon atmosphere. The O_2 concentration, the relative humidity, and the temperature of the inside of the chamber were measured.
3) The cathode and the anode cables were connected with the power supply. The power controller and the emergency stop cables were installed.
4) The internal resistance (about 8 kΩ) of the power supply was inspected.
5) The data acquisition system was inspected.
6) All related utility lines were inspected and cooling water flows were started. Operation of the exhaust vent was verified.
7) The power supply was turned on.

4.6.2. Arc Ignition

In this work, two arc ignition methods were used. The first method was drawing an arc from short circuit, and the second one was using the high frequency generator. The arc drawing method was performed by separating graphite electrodes which were in contact. The contact of the graphite electrodes was verified using a multimeter. Because the anode was fixed, the cathode was lowered to contact the anode using a DC motor controller. The lowering speed of the cathode was 0.04 cm per second to minimize mass loss of the cathode when the electrodes contacted. To draw an arc, the cathode was lifted up relatively quickly. The speed of the lifting was 0.1 cm per second. As soon as the arc ignited, the current was increased to 100 A to help in drawing the arc. This method was employed to avoid the electrical interference caused by the high frequency generator and thus allow the voltage and the current to be recorded from the beginning of the arc ignition. In the high frequency generator method, the most common arc ignition method currently used in transferred arc plasma systems, the cathode was lowered to within a few millimeters of the stationary anode surface and then a high frequency spark was struck between the electrodes. The high frequency generator method was used to measure erosion rates without the mass loss due to the contact. For 150 A experiments the drawing an arc method was used, and for 300 and 400 A experiments the high frequency generator method was used.

4.6.3. Execution of an Experiment

1) The argon gas flow rate, the initial interelectrodes gap, and the current were adjusted to their desired levels.

2) The data acquisition was begun. For the drawn arc method there was no time delay from arc ignition to the start of the data acquisition system. In case of the high frequency generator method, however, the time delay was approximately 3 minutes since the computer could only be started after the high frequency was off.
3) An experiment was terminated by shutting down the rectifier bank. Argon and cooling water were continued until the apparatus had cooled.

4.6.4. Post Experimental Procedure

1) The cathode and the anode were cleaned with a brush or a compressed air duster to remove soot attached on the surfaces of the electrodes.
2) The cathode was weighed to determine its mass loss during the experiment.
3) Average arc current was obtained from the ASCII text file of the data acquisition.
4) Erosion rate of the cathode was calculated.

CHAPTER V

EQUILIBRIUM COMPOSITION

A free energy minimization was performed to calculate the equilibrium composition as a function of temperature. It was aimed at understanding the behavior of carbon and ionized species under a high temperature condition in the argon atmosphere at atmospheric pressure. The Outokumpu HSC Chemistry Program (Roine, 1994) was used for the calculation of the equilibrium compositions. The equilibrium compositions calculated was limited because chemical species available in the database of the HSC program were restricted. Also, thermodynamic equilibrium in the chamber could not be expected due to the temperature distribution in the chamber.

5.1. SPECIES CONSIDERED

The carbon species considered here were C (s), C (g), C_2 (g), C_3 (g), C_4 (g), C_5 (g), C (+g), C (-g), C_2 (+g), and C_2 (-g). The s in the parentheses stands for a solid compound and the g represents a gaseous one. The +g and the -g mean charged compounds, positive and negative gaseous species, respectively. The electron was also included in this calculation for the ionization of gaseous compounds. Diamond was excluded since it was thought that diamond was not produced under this condition. For the calculation of the equilibrium composition, the HSC program needs the charge balance between positive and negative species of input compounds. Therefore, 1E-20 moles of C_2 (+g) and 1E-20 moles of C_2 (-g) were initially given in the input condition. For the argon gas species, Ar (g) and Ar (+g) were used.

5.2. EQUILIBRIUM COMPOSITION

Figure 5-1 presents the equilibrium composition as a function of temperature. For the calculation, the system pressure was 1 bar, and the molar ratio of the argon gas to the solid carbon species was 1. For this program, the increase of the number of moles of the argon gas, i.e. the increase of the molar ratio, did not affect the equilibrium composition of the carbon species. However, as the ratio is increased, the lowering of the ionization energies of the species in the vicinity of charged particles may be expected because the densities of charged particles are increased, thus providing higher fields and lowering the ionization energies.

In Figure 5-1, the input mole of the solid carbon (1 mole) starts to drop sharply at about 3200 K. That is vaporization of the solid carbon. Before this temperature, the number of the input moles of the solid carbon is constant because there is no oxygen in the argon atmosphere. After the vaporization of the solid carbon, C (g), C_2 (g), C_3 (g), C_4 (g), and C_5 (g) starts to appear at about 4000 K. The carbon species of C (g), C_2 (g), and C_3 (g) are noticeable, but C_4 (g) and C_5 (g) are negligible in this calculation. Therefore, in the figure only C (g), C_2 (g), and C_3 (g) are presented. According to Mentel's study (1978), the temperature of graphite vapor jets was between 4000 and 5000 K. In this temperature range, it can be expected that several carbon species exist and they may be the source of the carbon redeposition, which has been reported for carbon arcs producing fullerences. Between 5,000 and 10,000 K, C (g) is the most stable component among the carbon species. After 10,000 K, equilibrium moles of C (g) start to decrease greatly because of its ionization; its ionization energy is 11.3 eV. Also, the ionization of Ar (g) appears; the ionization energy of argon gas is 15.7 eV. Over than 20,000K, uncharged species almost do not exist and C (+g), Ar (+g), and electrons are major components.

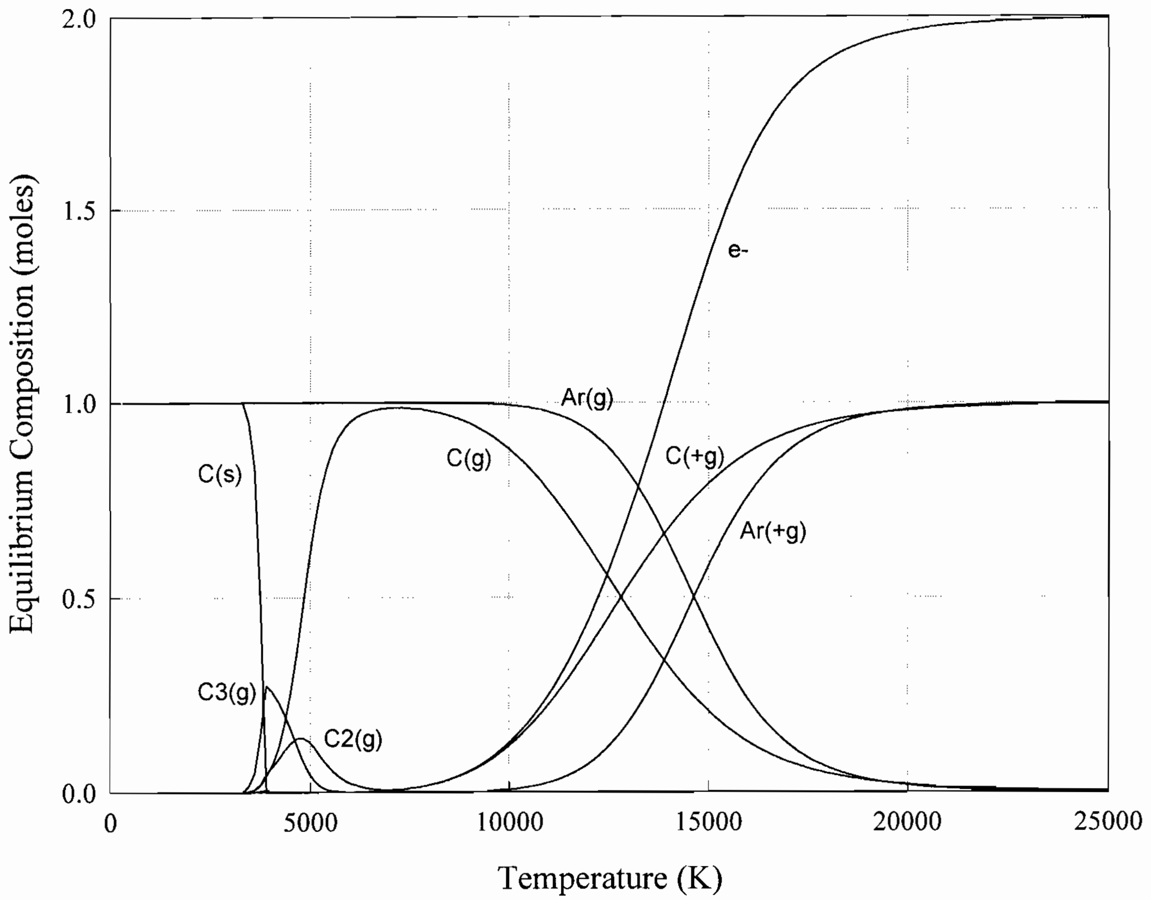

Figure 5-1: Equilibrium composition of the carbon and argon components as a function of temperature. Input compositions are argon (g) 1 mole, C_2 (+g) 1E-20 mole, C_2 (-g) 1E-20 mole, and C (s) 1 mole.

CHAPTER VI

RESULTS AND DISCUSSIONS

This chapter consists of three parts: 1) characteristics of the arcs, 2) the arc stability at the hollow graphite cathode, and 3) the erosion behavior of the hollow graphite cathode. The first part includes interpretation of the total voltage as a function of the operating conditions. Arc pictures are also presented. The second part deals with identification of the mode transition of the cathode. This is followed by the erosion behavior of the cathode.

6.1. CHARACTERISTICS OF THE ARCS

6.1.1. Total Voltage Patterns

In this work, two completely different total voltage patterns appeared as a function of the operating conditions and the geometry of the cathode. One is almost constant total voltage pattern termed “stable” operation; the other is great fluctuation of total voltage pattern termed “unstable” operation as shown in Figures 6-1, 6-2, and 6-3. These figures present typical total voltage patterns of the stable and the unstable arcs recorded at 150 A. Total arc duration in these figures was separated into 3 regimes; initial, stable, and unstable arc duration. The initial arc duration of 3 minutes is introduced for only 150 A runs due to the arc drawing method, which did not have the time delay (3 minutes) for the start of the data acquisition system.

As shown in Figure 6-1, for the stable operation the total voltage was almost unchanging, but for the unstable operation in Figures 6-2 and 6-3, some time after the arcs ignited, the total voltage fluctuated greatly with time. This fluctuation was one of the characteristics of the unstable operation. A run displaying this unstable part always started in stable arc region. This initial stability was associated with a sharp cathode tip; before the cathode tip eroded, the arcs were always stable; after the cathode tip eroded, the fluctuation of the total voltage appeared according to the operating conditions. Details are presented later (see 6.2.2. Effect of the Cathode Tip Geometry on The Arc Stability). The stable arc duration before unstable operation was not constant. It was different for different operating conditions and even for different experiments under the same operating conditions. For EXP-21 the stable arc operation time was about 63 minutes and the unstable arc duration was about 54 minutes as shown in Figure 6-2. Figure 6-3 shows another total voltage pattern recorded at the same operating conditions of EXP-21. In this case, the stable arc operation and the unstable arc operation times were 73 and 44 minutes, respectively. It was thought that this difference might be related to different graphite cathode tip surface conditions and random ignition positions. The raw data of the operating conditions as well as the erosion rates measured in this study are included in Appendix 2 and 3. In case of 300 and 400 A experiments, the trends of the total voltage patterns were similar. Some total voltage patterns recorded at 300 and 400 A runs are introduced below.

The arc operation change from the stable to the unstable region was associated with the appearance of an acoustical noise and a sudden increase of the voltage, normally a few volts. The acoustical noise is associated with the arc power fluctuations. At this time stretched arcs could be seen through visual observation of arcs, performed by the digital camera. In addition, the anodic arc root moved radially outward from its normal location beneath the cathode.

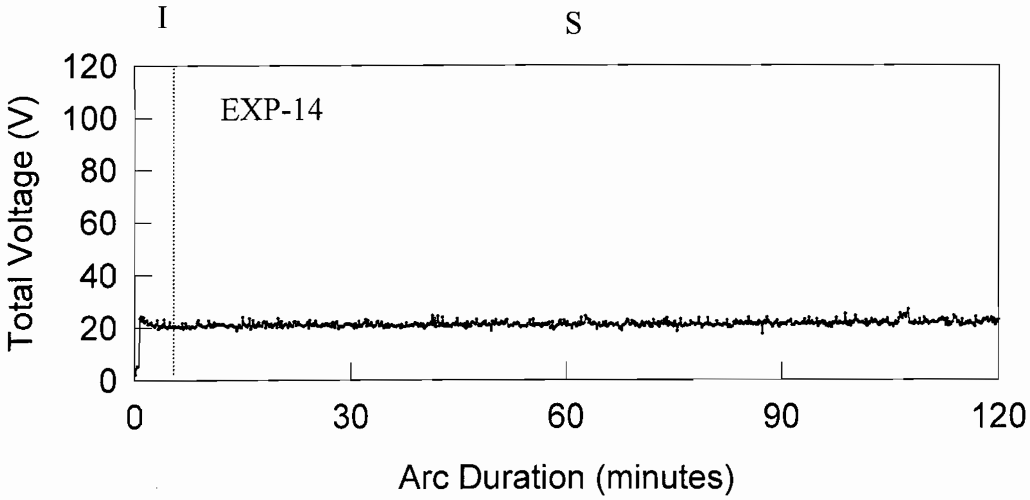

Figure 6-1: Typical total voltage pattern of the stable operation using cathode I for an initial interelectrode gap of 0.5 cm, an argon gas flow rate of 15 slpm, and an arc current of 150 A. I stands for initial arc duration (3 minutes); S is for stable arc duration (117 minutes).

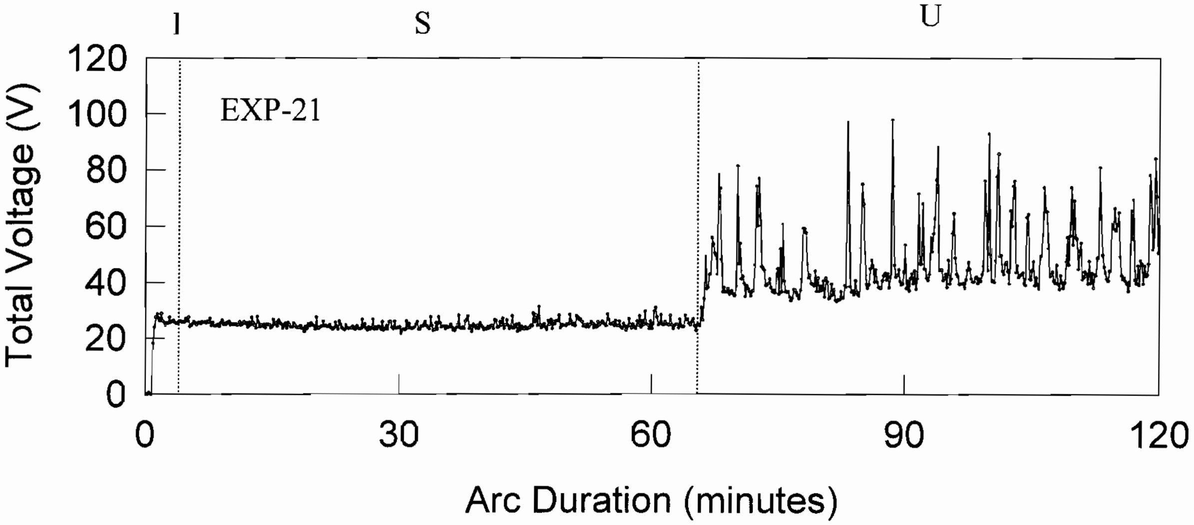

Figure 6-2: Typical total voltage pattern of the unstable operation using cathode I for an initial interelectrode gap of 3.0 cm, an argon gas flow rate of 4.5 slpm, and an arc current of 150 A. I stands for initial arc duration (3 minutes); S is for stable arc duration (63 minutes); U is for unstable arc duration (54 minutes).

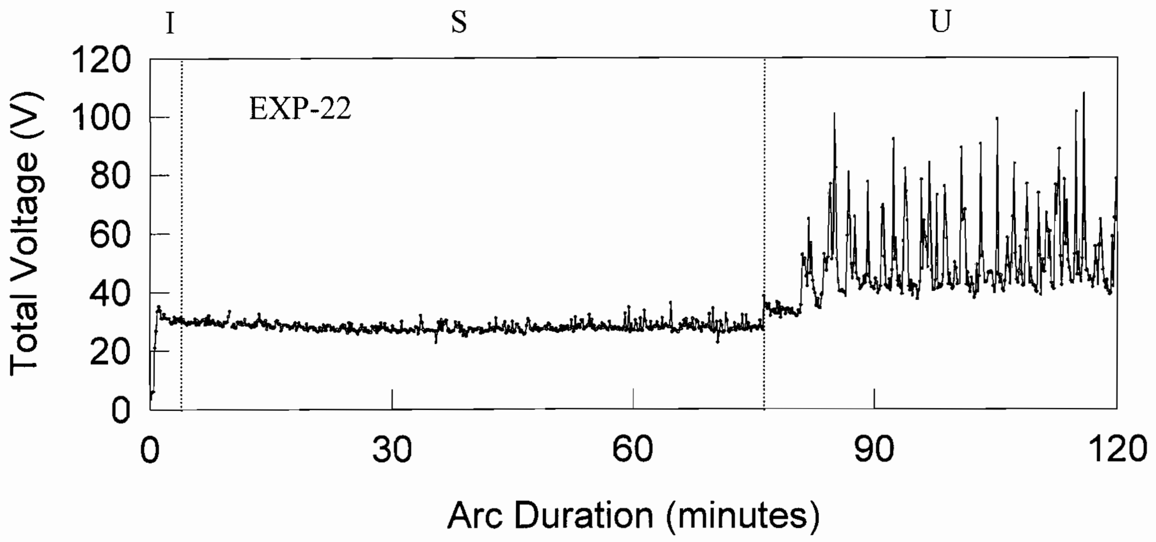

Figure 6-3: Typical total voltage pattern of the unstable operation using cathode I for an initial interelectrode gap of 3.0 cm, an argon gas flow rate of 4.5 slpm, and an arc current of 150 A. I stands for initial arc duration (3 minutes); S is for stable arc duration (73 minutes); U is for unstable arc duration (44 minutes).

6.1.2. Influence of Initial Interelectrode Gap on Total Voltage

Figures 6-4 and 6-5 show the influence of the initial interelectrode gap on the total voltage. Since the graphite cathode was eroded with the time, the average values of the total voltage between 3 and 6 minutes of the stable operation are used in these figures. As the initial interelectrode gap rose, the total voltage increased because the rise of the initial interelectrode gap provided higher arc length. This was expected since arc resistance increases with arc length. The slope, i.e. $\Delta V/\Delta gap$, for the run at 0 slpm is higher than other runs. This slope represents strength of the mean electric field between the electrodes; the arc current divided by this slope, i.e. $I / (\Delta V/\Delta gap)$, is the electrical conductivity between the electrodes. A higher slope, therefore, means higher electric field and lower electrical conductivity at a constant current. It could be seen that the injection of the argon gas reduced the slope and thus increased the electrical conductivity. It seems that the argon gas might wash out condensed carbon particles, thus causing enhanced the argon atmosphere and the increase of the electrical conductivity.

Figure 6-6 presents a comparison of the total voltage between cathode I and II for an argon gas flow rate of 15 slpm and an arc current of 300 A. The total voltage of cathode II was always higher. It appeared that the reduced outer diameter of cathode II might provide increase of the total resistance of cathode II and influence electrical properties of the arcs, thus offering the higher total voltage of cathode II. The total resistances of the cathodes measured at room temperature are 0.34 Ω for cathode I and 0.46 Ω for cathode II.

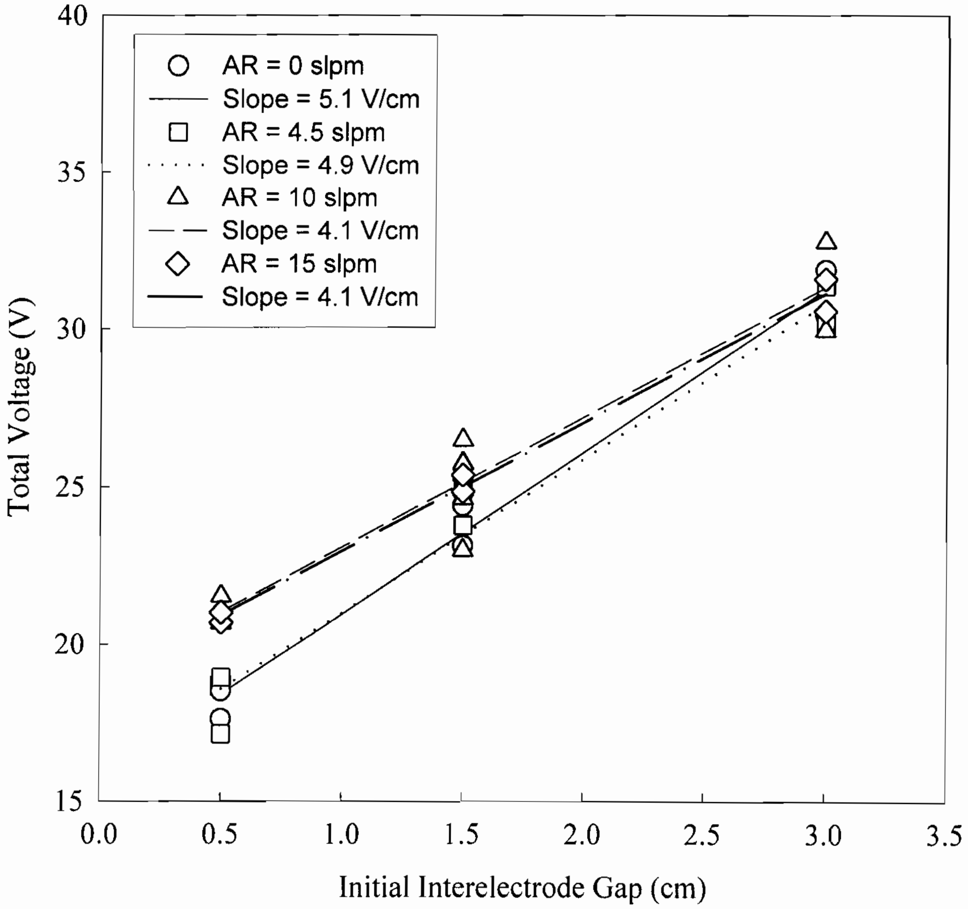

Figure 6-4: Total voltage as a function of the initial interelectrode gap using cathode I at 150 A.

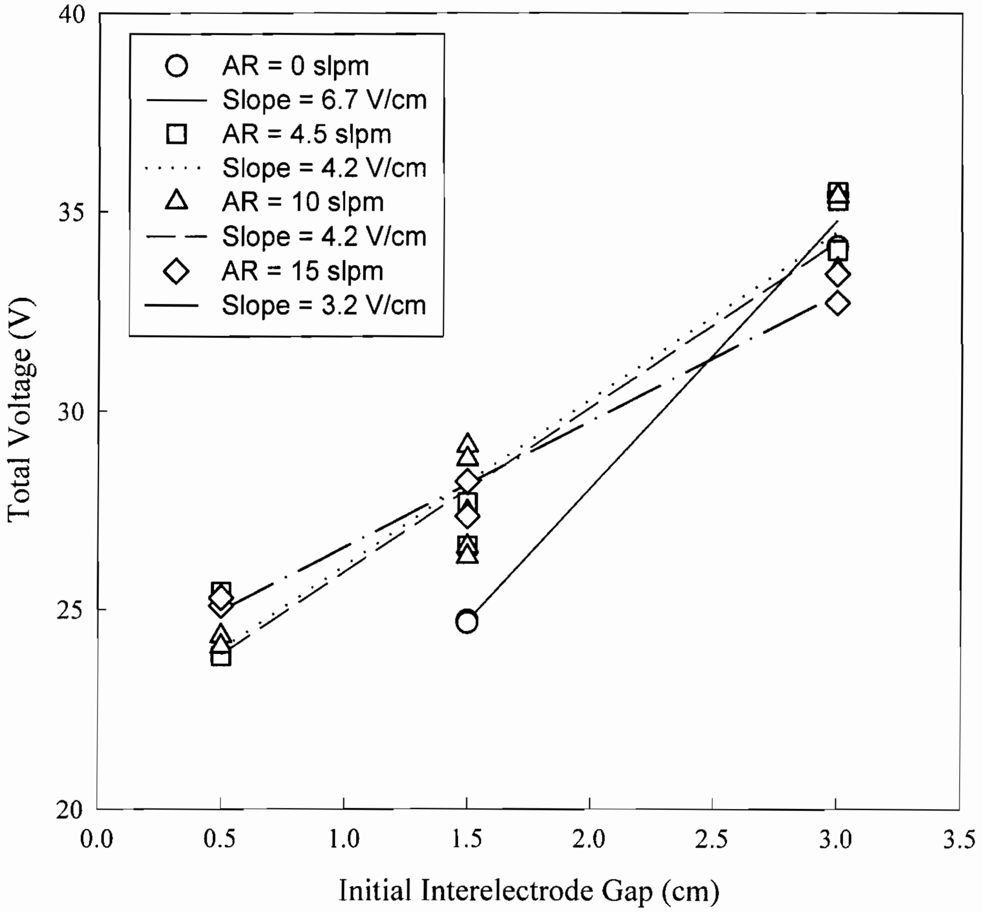

Figure 6-5: Total voltage as a function of the initial interelectrode gap using cathode I at 300 A.

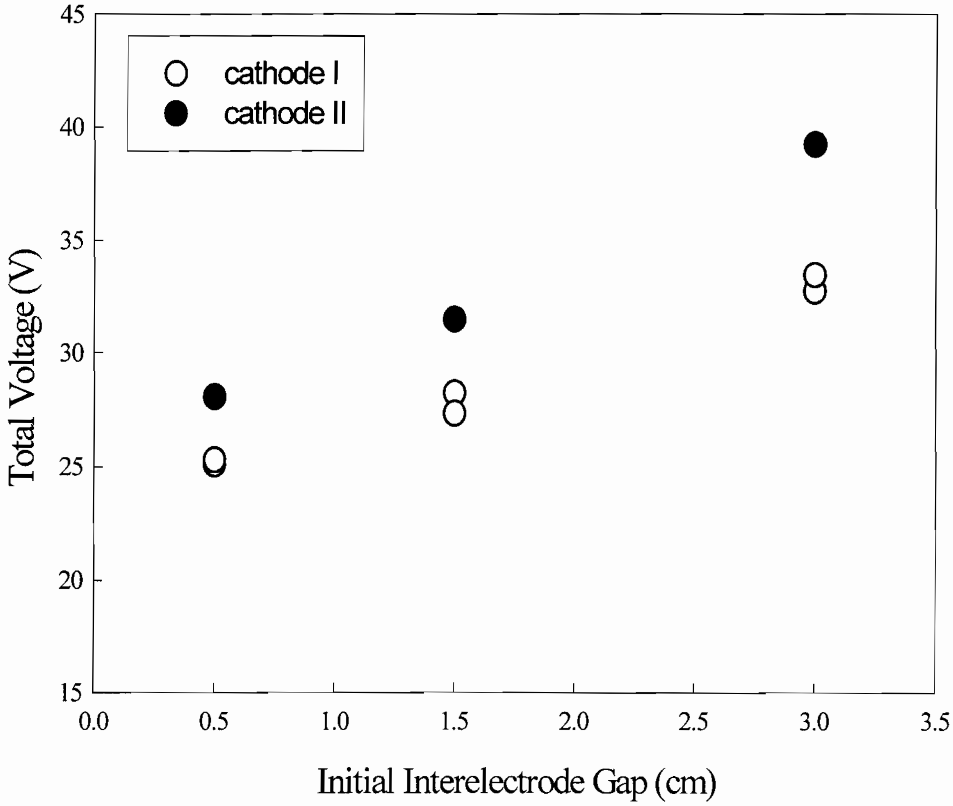

Figure 6-6: Comparison of the total voltage between cathode I and II for an argon gas flow rate of 15 slpm at 300 A.

6.1.3. Influence of Argon Gas Flow Rate on Total Voltage

The influence of the argon gas flow rate on the total voltage is presented in Figures 6-7 and 6-8. The average values of the total voltage between 3 and 6 minutes of the stable operation are used. Pfender et al. (1989) stated that an increase of gas flow rate causes enhanced cooling of the arc fringes, thus providing a higher rate of ionization in the core of the arc column to compensate the electron losses of the arc fringes. This also increases the field strength, and therefore, the arc voltage has to rise. In addition, Mehmetoglu (1980) reported the effect of the argon gas flow rate on the arc voltage in a transferred-arc plasma using tungsten electrodes; the arc voltage increased with the argon gas flow rate. His experimental conditions were arc currents of 150, 250, and 350 A, interelectrode gaps of 4, 6, 8, and 10 cm, and argon gas flow rates of 14, 17, and 20 slpm. He stated that the influence of the argon gas flow rate was almost negligible for short arcs, but was significant for long arcs. His conclusion about this effect could not be directly compared with the results of this work because of the different operating conditions, especially the interelectrode gap. The shortest interelectrode gap of his work was 4 cm, while the longest initial interelectrode gap of this study was 3 cm. In this work, it was thought that at 0.5 and 1.5 cm, the voltage increased slightly with increasing argon gas flow rate, but at a gap of 3.0 cm the effect of gas flow rate on voltage was negligible. An important difference between this work and work with transferred arcs to metal cathodes is that the latter had a converging section through which the gas was injected. In the present work the gas enters through a constant diameter hole in the middle of the cathode so that the argon gas jets leaving the cathode are relatively weaker and thus changes in gas flow rate have little effect on the voltage.

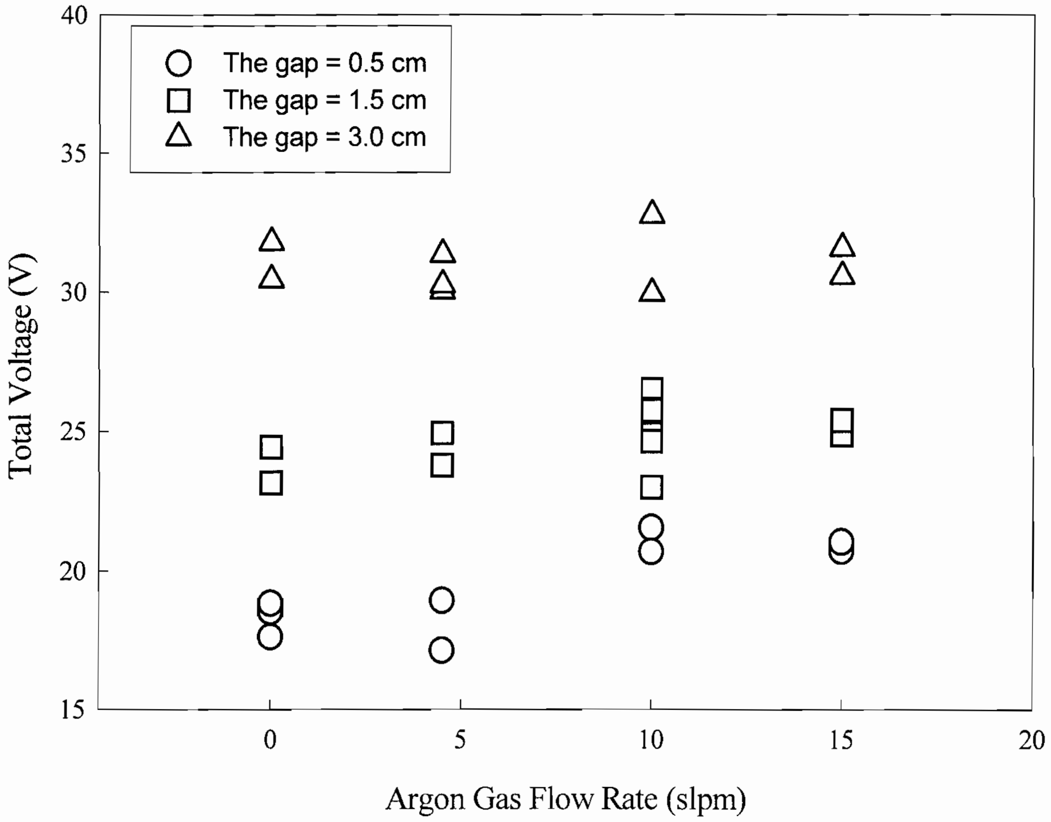

Figure 6-7: Total voltage as a function of the argon gas flow rate using cathode I at 150 A.

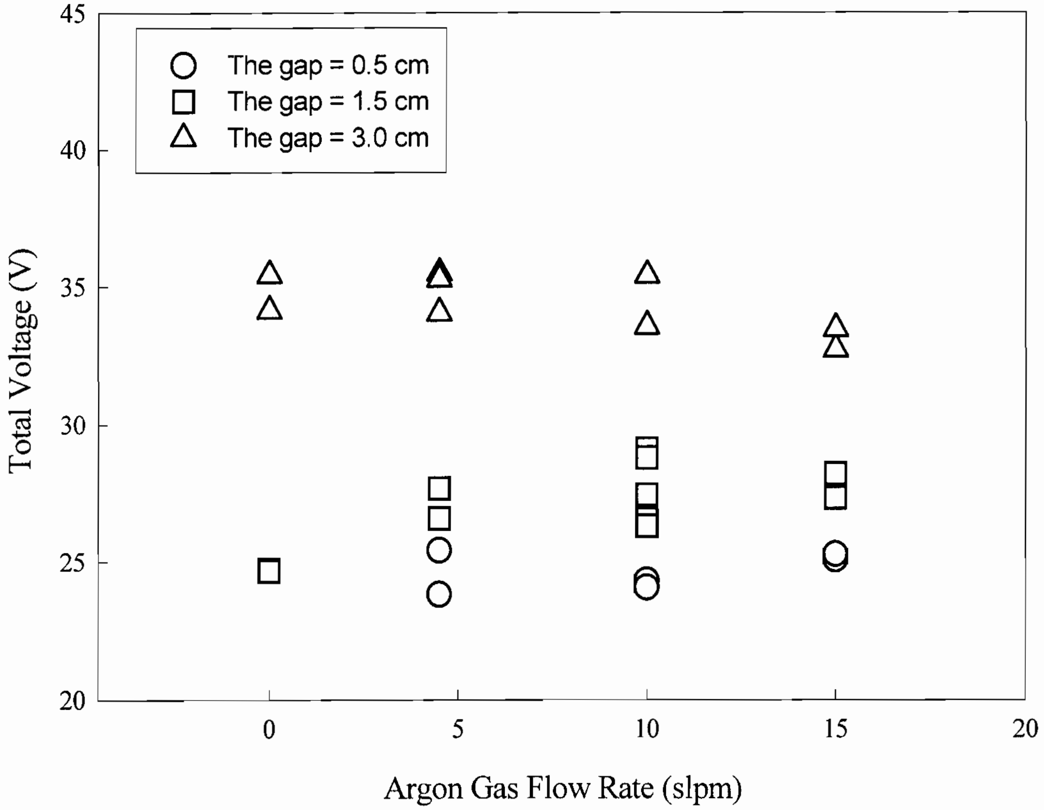

Figure 6-8: Total voltage as a function of the argon gas flow rate using cathode I at 300 A.

6.1.4. Voltage-Current (V-I) Characteristic

The V-I characteristic of the hollow graphite cathode is a slowly rising characteristic as presented in Figure 6-9. Roth (1995) stated that generally the arc regime in more than 20 to 50 A are called the thermal or high intensity arcs and their V-I characteristics are a nearly flat or slowly rising like the V-I characteristic of this work. This V-I characteristic confirms that arcs in this study are in the thermal arc regime. The rise of the total voltage with the increase of the argon gas flow rate discussed in section 6.1.3 is also evident in Figure 6-9.

6.1.5. Visual Observation of The Arcs

This visual observations and digital video camera photography were used to characterize the behavior of the arcs. This also included the distinction between the stable and the unstable arcs, by considering the voltage at any moment.

6.1.5.1. Arc Observation of Cathode I

Arc pictures for the stable and the unstable arcs of cathode I are presented in the following figures. The operating conditions selected for this run were a current of 300 A, an initial interelectrode gap of 3.0 cm, and an argon gas flow rate of 4.5 slpm. The total voltage pattern of this run is presented in Figure 6-10. The experiment ran for 60 minutes; the first 18 minutes fell into the stable region and the rest was unstable. A schematic drawing of this visual arc observation is presented in Figure 6-11.

The pictures in Figure 6-12 were taken at random intervals during the stable arc

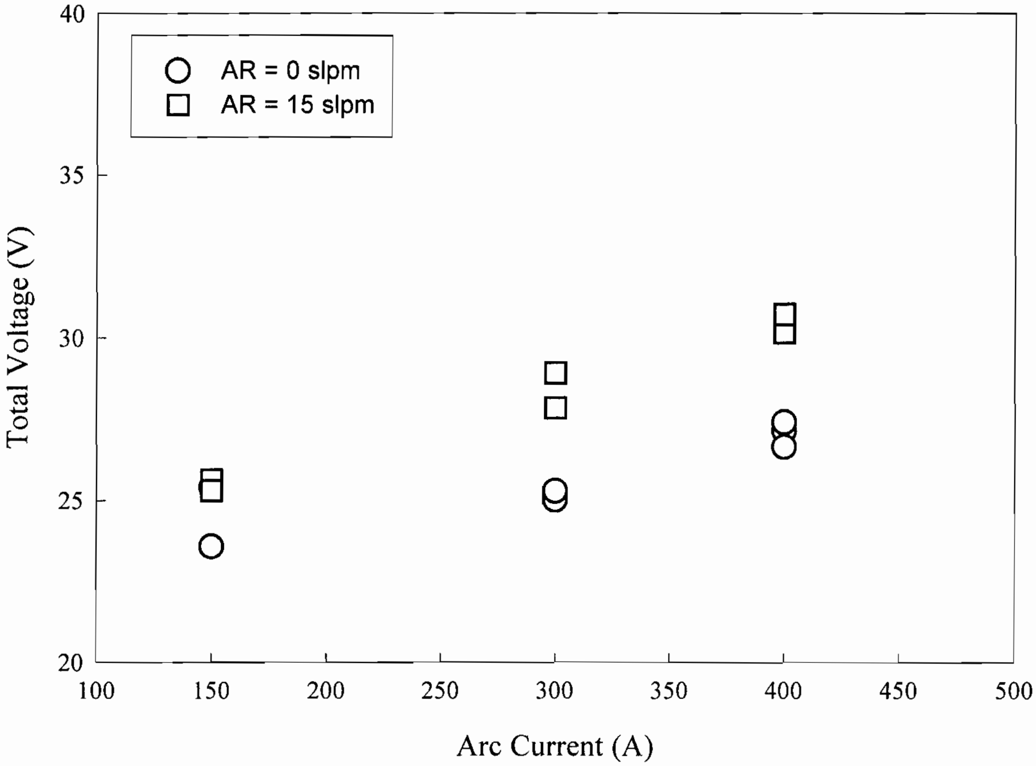

Figure 6-9: Voltage-current (V-I) characteristic of the arcs using cathode I for an initial interelectrode gap of 1.5 cm.

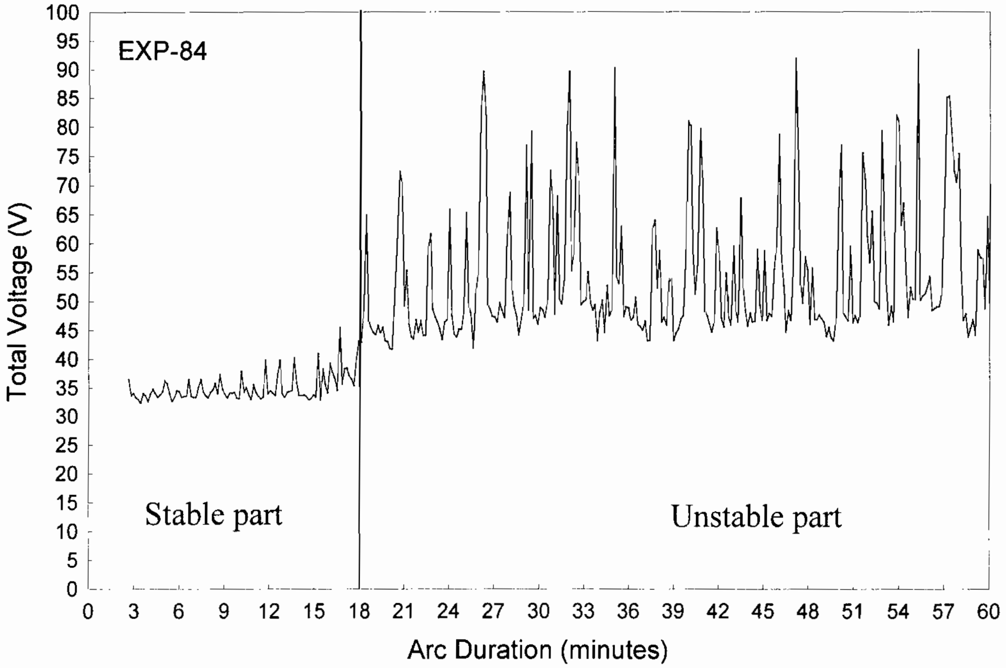

Figure 6-10: Total voltage pattern of an unstable arc recorded using cathode I for an initial interelectrode gap of 3.0 cm, an argon gas flow rate of 4.5 slpm, and an arc current of 300 A.

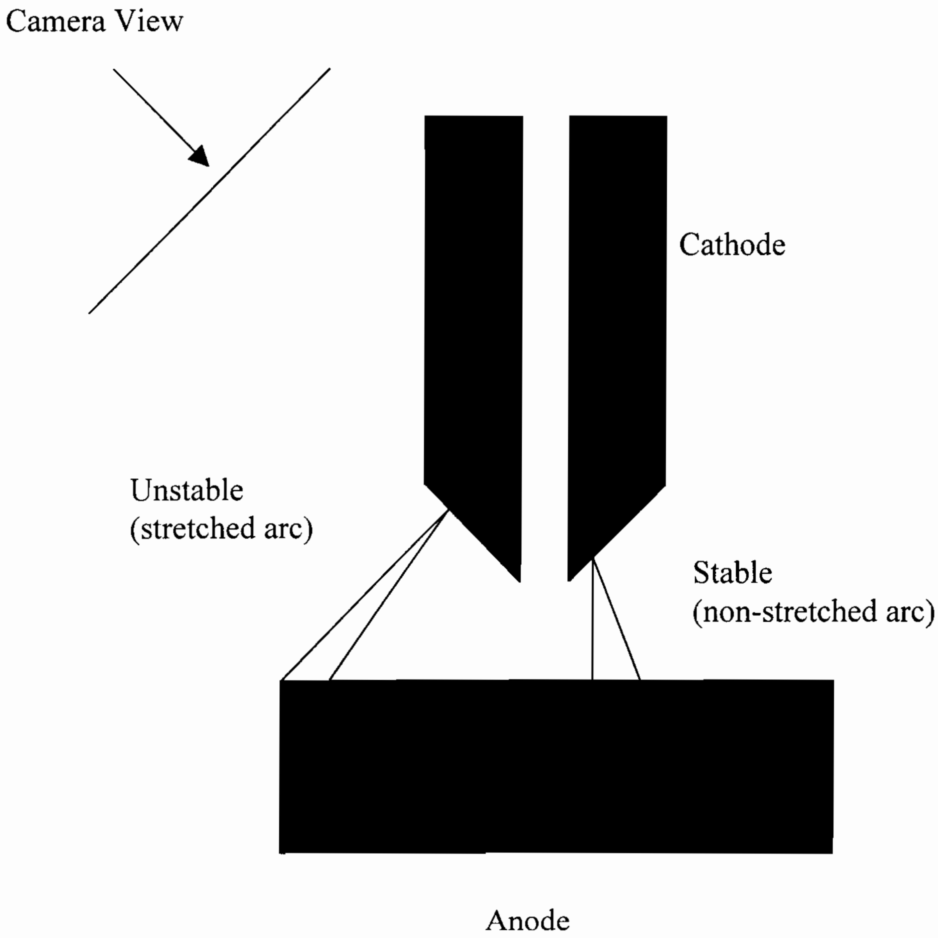

Figure 6-11: The schematic diagram of visual arc observation

operation. The exposure time on the camera was changed to make the pictures brighter. The unit of the exposure time is arbitrary. In the stable arc operation the arc was not stretched, but sometimes, at the end of the stable operation, the arc started to be stretched with small voltage fluctuations as shown in the total voltage between 15 and 18 minutes in Figure 6-10. At that time the arc looked like picture (e) in Figure 6-12. Pictures for the unstable arc operation were randomly taken 18 minutes after the arc started and are presented in Figure 6-13. When the arc was unstable, it was highly stretched and touched the anode at a radial position far from location directly beneath the cathode. Acoustical noise could be heard at this time. Also, in this case anodic vapor jets were easily visible. These vapor jets often contacted the arc and were very fast moving. The connecting vapor jets are presented in pictures (b), (c), (g), (i), (l), (m), and (r) in Figure 6-13.

Figure 6-14 shows 33 sequential pictures of the unstable arc taken within 1 second using the digital camera. The pictures were taken at 48 minutes 55 seconds after the arc started. This figure provided good information about the connection between the arc and the anodic vapor jets for an unstable arc. In these pictures the movement of the anodic vapor jets could also be seen; the vapor jets moved even in less than 1 second. It is believed that this movement is good evidence of how fast the vapor jets move. The connecting anodic vapor jet is normally present in one stream but sometimes even up to three streams were observed.

6.1.5.2. Arc Observation of Cathode II

Arc pictures of cathode II are presented in Figures 6-16 and 6-18. The operating

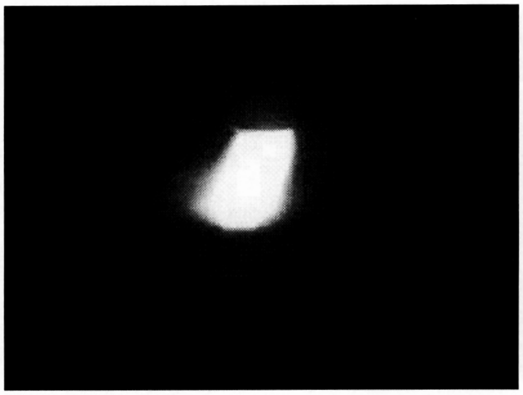

(a) Voltage=30 V, Exposure=8

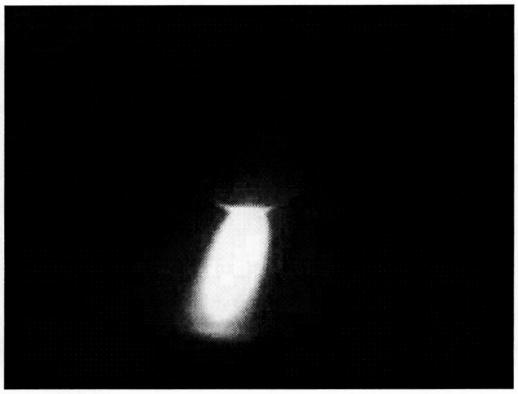

(d) Voltage=31 V, Exposure=12

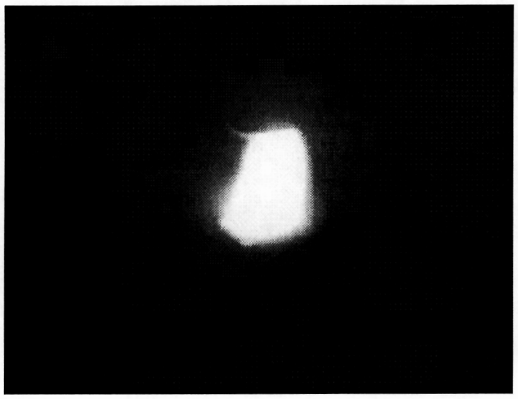

(b) Voltage=33 V, Exposure=9

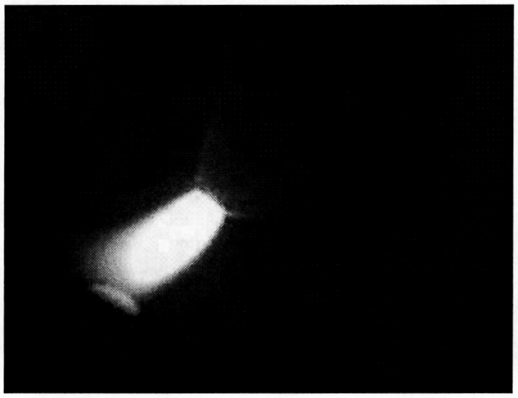

(e) Voltage=37 V, Exposure=11

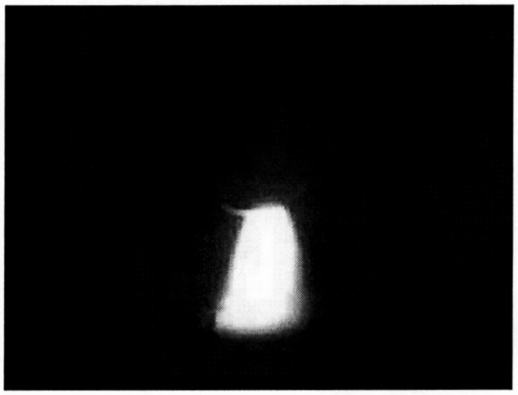

(c) Voltage=31 V, Exposure=11

Figure 6-12: Arc pictures randomly taken for the stable arc operation of EXP-84.

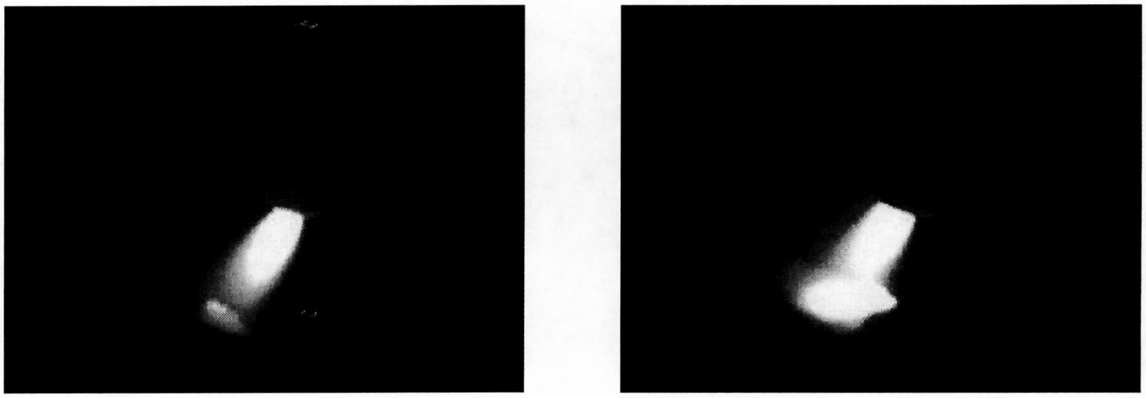

(a) Voltage=45 V, Exposure=8

(d) Voltage=43 V, Exposure=8

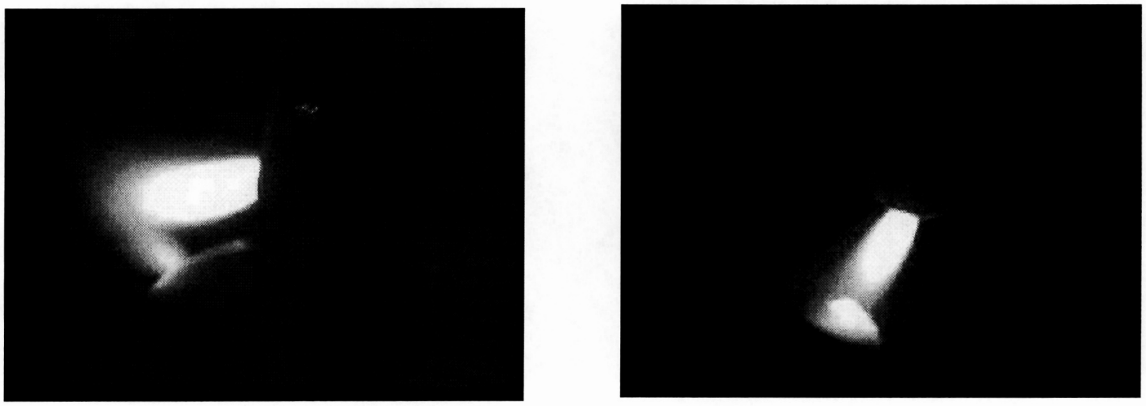

(b) Voltage=60 V, Exposure=11

(e) Voltage=45 V, Exposure=9

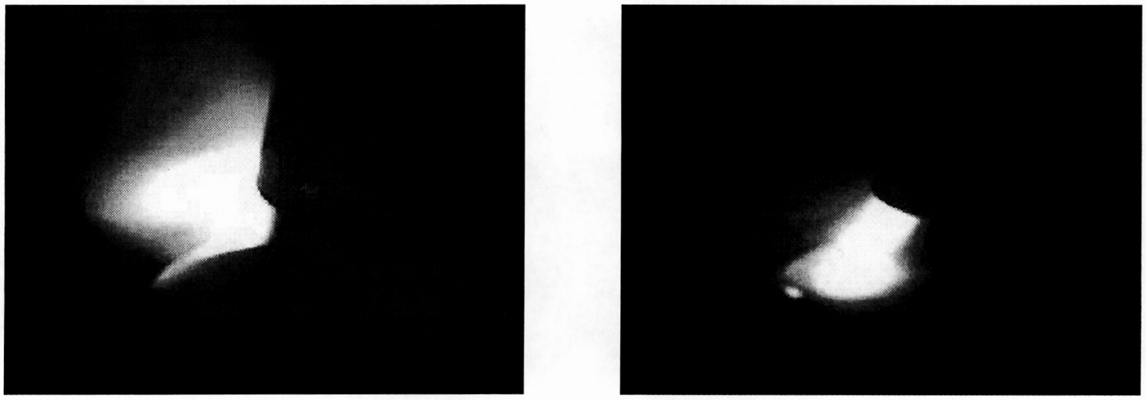

(c) Voltage=70 V, Exposure=11

(f) Voltage=45 V, Exposure=9

Figure 6-13: Arc pictures randomly taken for the unstable arc operation of EXP-84.

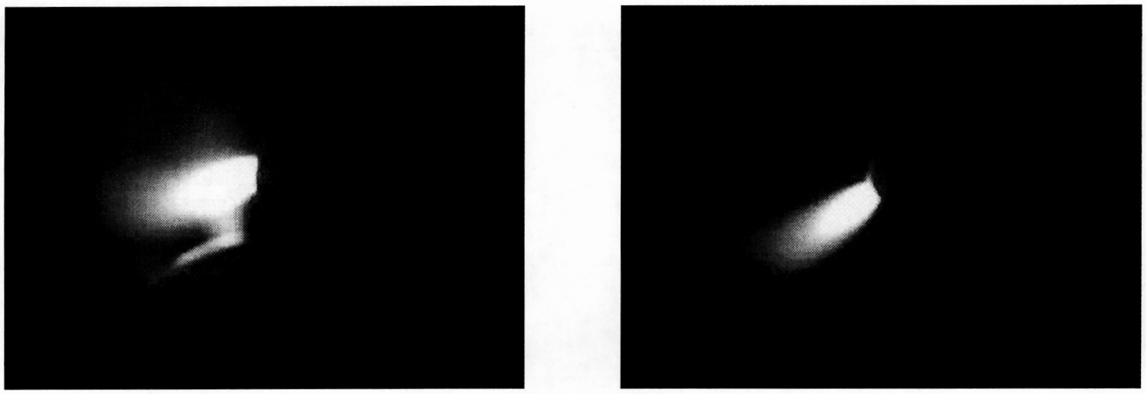

(g) Voltage=70 V, Exposure=9

(j) Voltage=80 V, Exposure=8

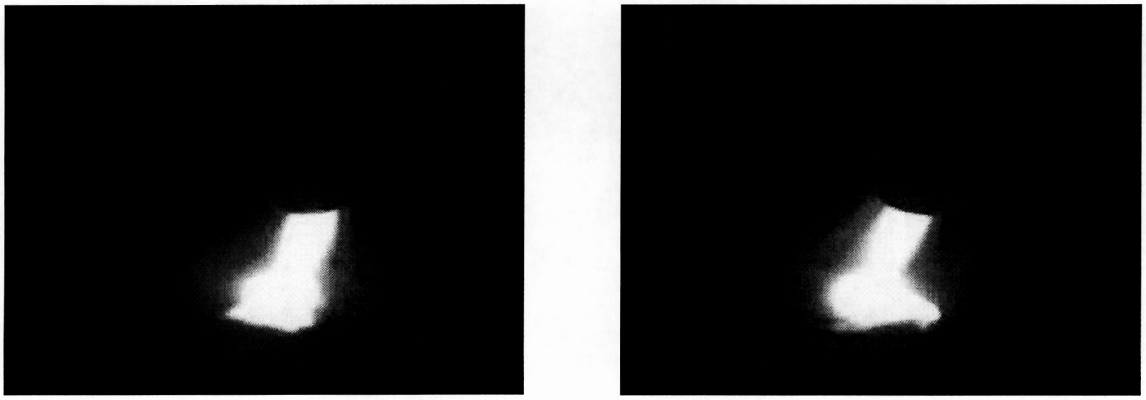

(h) Voltage=42 V, Exposure=9

(k) Voltage=47 V, Exposure=9

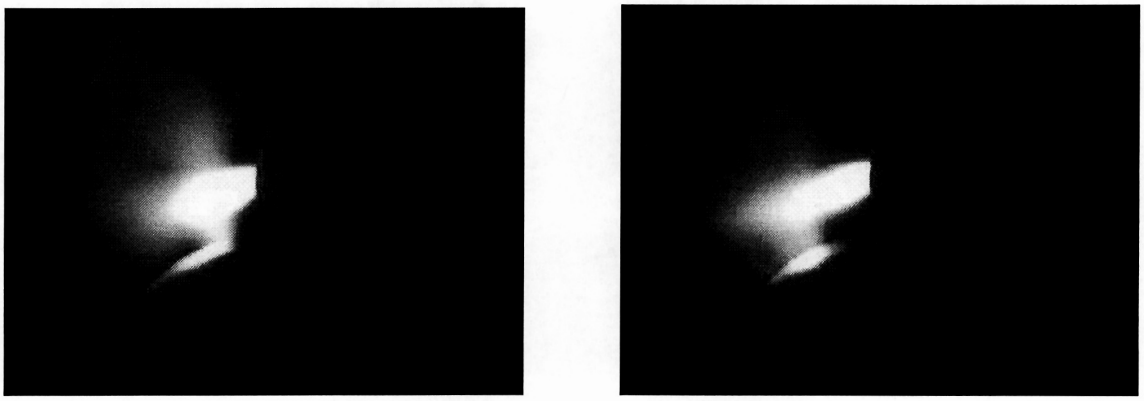

(i) Voltage=80 V, Exposure=9

(l) Voltage=81 V, Exposure=8

Figure 6-13: Arc pictures randomly taken for the unstable arc operation of EXP-84. (continued)

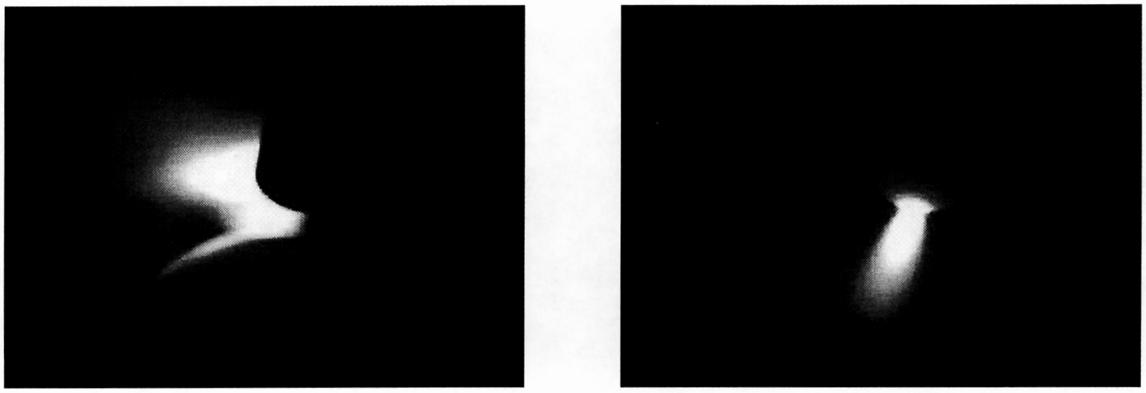

(m) Voltage=75 V, Exposure=8

(p) Voltage=75 V, Exposure=8

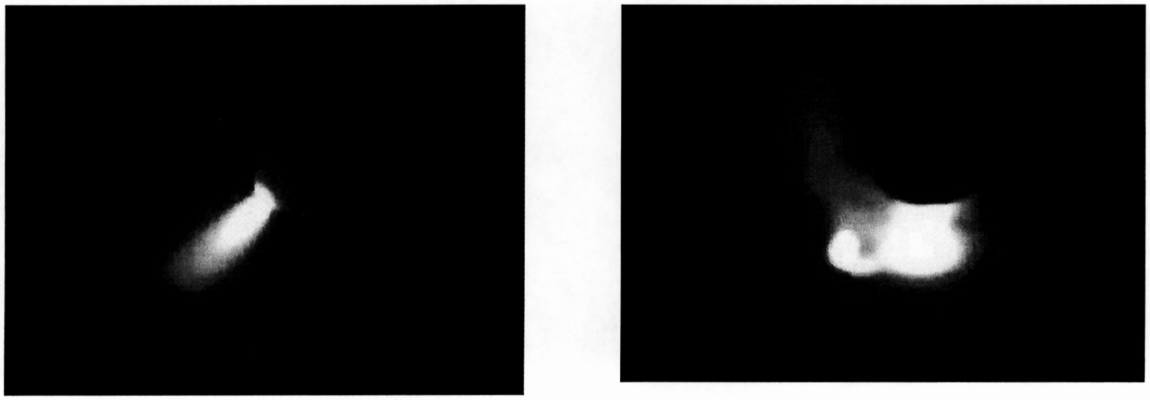

(n) Voltage=81 V, Exposure=8

(q) Voltage=45 V, Exposure=8

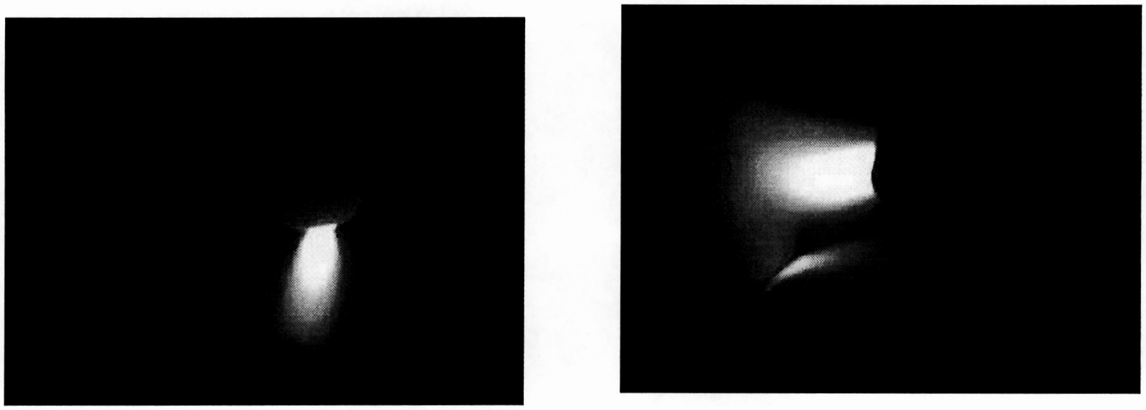

(o) Voltage=41 V, Exposure=8

(r) Voltage=61 V, Exposure=9

Figure 6-13: Arc pictures randomly taken for the unstable arc operation of EXP-84. (continued)

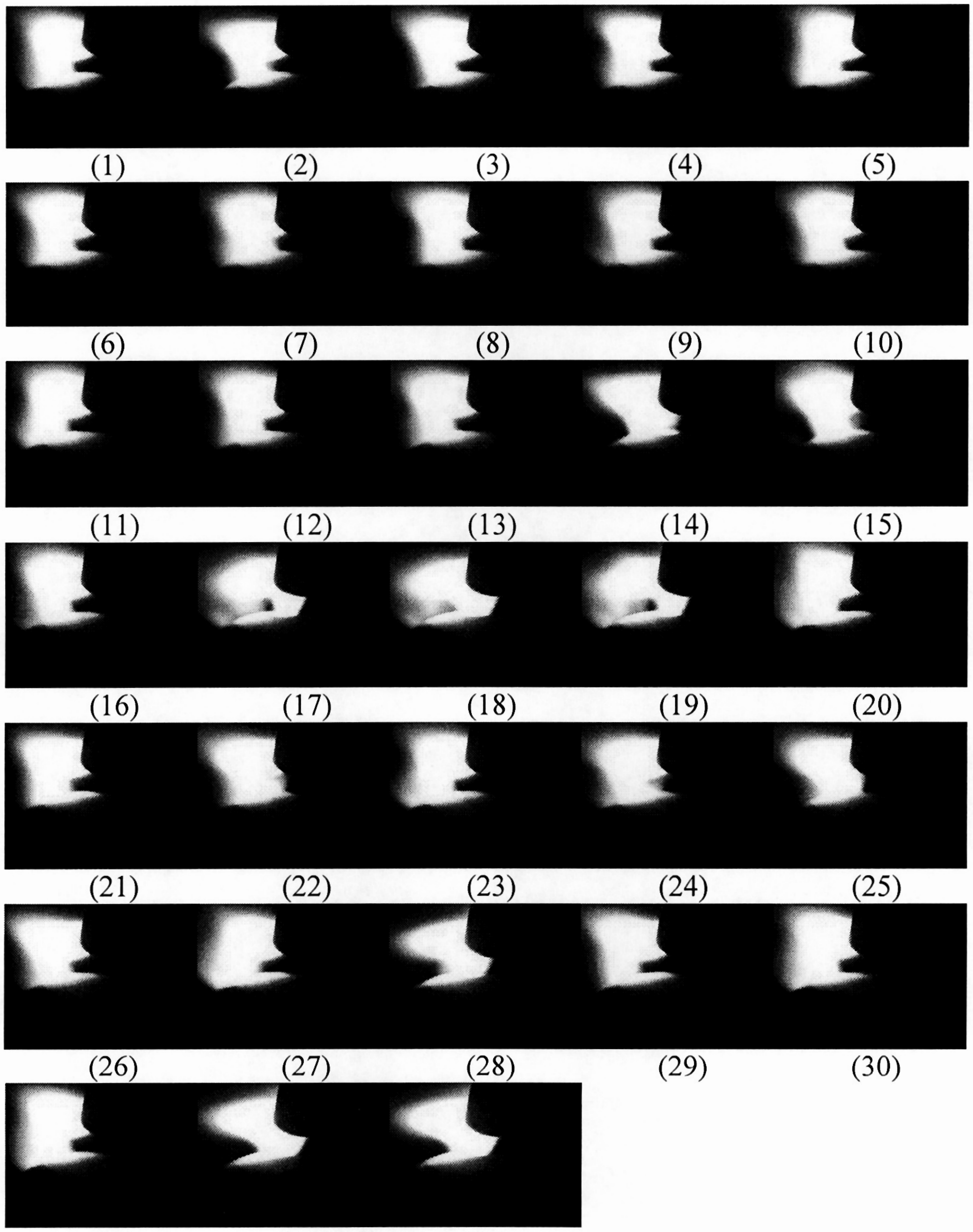

(1) (2) (3) (4) (5)

(6) (7) (8) (9) (10)

(11) (12) (13) (14) (15)

(16) (17) (18) (19) (20)

(21) (22) (23) (24) (25)

(26) (27) (28) (29) (30)

(31) (32) (33)

Figure 6-14: Arc pictures taken within 1 second at 48 minutes 55 seconds of EXP-84.

conditions selected for the run of Figure 6-16 were a current of 300 A, an argon gas flow rate of 0 slpm, and an initial interelectrode gap of 3.0 cm. The total voltage pattern of this run is presented in Figure 6-15. The experiment ran for 30 minutes and the arc was stable for the whole run. For 0 slpm the arc of cathode I changed from the stable to the unstable region and showed the great voltage fluctuation; however, for cathode II the arc was always stable and the voltage fluctuated little even after the arc stretched. Figure 6-15 presents the stretched arc voltage pattern of cathode II. At about 6 minutes the voltage started to increase corresponding to the stretching of the arc. The arc had a slow and uniform motion all over the cathode tip. The voltage was fairly constant fluctuating only by 2~3 volts, with a mean value of about 43 V.

Another total voltage pattern and arc pictures using cathode II are presented in Figures 6-17 and 6-18. This run lasted for 30 minutes at 300 A for an argon gas flow rate of 4.5 slpm and an initial interelectrode gap of 3.0 cm. The difference of total voltage patterns between EXP-81 and EXP-82 is that in the total voltage pattern of EXP-82, there was no voltage increase, as was observed after about 6 minutes in EXP-81. The increase of the argon gas flow rate might make the arc region more electrically conductive between the electrodes by washing out the vaporized graphite particles and thus the arc length change was less. That was also observed in other experiments at 10 and 15 slpm.

An incandescence at the tips of cathode I and II resulting from arc heating could be observed through the chamber window. Also some arc pictures show a color difference between two cathodes. For cathode II, the red zone at the tip was both longer and

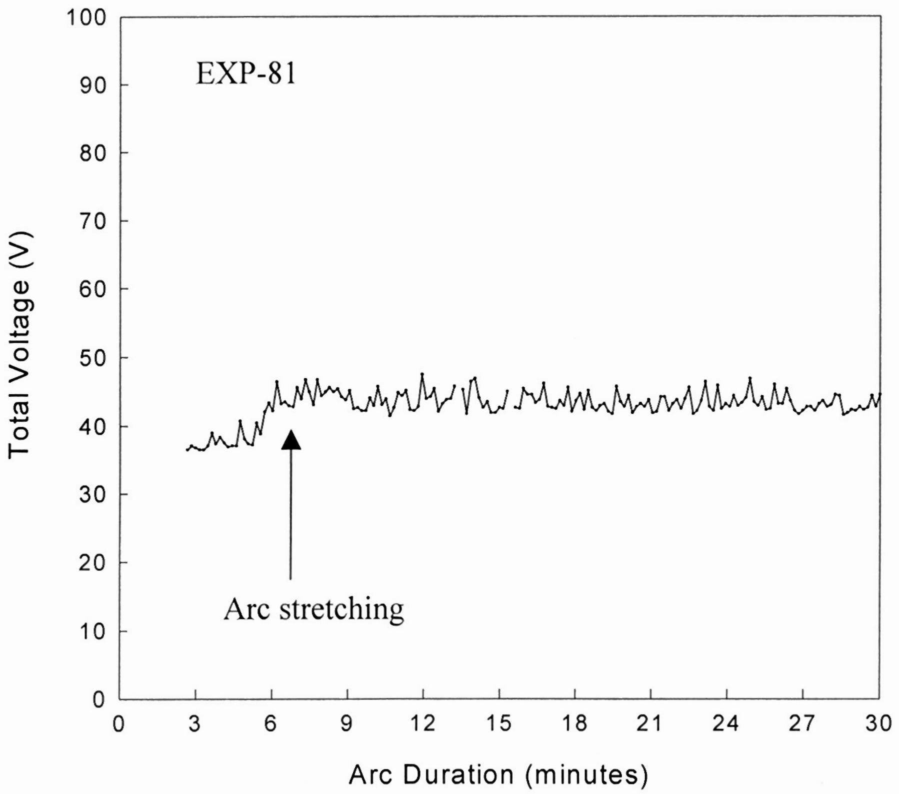

Figure 6-15: Total voltage pattern of a stable arc using cathode II recorded for an initial interelectrode gap of 3.0 cm, an argon gas flow rate of 0 slpm, and an arc current of 300 A.

(a) Voltage=41 V, Exposure=13

(b) Voltage=41 V, Exposure=11

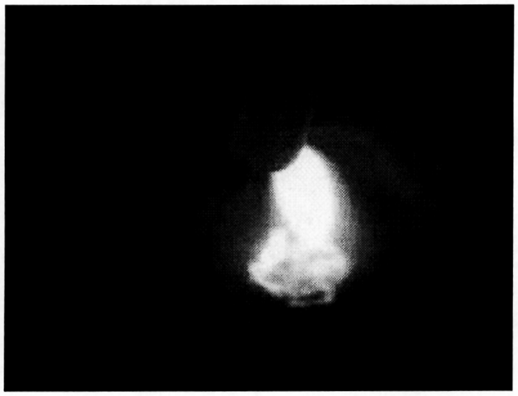

(c) Voltage=41 V, Exposure=10

(d) Voltage=42 V, Exposure=9

(e) Voltage=43 V, Exposure=8

Figure 6-16: Arc pictures randomly taken using cathode II (EXP-81).

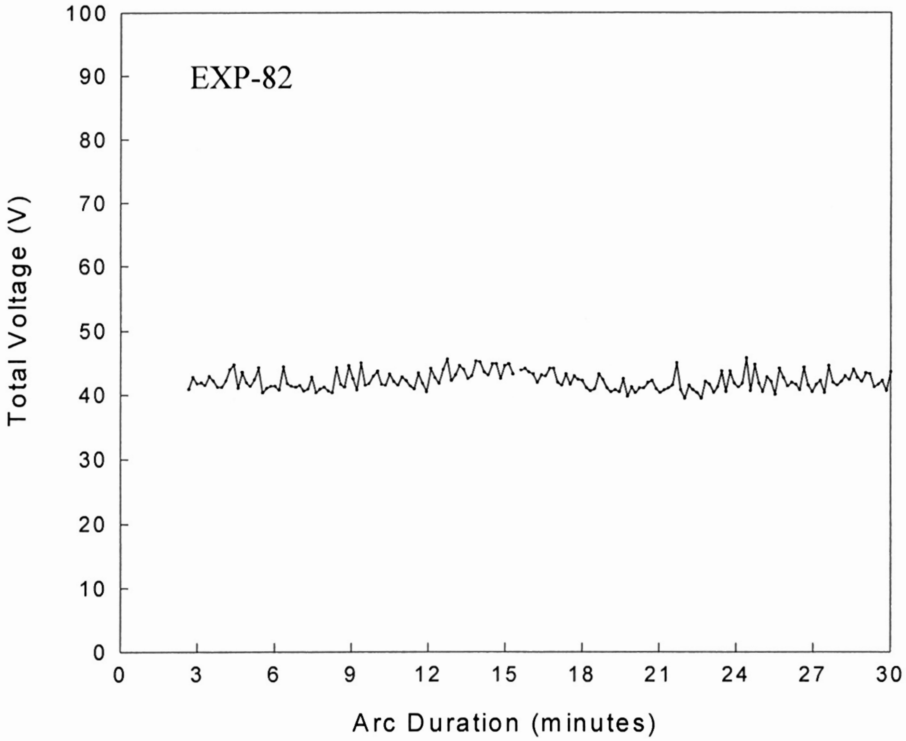

Figure 6-17: Total voltage pattern of a stable arc using cathode II recorded for an initial interelectrode gap of 3.0 cm, an argon gas flow rate of 4.5 slpm, and an arc current of 300 A.

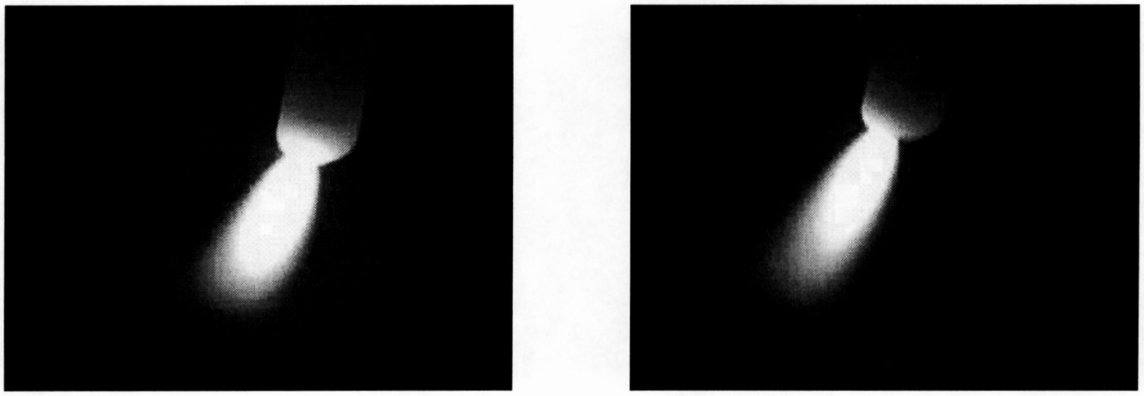

(a) Voltage=41 V, Exposure=13

(d) Voltage=41 V, Exposure=11

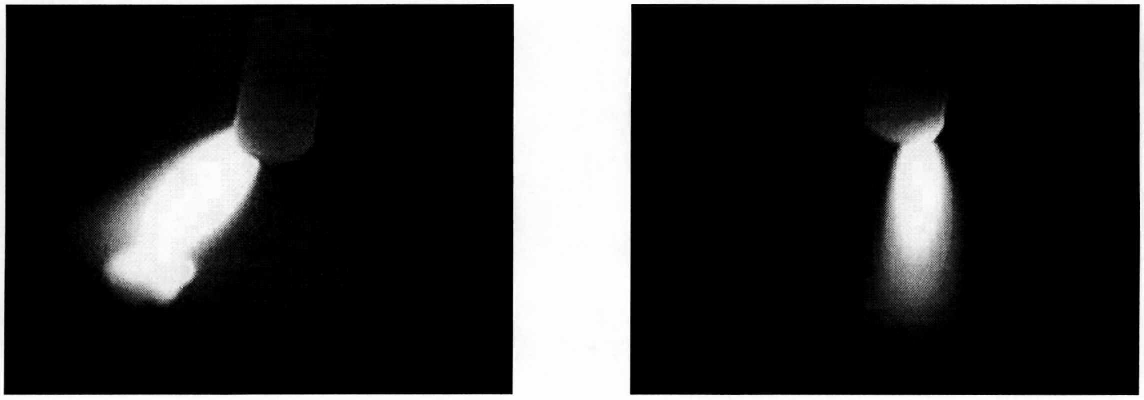

(b) Voltage=41 V, Exposure=13

(e) Voltage=41 V, Exposure=10

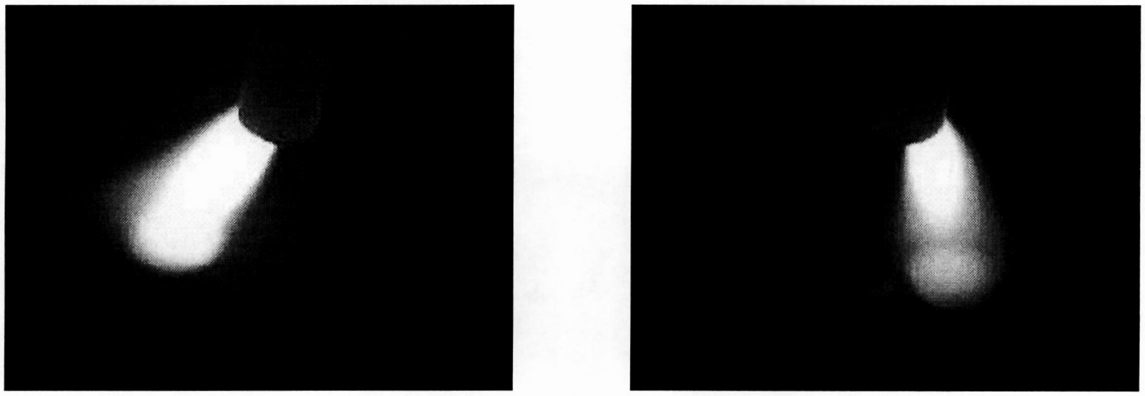

(c) Voltage=41 V, Exposure=12

(f) Voltage=41 V, Exposure=9

Figure 6-18: Arc pictures randomly taken using cathode II (EXP-82).

brighter; it was believed that this was due to less conduction heat loss through the cathode due to the smaller outer diameter as discussed earlier.

6.2. THE ARC STABILITY OF THE HOLLOW GRAPHITE CATHODE

Instability is indicated by electrical and acoustic noise as well as rapid motion of the arc on the cathode surface. Since plasma reactors are often closed and neither the acoustic noise nor the arc root motion is evident, it is better to rely on electrical noise, i.e. voltage fluctuations as an indicator of stability. In principle, either the standard deviation of the total voltage (ΔV) or the ratio of the standard deviation of the total voltage to the total voltage (ΔV/V) could be used. The data for both parameters are examined below and it was concluded that in the present work ΔV is the better indicator. An absolute value of ΔV > 3 V seems to separate the operation of the arcs examined here from the stable and unstable regimes consistent with the observations of acoustic noise, voltage fluctuations, and arc movement.

6.2.1. The Arc Stability Indicator

Firstly, ΔV and ΔV/V are plotted as a function of the initial interelectrode gap and the argon gas flow rate for all the conditions and cathodes examined as shown in figures from 6-20 to 6-27. Secondly, to select the arc stability indicator, a comparison between ΔV and ΔV/V is made as follows. In the figures separation of the total voltage into the stable and the unstable part is performed to see trends of the arc stability indicators for each operation. In case of the ΔV, the borderline between the stable and the unstable part is clearly distinguished. The stable region is less than the ΔV of 3 V; the unstable region is greater than the ΔV of 3 V. This borderline of 3 V, of course, might change in a different transferred-arc system; however, it was useful in this work for the classification of the stable and the unstable operation. Meanwhile, for the ΔV/V, the borderline is not clear. Normally, operation is stable for the ΔV/V less than 0.10. However, in some cases, as shown in Figures 6-21, 6-23, 6-25, and 6-27, the stable and the unstable operation co-existed between the ΔV/V is of 0.10 and 0.15. This was caused by two factors. The first factor was low frequency, low amplitude fluctuations of the voltage in some stable arcs (see Figure 6-19). For the stable part at 0.5 cm, 4.5 slpm, and 150 A, this caused increase of the ΔV and the ΔV/V. These fluctuations were completely different from the large voltage fluctuations in the unstable operation in that there were not high amplitude random fluctuations. The second factor was that in the unstable part, V as well as ΔV increased simultaneously, thus affecting the ΔV/V. This could be seen in the runs for 1.5 cm, 4.5 slpm, and 120 minutes at 150 A (EXP-10) and for 1.5 cm, 0 slpm, and 120 minutes at 150 A (EXP-30). The ΔV and the ΔV/V of these runs are presented in Table 6-1. Between these two runs, the only different operating condition was the argon gas flow rate. In this work the ΔV increased as the argon gas flow rate decreased. Therefore, increase of the ΔV/V was also expected for EXP-30 due to the decrease of the argon gas flow rate. However, the ΔV/V decreased even though the argon gas flow rate was 0 slpm. It seemed that because V as well as ΔV increased together in the unstable part, the higher V lowered the ΔV/V.

From the comparison, the ΔV was selected as the arc stability indicator in this study. It does not mean that the ΔV is an absolutely better indicator. The comparison just indicates that the ΔV is more proper to analyze the results of the arc stability in this study. In the following part, therefore, basically the ΔV is used as the arc stability indicator for discussions of the arc stability.

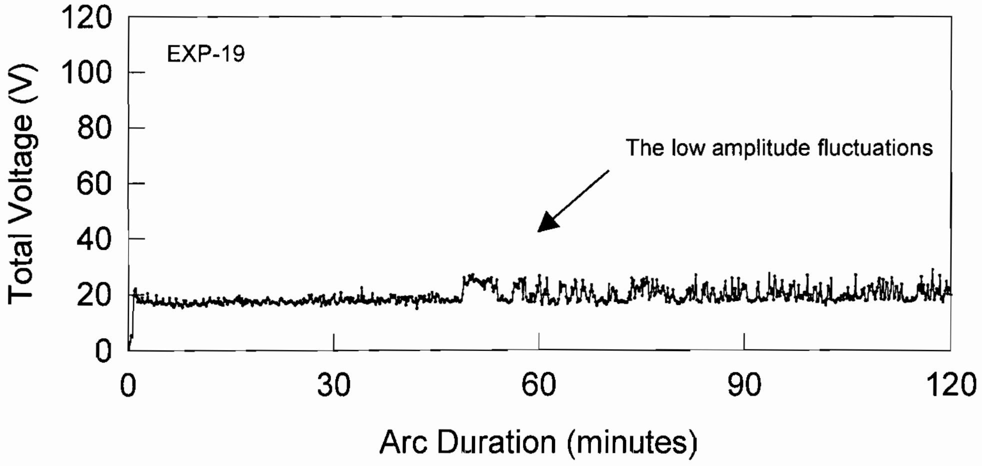

Figure 6-19: Low amplitude fluctuations of the arc voltage in a stable arc. This run used cathode I for an initial interelectrode gap of 0.5 cm, an argon gas flow rate of 4.5 slpm, and an arc current of 150 A.

Table 6-1: A comparison between the ΔV and the ΔV/V

EXP-NO.	The stable operation			The unstable operation		
	ΔV	V	ΔV/V	ΔV	V	ΔV/V
EXP-10[1)]	1.27	24.81	0.05	5.76	34.35	0.17
EXP-30[2)]	1.28	23.58	0.05	7.69	47.78	0.16

1) Operating conditions: 1.5 cm, 4.5 slpm, 120 minutes, and 150 A.

2) Operating conditions: 1.5 cm, 0 slpm, 120 minutes, and 150 A.

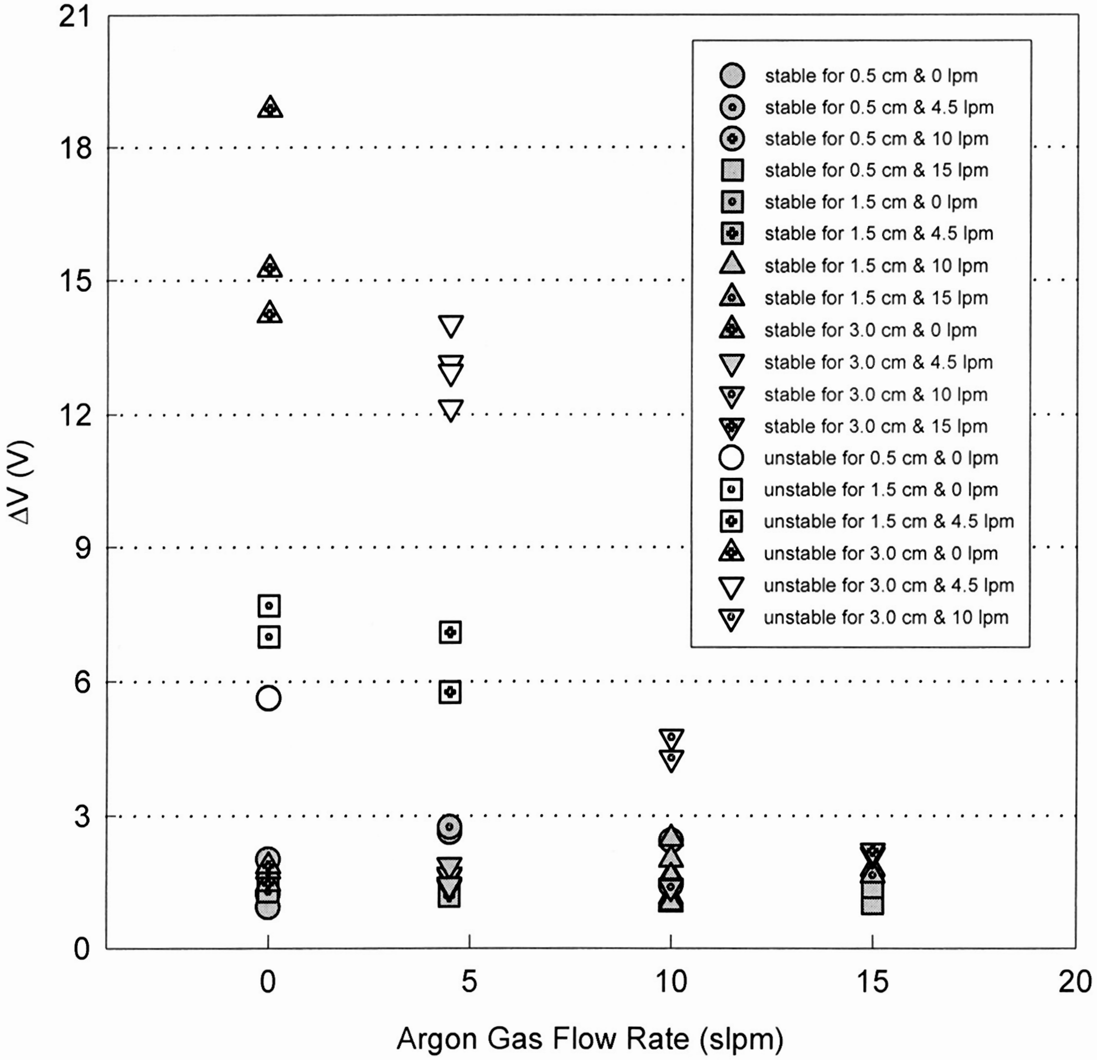

Figure 6-20: ΔV for the stable and the unstable operation separated as a function of the argon gas flow rate using cathode I at 150 A.

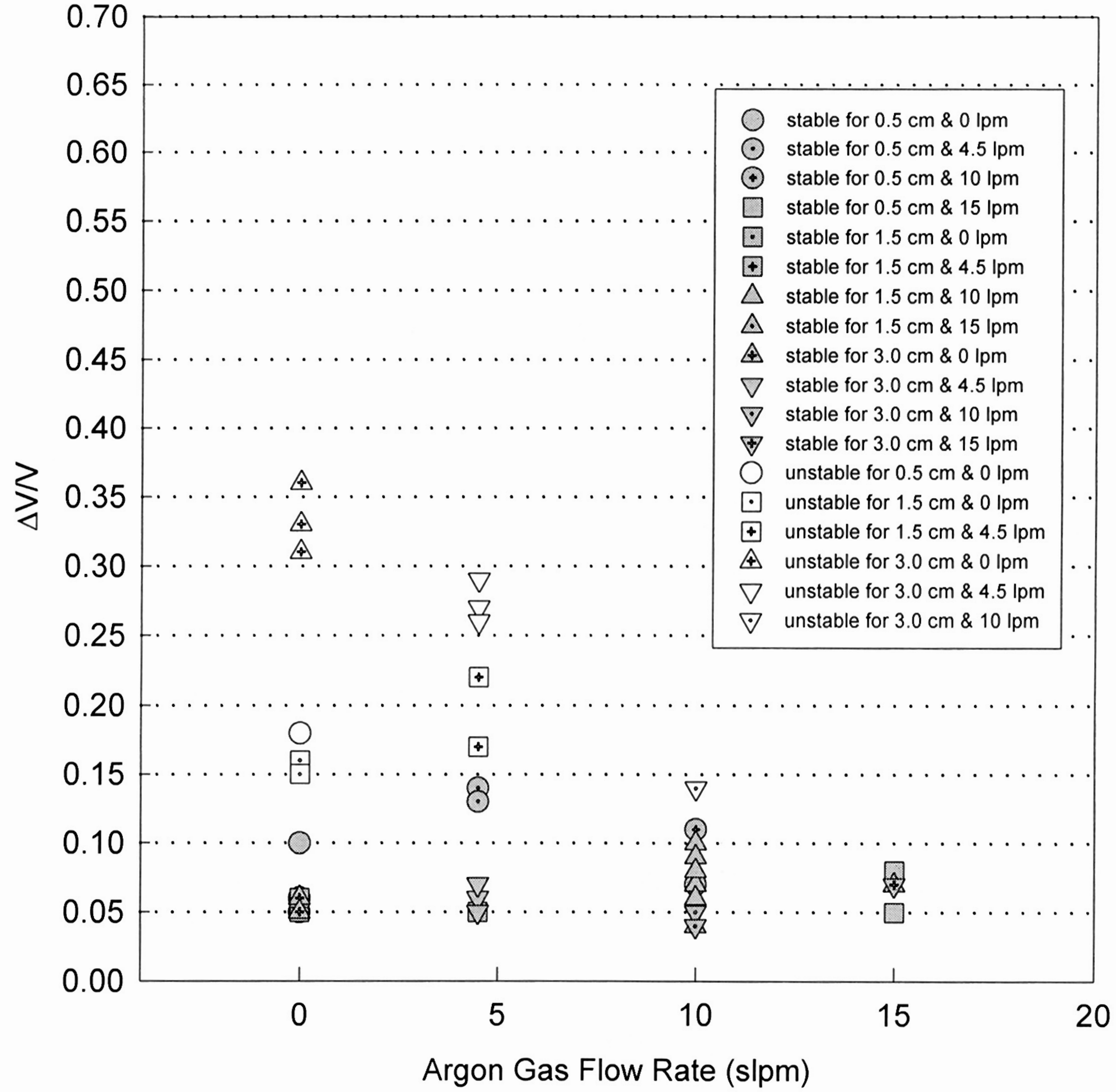

Figure 6-21: ΔV/V for the stable and the unstable operation separated as a function of the argon gas flow rate using cathode I at 150 A.

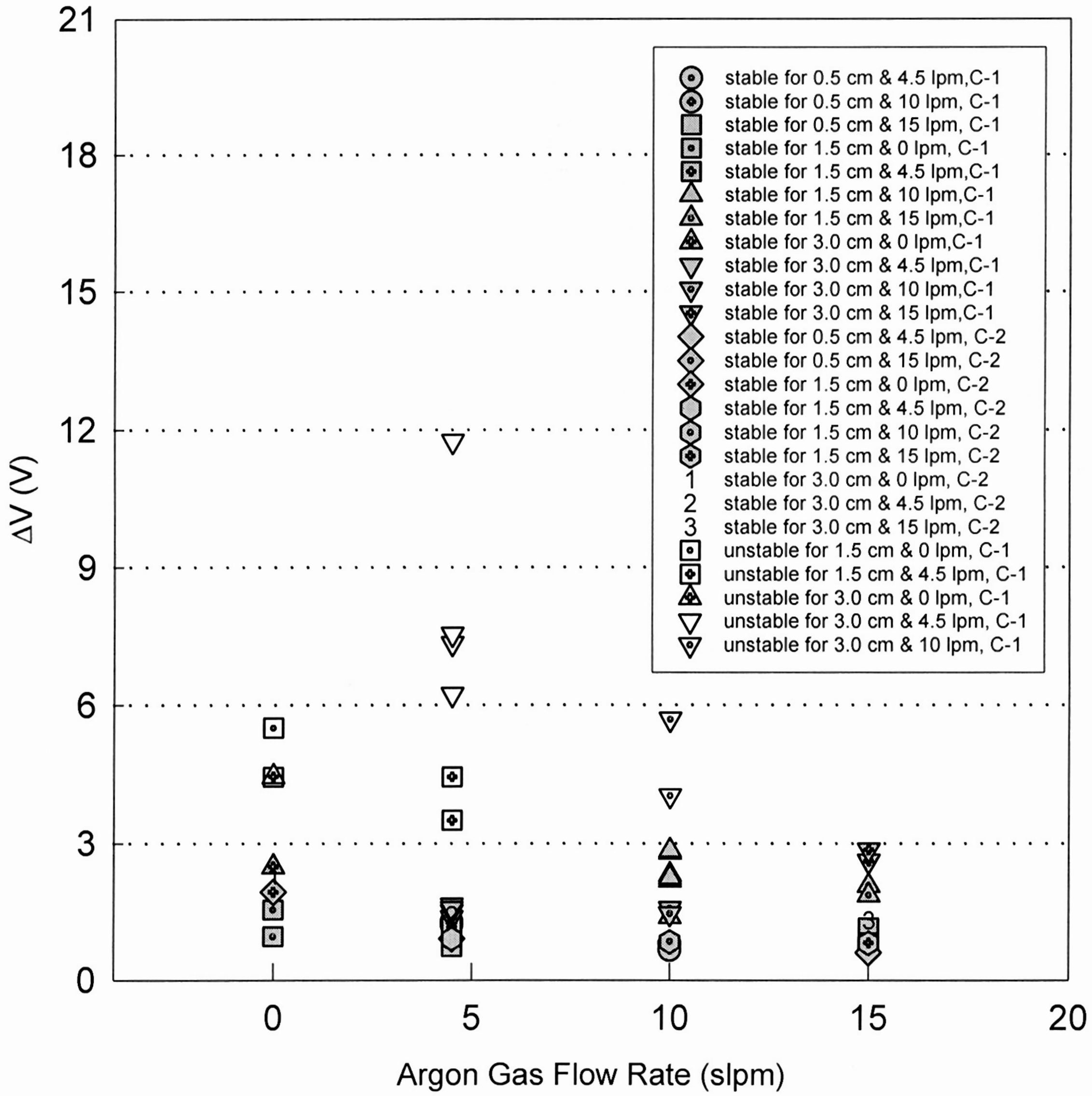

Figure 6-22: ΔV for the stable and the unstable operation separated as a function of the argon gas flow rate at 300 A. C-1 stands for cathode I; C-2 is for cathode II.

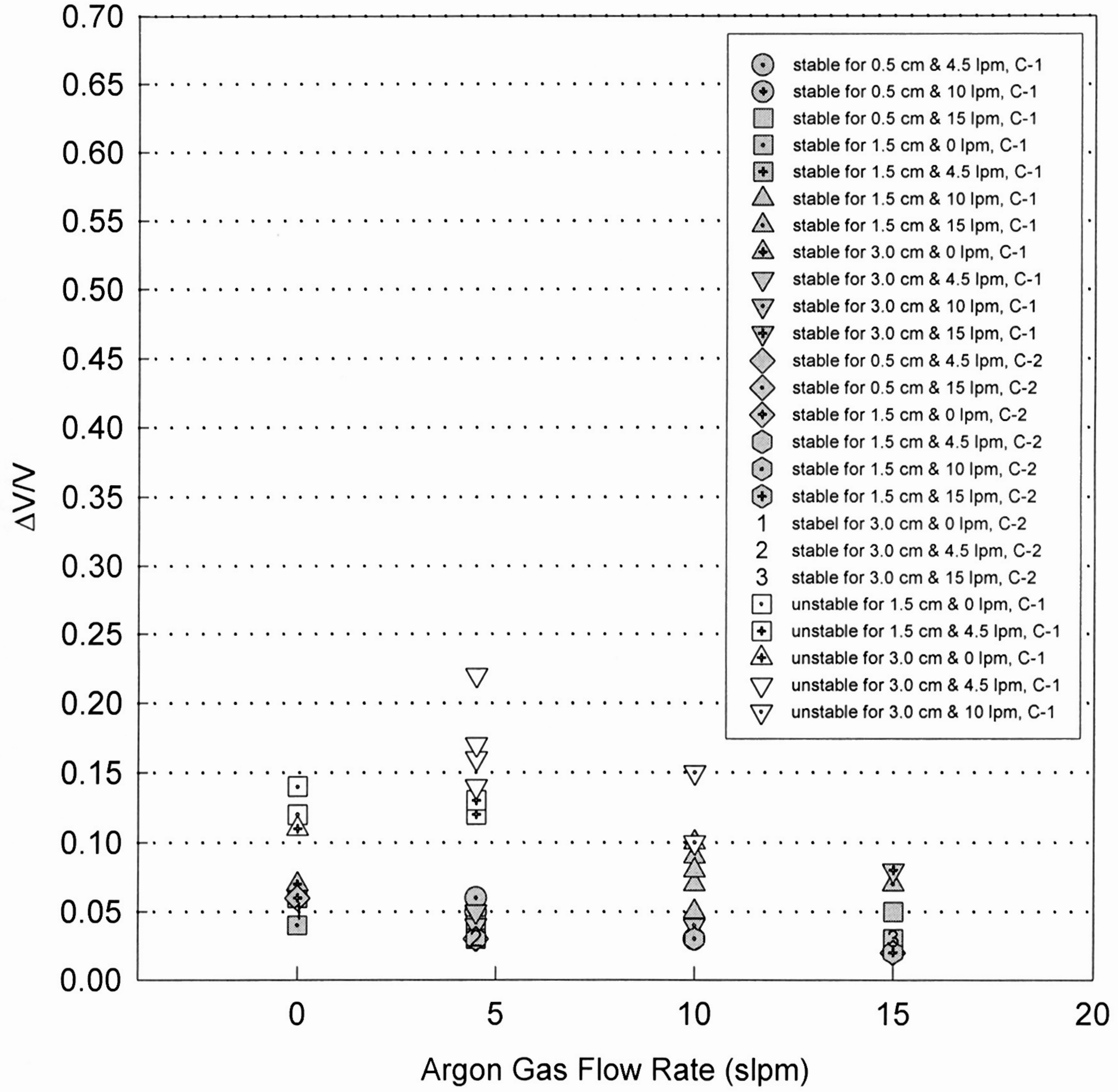

Figure 6-23: ΔV/V for the stable and the unstable operation separated as a function of the argon gas flow rate at 300 A. C-1 stands for cathode I; C-2 is for cathode II.

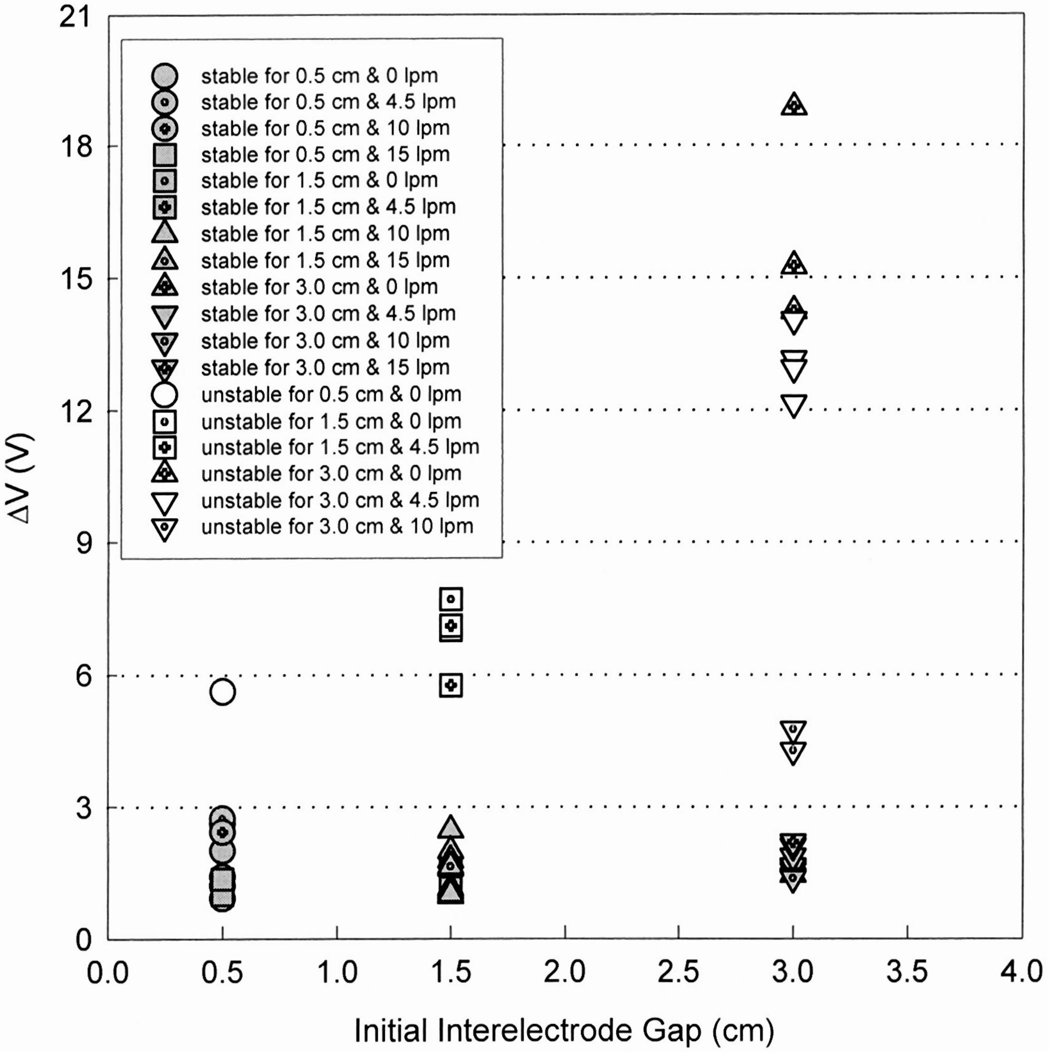

Figure 6-24: ΔV for the stable and unstable operation separated as a function of the initial interelectrode gap using cathode I at 150 A.

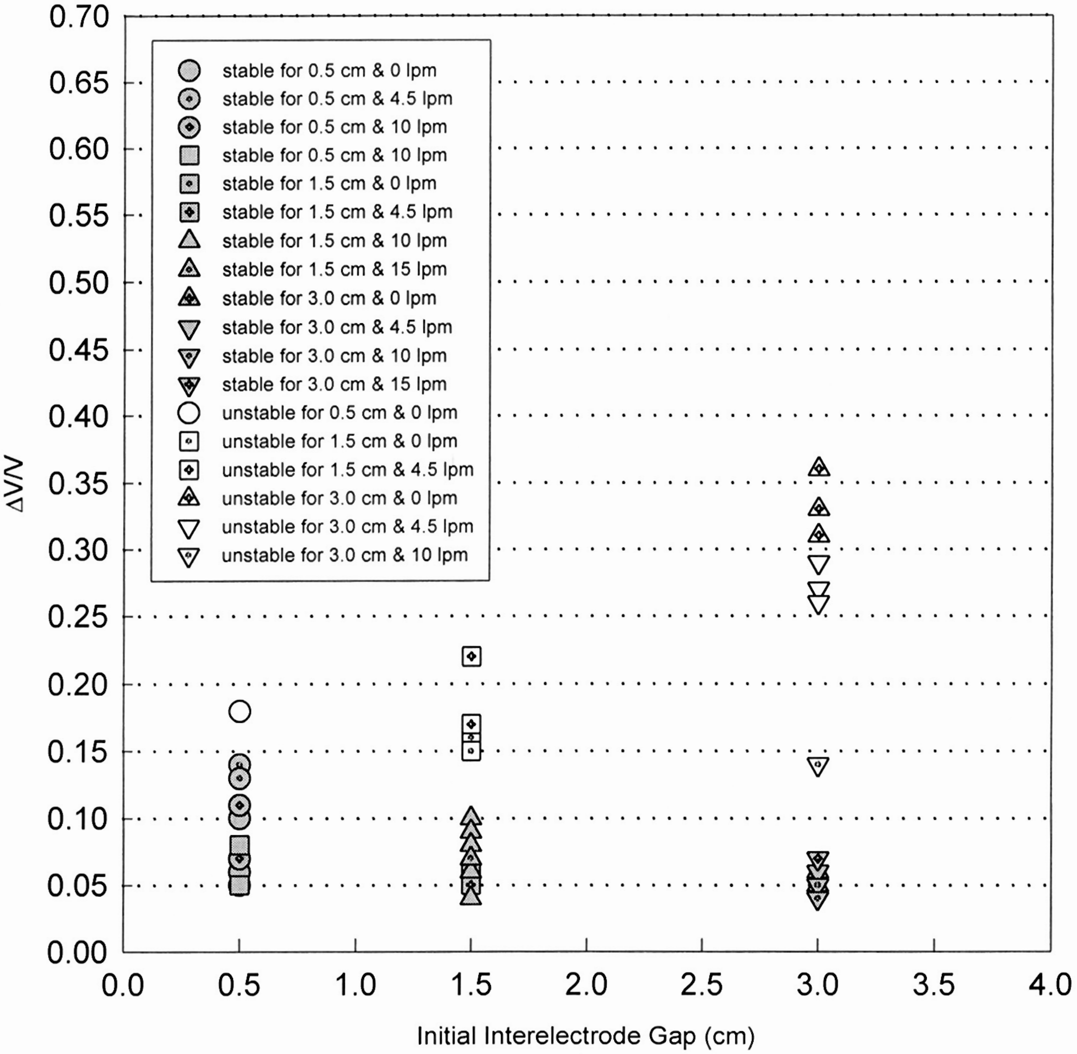

Figure 6-25: ΔV/V for the stable and unstable operation separated as a function of the initial interelectrode gap using cathode I at 150 A.

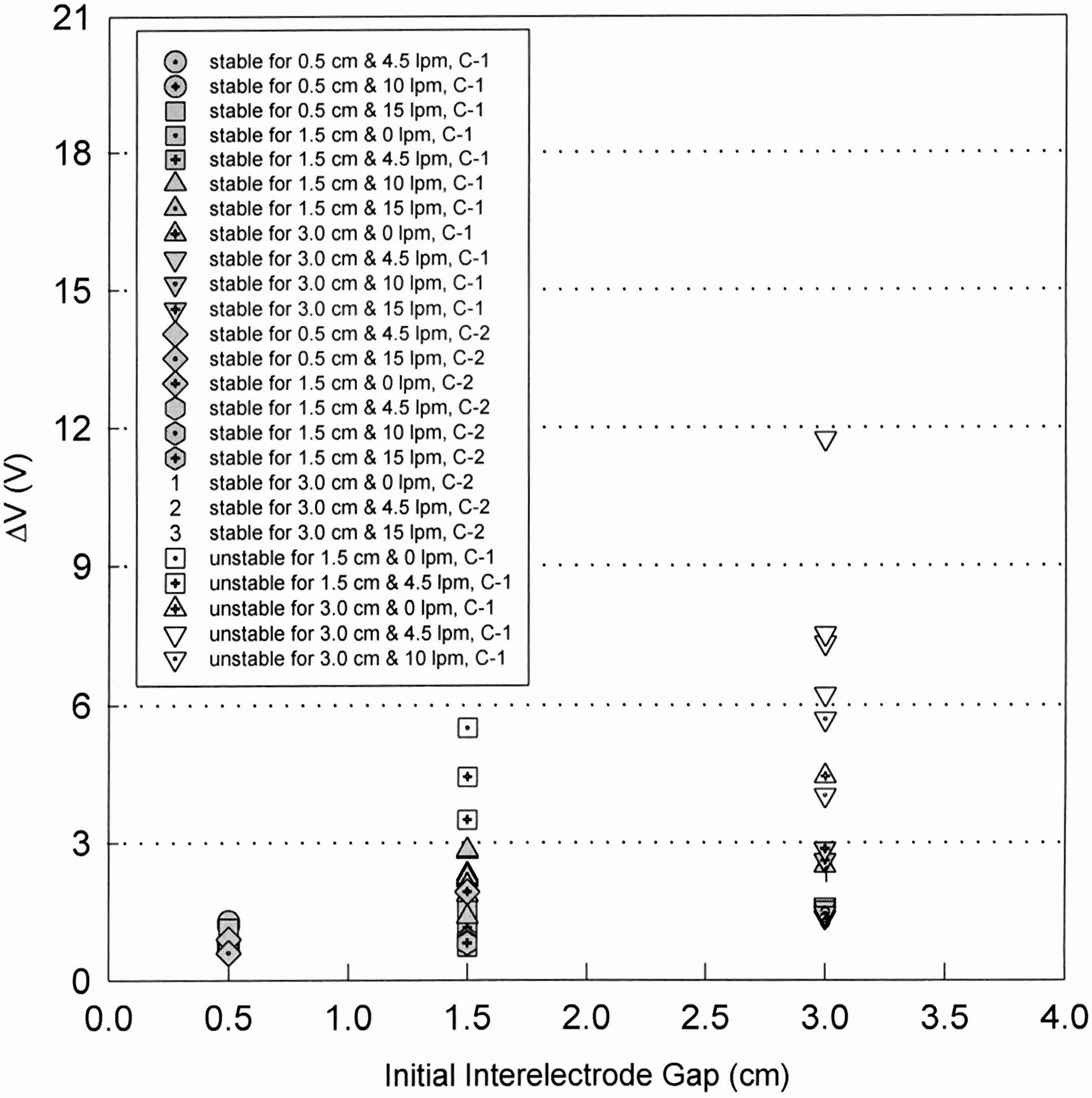

Figure 6-26: ΔV for the stable and the unstable operation separated as a function of the initial interelectrode gap at 300 A. C-1 stands for cathode I; C-2 is for cathode II.

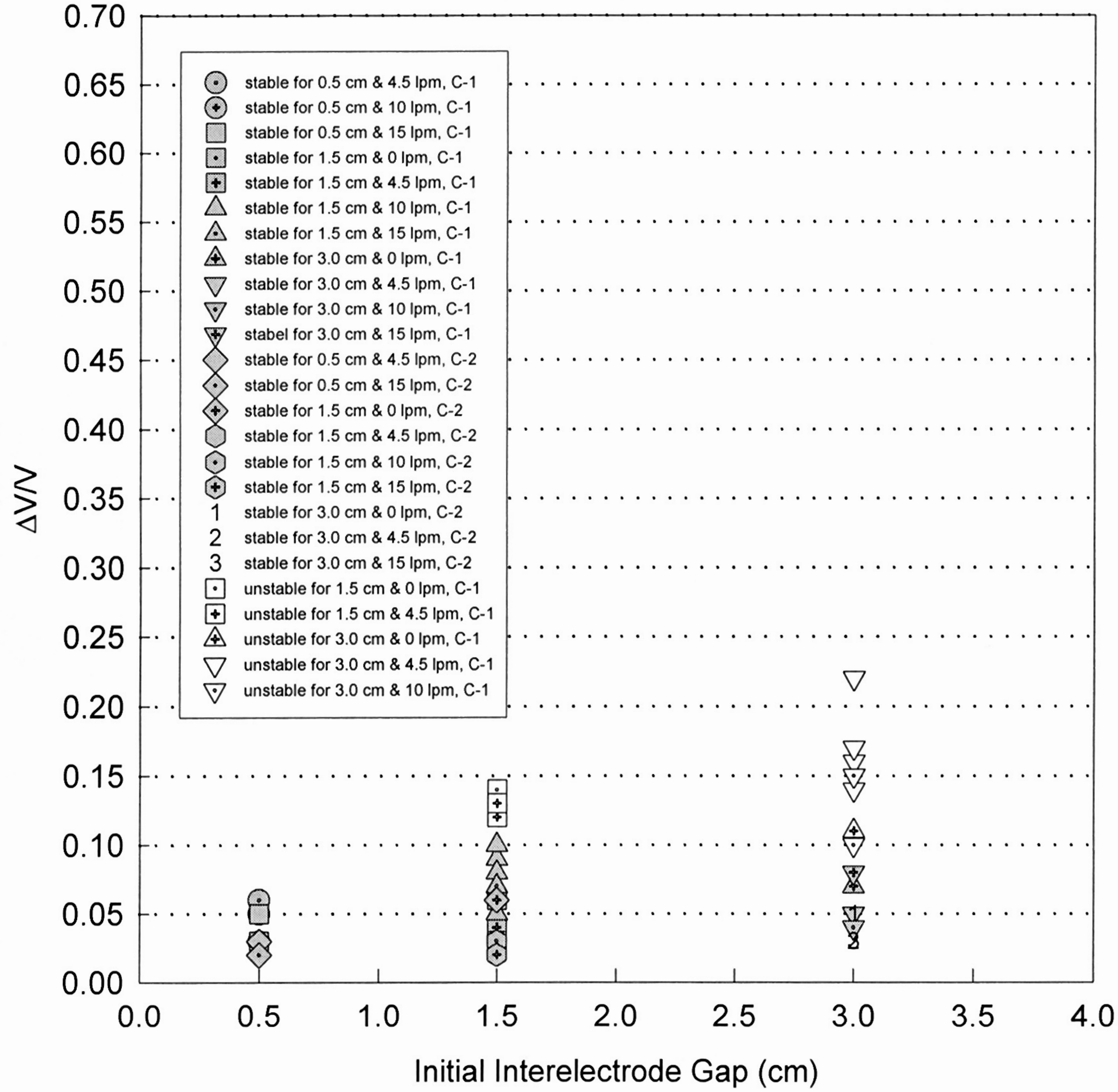

Figure 6-27: ΔV/V for the stable and the unstable operation separated as a function of the initial interelectrode gap at 300 A. C-1 stands for cathode I; C-2 is for cathode II.

In the following section, to discuss the arc stability as a function of the argon gas flow rate and the initial interelectrode gap, previous Figures 6-20, 6-22, 6-24, and 6-26 are used. Before the discussions, effect of the cathode tip geometry on the arc stability and overview of the arc stability are presented.

6.2.2. Effect of The Cathode Tip Geometry on The Arc Stability

Discussion of this effect is first given because it was performed using a used cathode, i.e. a cathode without the pointed tip. As briefly mentioned earlier, before the cathode tip eroded the arc was always stable. It seems that before the tip eroded, the cathode tip temperature might be higher because the cross-sectional area of the tip is smaller than that of the normal cathode body. This might increase the arc root temperature. In addition, the self-magnetic force produced by the tip might affect the arc stability. According to Montgomery et al.' (1969) study, carbon arcs for an arc current of 400 ~ 2,000 A at atmospheric pressure were stable before a sharp edge on the cathode eroded. This sharp edge might correspond to the tip of the cathode used in this study. They used various graphite rod cathodes with different edge angles on the cathode and reported that before the edge eroded the arcs were stable because of the self-magnetic force.

A run using an used cathode was performed to examine this effect by recording the voltage. Figure 6-28 shows the total voltage pattern of the used cathode. The run was started with an argon gas flow rate of 4.5 slpm and an initial interelectrode gap of 3.0 cm at 150 A. As can be seen in the figure, the arc was unstable as soon as the arc was ignited.

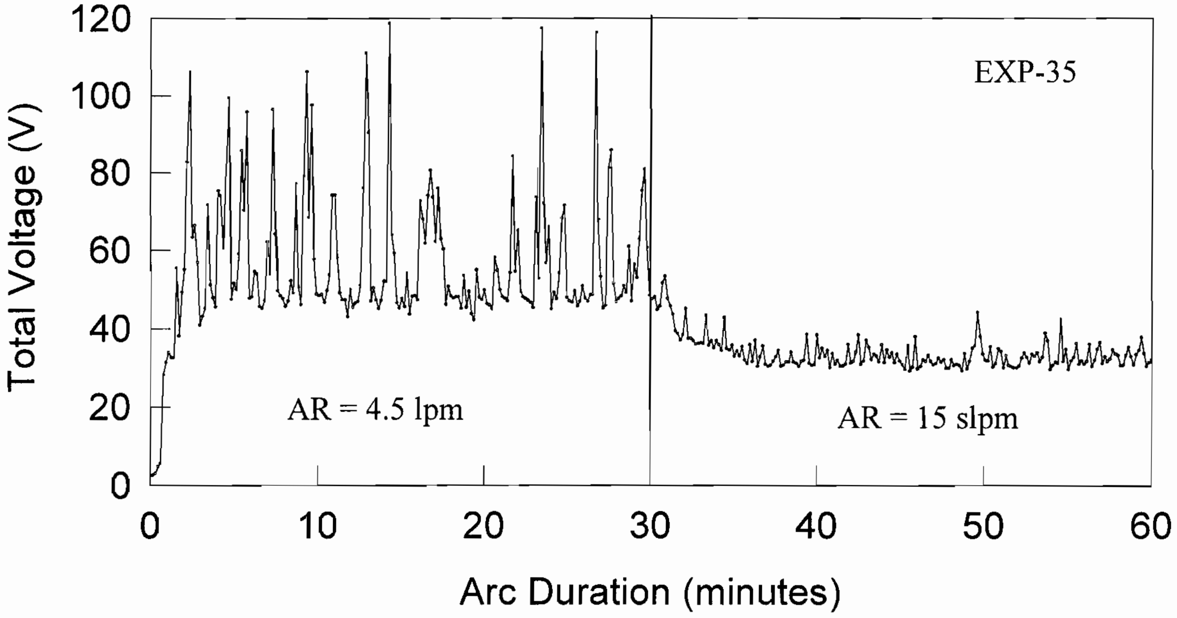

Figure 6-28: Total voltage pattern of the used cathode I for an initial interelectrode gap of 3.0 cm at 150 A.

Because the used cathode had no sharp tip and the argon gas flow rate was lower, the electron emission of the cathode was believed to be in the thermofield emission regime, thus providing the great voltage fluctuations. At 30 minutes the argon gas flow rate was increased to 15 slpm and the voltage fluctuations began to disappear as soon as the argon flow rate was increased. It was believed that the higher argon flow rate increased the arc root temperature as well as the electrical conductivity of the arc, thus making the arc stable. Details of the effect of the argon gas flow rate on the arc stability are presented in the section of 6.2.4.

6.2.3. Overview of The Arc Stability

An overview of the arc stability in this study is presented in Figures 6-29 and 6-30 for 150 A and 300 A runs, respectively. For stable arc runs, given by the open symbols, the ΔVs taken over an entire run are used because the ΔVs for stable arc operation were always less than 3 V and did not affect the behavior of the ΔVs during a complete run. Meanwhile, for unstable arc runs, given by the black symbols, the ΔVs captured during unstable arc operation are used. These ΔVs are included in Appendix 4. As shown in the figures, the arcs shift from the unstable region to the stable region as the argon gas flow rate increases and as the initial interelectrode gap decreases.

6.2.4. Effect of Argon Gas Flow Rate on The Arc Stability

Figures 6-20 and 6-22 show the ΔV as a function of the argon gas flow rate for the 150 and 300 A experiments. In the stable operation, the ΔV was almost constant under 3 V, but in the unstable operation, as the argon flow rate was increased, the ΔV generally was

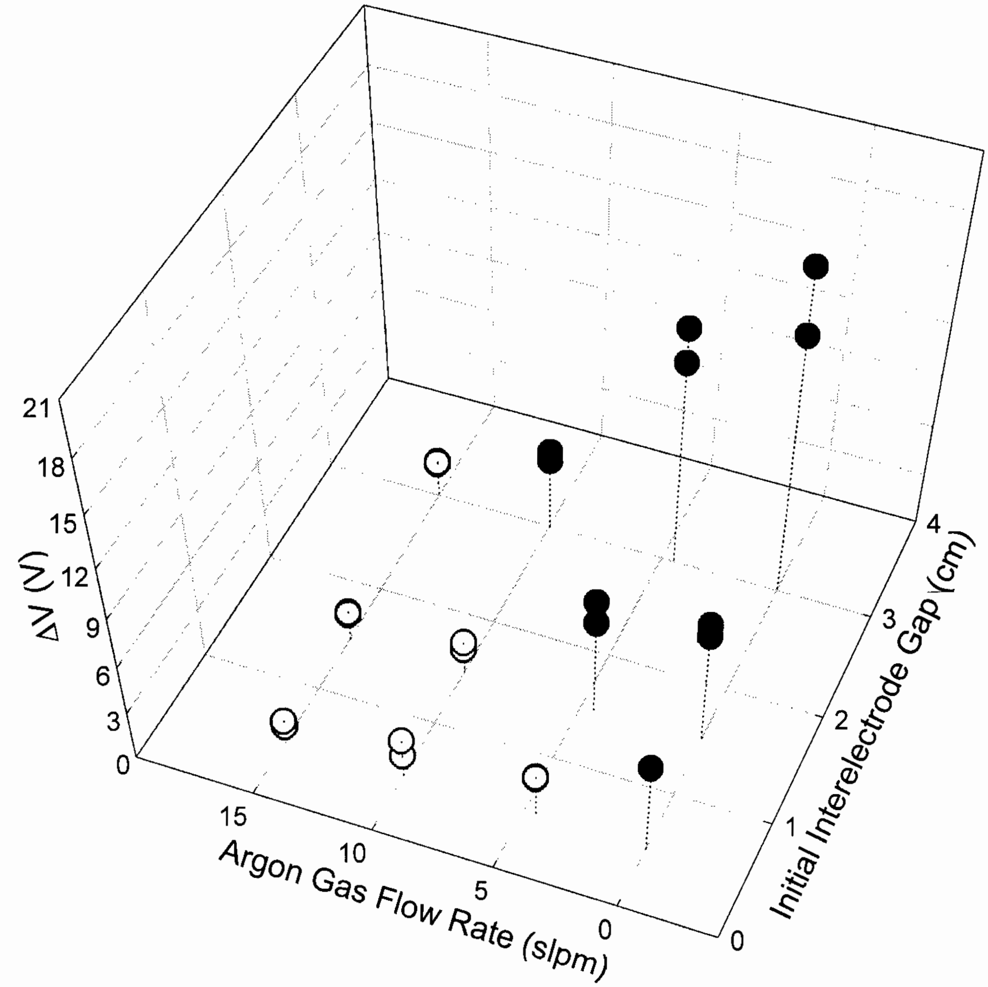

Figure 6-29: 3-D overview of the arc stability for an arc duration of 120 minutes and an arc current of 150 A. The white circles are for the stable arcs and the black circles are for the unstable arcs.

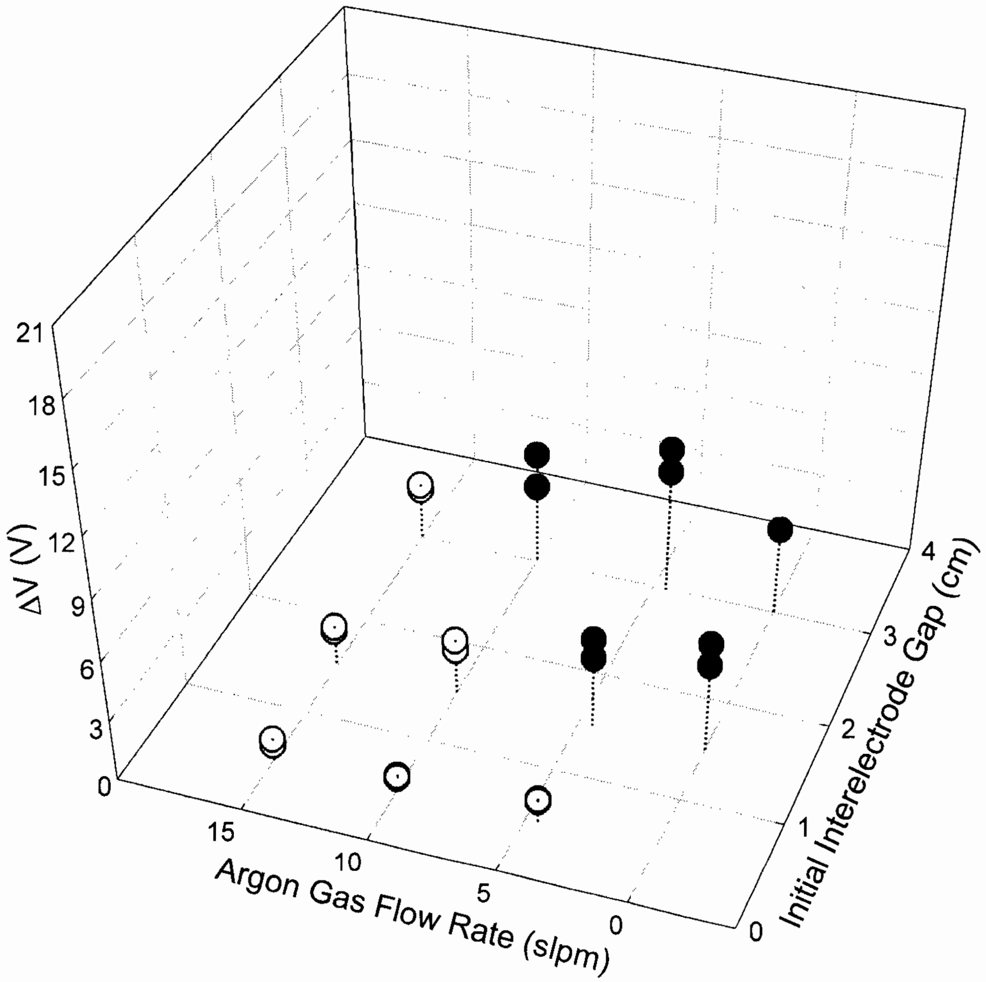

Figure 6-30: 3-D overview of the arc stability for an arc duration of 30 minutes and an arc current of 300 A. The white circles are for the stable arcs and the black circles are for the unstable arcs.

decreased. This meant that the arc was more stable for higher argon gas flow rate runs at the same initial interelectrode gap. However, a different trend appeared in unstable operation at 3.0 cm, 0 slpm, and 300 A. The ΔV of this run was lower than that at 1.5 cm, 0 slpm, and 300 A (see Figure 6-22) even though higher ΔV was expected at 3.0 cm, 0 slpm, and 300 A because of the higher interelectrode gap. This was due to abnormal total voltage patterns (see Figure 6-31); unlike the large voltage fluctuations in the typical unstable operation, the total voltage of this run increased gradually. This kind of the total voltage pattern was difficult to classify into stable or unstable operation, but it was categorized as an unstable arc because the ΔV of this run was greater than 3 V. It was believed that the arc was approaching instability at a time of about 27 minutes.

Figure 6-32 presents the ΔV of cathode II compared with that of cathode I. The ΔVs in this figure were taken over an entire run. For cathode I, the argon gas flow rate affected the arc stability. However, in the case of cathode II, the arc stability was independent of the operating conditions; the runs using cathode II were always stable. There were not the great voltage fluctuations, and the ΔV was always less than 3 V. The arcs of cathode II were stable even at 0 slpm. In this case the arc was stretched because of the presence of condensed carbon particles in the argon atmosphere. This stretching caused an increase of the arc length and small fluctuations of the total voltage; therefore, the ΔV at 0 slpm were little higher than the other runs, which the argon gas was injected.

For cathode I, the arc was more stable at higher argon flow rate operation. It has been understood that increasing the argon gas flow rate has three important effects on the arc

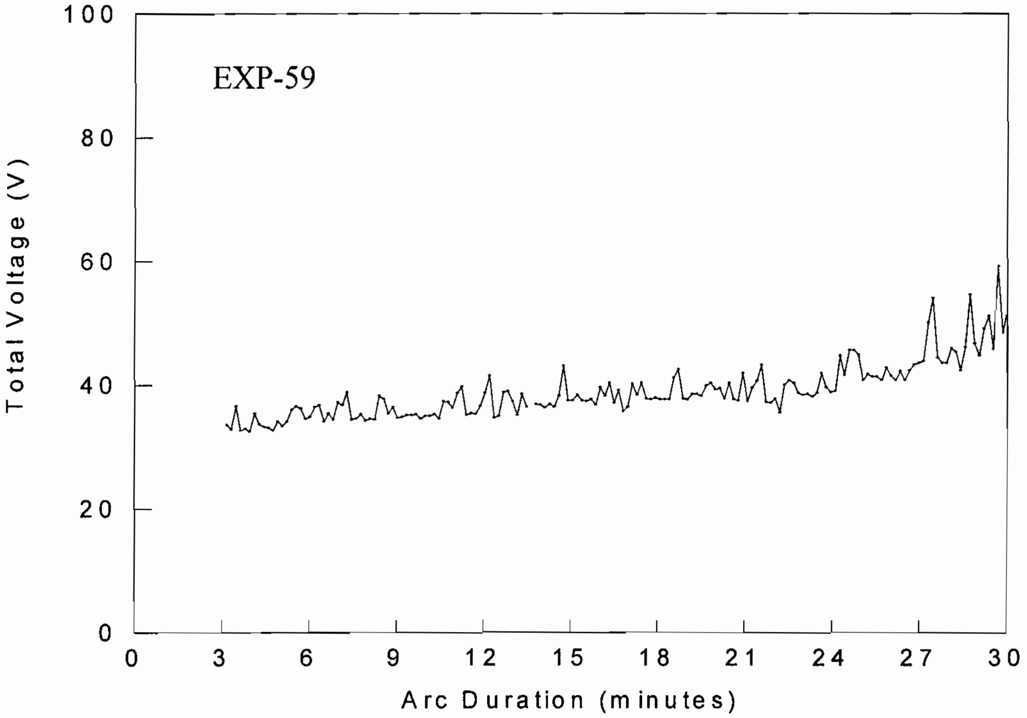

Figure 6-31: Total voltage pattern using cathode I for an argon gas flow rate of 0 slpm, an initial interelectrode gap of 3.0 cm at 300A.

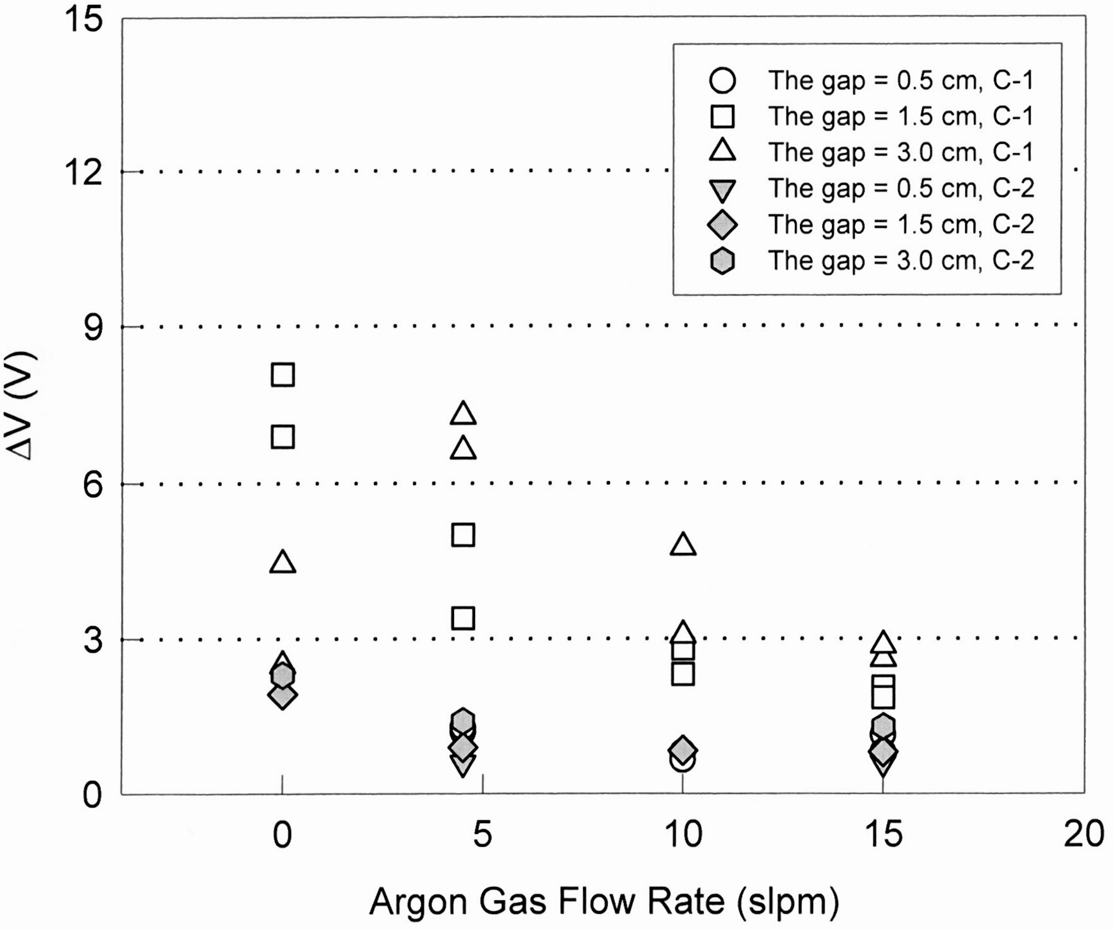

Figure 6-32: ΔV of cathode I and II as a function of the argon flow rate for a current of 300 A and an arc duration of 30 minutes. C-1 stands for cathode I; C-2 is for cathode II.

stability. First, it increases the electrical conductivity of the arc by washing out vaporized graphite or recondensed carbon particles near the arc. Second, it may also steepen the thermal gradient at the arc root by internal cooling of the electrode, thus giving a higher arc root temperature, which shifts the emission from the thermofield emission to the thermionic emission. Third, the increased gas flow rate may increase cooling on the periphery of the arc, which results in increasing ion-electron recombination on the outside and ionization phenomena inside the arc as stated by Pfender et al. (1987) and Roth (1995). This will also tend to increase the arc root temperature. In summary, it appears that higher argon gas flow rates might increase the arc root temperature, reduce electron emission by cathode spots, and eliminate the large voltage fluctuations. The disappearance of the large voltage fluctuations at higher argon gas flow rate is good evidence for the thermionic emission under this condition. Desaulniers-Soucy and Meunier (1995) studied the voltage fluctuations using a copper cathode, i.e. a cold cathode operated in the thermofield emission. They reported that the voltage fluctuations were caused by the arc length change and the cathode spot emission in the thermofield emission. In the present study, the voltage pattern of the stretched arc of cathode II showed that the voltage fluctuations due to the arc length change were relatively small. Therefore, it was thought that the voltage fluctuations in the unstable part were primarily due to the electron emission by the cathode spots in the thermofield emission regime.

In case of cathode II, the arcs were always stable. Since cathode II was designed to reduce the heat conduction loss through the bulk cathode body, it is logical that higher arc root temperature leads to the thermionic emission.

A higher argon gas flow rate also affected the cathode surface structure after a run as shown in Figure 6-33. A JOEL-840 scanning electron microscope (SEM) was used to see the surface structure. These SEM pictures present the cathode surface structure after treatment by stable arcs using cathode II at 300 A. Figure 6-33 (a) shows the surface structure after a run at 0 slpm, 3.0 cm, 30 minutes, and 300 A; Figure 6-33 (b) presents the surface structure after a run at 15 slpm, 3.0 cm, 30 minutes, and 300 A. The only different operating condition is the argon gas flow rate. It is clear that higher argon gas flow rate cooled the cathode surface. For 0 slpm the center of cathode II was strongly heat treated by the stable arc, and modification of the surface structure at the center could be seen clearly. This appears to be a coarsening of grain structure. However, for 15 slpm the shape of the center was conserved like that before the arc treatment because of the cooling by the argon gas.

6.2.5. Effect of Initial Interelectrode Gap on The Arc Stability

The initial interelectrode gap also affected the arc stability. Figures 6-24 and 6-26 show the effect of the initial interelectrode gap on the arc stability at 150 and 300 A. Generally, as the initial interelectrode gap decreased, the arc stability increased. However, the ΔV at 3.0 cm and 0 slpm, and 300 A was lower than that at 1.5 cm, 0 slpm, and 300 A (see Figure 6-26) due to the abnormal unstable voltage pattern, already introduced in Figure 6-31. It seemed that the reduced interelectrode gap might suppress the radial arc movement. At higher interelectrode gap, the arc could move further radially; this increase of the radial arc movement might contribute somewhat to the voltage fluctuations.

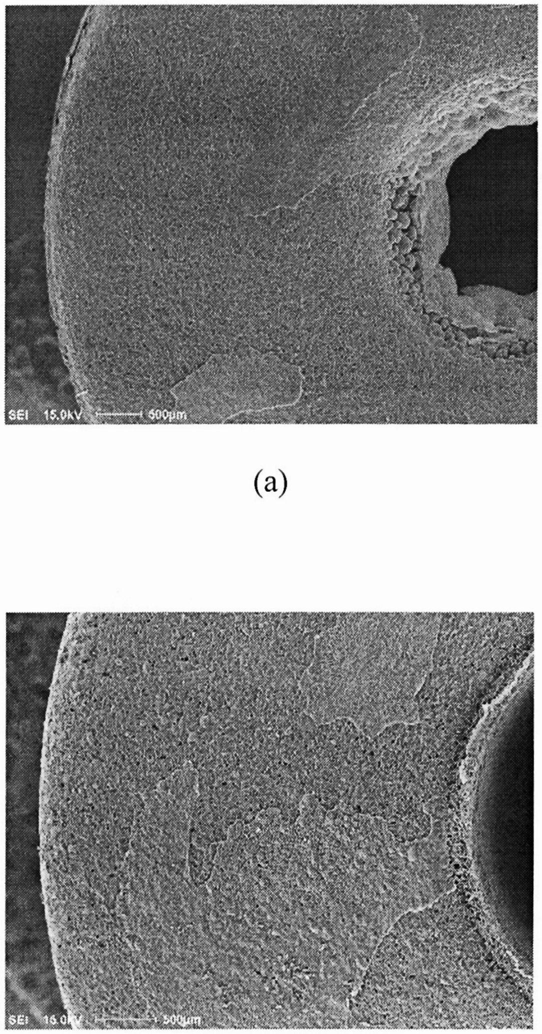

(a)

(b)

Figure 6-33: SEM pictures of the cathode surface structure after treatment by stable arcs. The operating conditions were 0 slpm, 3.0 cm, 30 minutes, and 300 A for (a), EXP-81 and 15 slpm, 3.0 cm, 30 minutes, and 300 A for (b), EXP-83.

6.2.6. Effect of Arc Current on The Arc Stability

Figure 6-34 shows ΔV for complete runs at gas flow rates of 0 and 15 slpm as a function of arc current. For the higher gas flow rate, the arcs were always stable. For 0 slpm, the stability increased with increasing arc current as is expected. This is probably due to a combination of higher arc root temperature caused by the higher heat flux at higher currents as well as increased electromagnetic pumping. This pumping, known as the Maecker effect, stiffens the arcs making them more resistant to lateral motion and thus reducing voltage fluctuations.

6.2.7. Hypothesis about The Arc Stability of The Hollow Graphite Cathode

As discussed in the previous parts, the arc stability of the cathode may be associated with the mode transition of the arc cathode operation. The following hypothesis was based on observations from this work as well as the mode transition introduced in the literature review.

The Hypothesis

The stable operation of the hollow graphite cathode is in the thermionic emission regime; the unstable operation is in the thermofield emission regime.

In the next part, proof of this hypothesis is given by presenting results of 1) estimation of current densities with SEM pictures, 2) Fast Fourier Transform (FFT) of the total voltage, and 3) cathode surface temperatures.

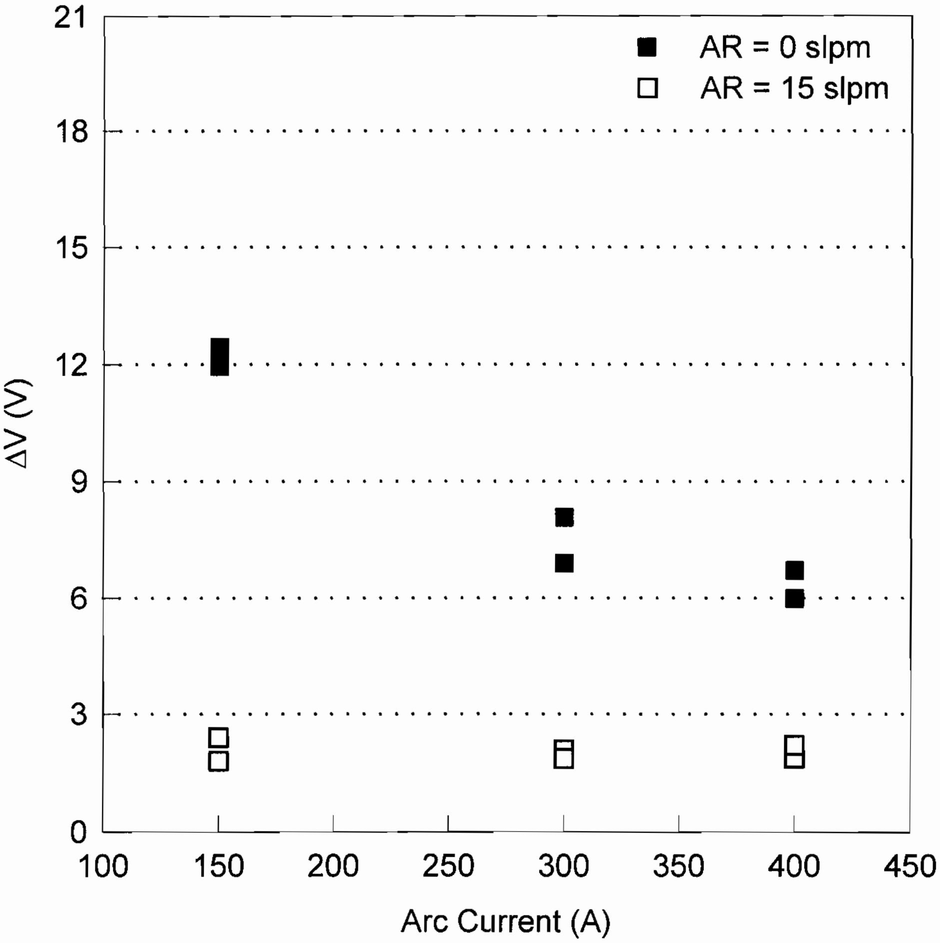

Figure 6-34: Effect of the arc current on the arc stability using cathode I at different argon gas flow rates for an initial interelectrode gap of 1.5 cm and an arc duration of 120 minutes for 150 A and 30 minutes for 300 and 400 A.

6.2.8. Proof of The Hypothesis

6.2.8.1. Estimation of Current Densities of The Stable and The Unstable Operation

After each stable run, arc tracks on the surfaces of cathode I could be seen without a microscope. Figure 6-35 (a) shows the arc tracks on the surface after a stable 150 A run (EXP-12). On the cathode surface several arc tracks could be observed, and the width of the arc track was about 2 mm. The SEM was used to examine the surface structure of the arc track; an example is shown in Figure 6-35 (b). The surface structure is quite uniform and looks like crystal growth. The surface structure before arc treatment is presented in Figure 6-35 (c) to compare the structures before and after a stable arc; before arc treatment the structure looks rough and irregular. For stable 300 A runs the width of the arc track was thicker; for EXP-52 operated at the same initial interelectrode gap and argon gas flow rate of EXP-12, it was about 4 mm. For 150 A runs some thermionic spots could be observed; however, for 300 A runs they could not be seen. The shape of the thermionic spot observed was almost circular, and the diameter was about 2 mm. Using this size, the current density (J) of 4.8 x 10^7 A/m^2 could be estimated for the stable 150 A run. This current density belongs to the general range of the current density of the thermionic emission regime (10^7~10^8 A/m^2). In addition, the temperature at the thermionic spot surface was estimated using the current density (J) of 4.8 x 10^7 A/m^2 and the Richardson equation. The Richardson equation is given as follow:

$$J = AT^2 \exp(-\frac{e\phi}{kT}) \qquad (6\text{-}1)$$

where J is the current density estimated; T is the temperature of the thermionic spot surface; A is the emission constant of 1.2 x 10^6 A/m^2-K^2; k is the Boltzmann's constant of 1.381 X 10^{-23} J/K; and ϕ is the work function of 5 V. The values of the emission constant and the work function were taken from Roth (1995). The temperature of 4430 K was estimated at the thermionic spot surface for the stable 150 A run.

The unstable operation did not produce the arc tracks on the cathode surfaces, and therefore, the SEM was used to search for cathode spots. Figure 6-36 (a) shows some cathode spots found after an unstable arc 150 A run. There were several different sizes of the cathode spots. Normally diameters of the cathode spots in the picture are about 40 ~ 50 μm. A diameter of about 45 μm of the cathode spot indicated by the arrow in Figure 6-36 (a) was selected to estimate the current density. The current density of 9.4 x 10^{10} A/m^2 was estimated for the cathode spot. However, because there are several cathode spots at the arc root in the thermofield emission regime, it was assumed that 2 cathode spots made up the arc root. It was based on the spot current of 200 A reported by Kimblin (1973). With this assumption the current density of 4.7 x 10^{10} A/m^2 was estimated. This current density is in the general range of the current density of the thermofield emission regime (10^{10}~10^{11} A/m^2). For unstable 300 A runs, the cathode spots could not be found, but remnants of the cathode spots could be observed. One such remnant is the cauliflower structure as shown in Figure 6-36 (b). Kandah (1997) reported that the cauliflower structure is one of the characteristics of the cathode spots of graphite cathodes operated in the thermofield emission regime.

The surface structure of the EXP-29 cathode for Figure 6-36 (a) was further investigated. Attention was focused on finding the structure difference after stable and unstable arc

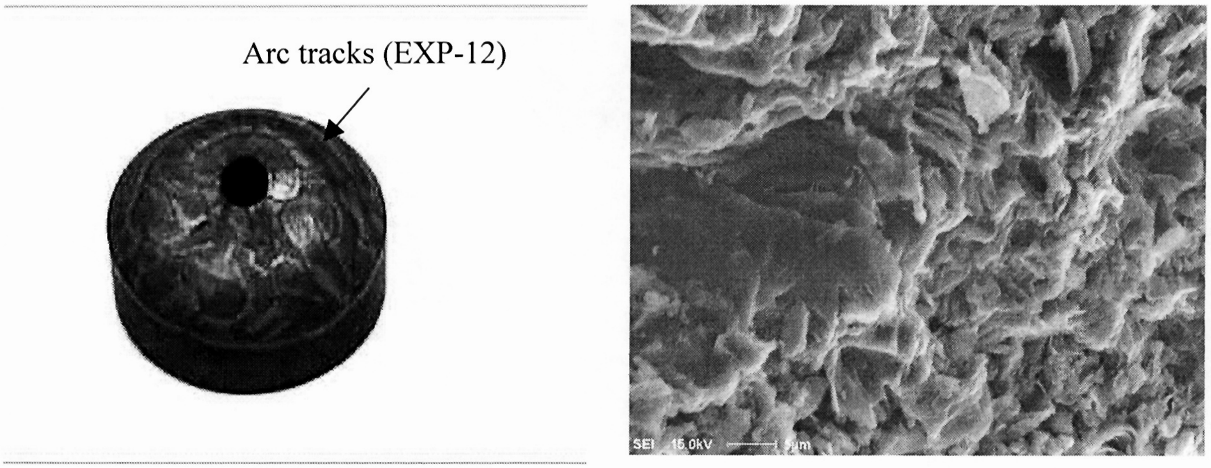

(a): arc tracks after stable arc treatment.

(c): surface structure before arc treatment.

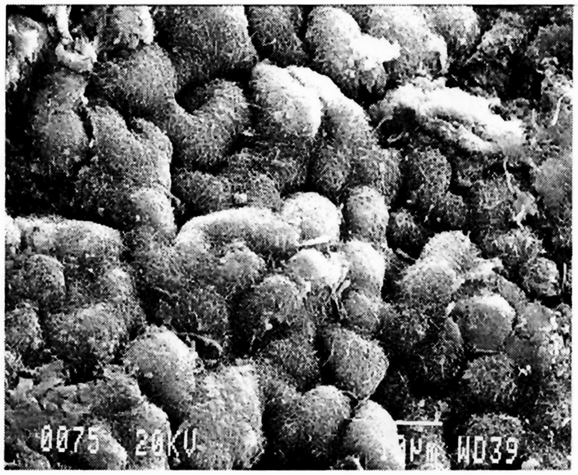

(b): surface structure inside an arc track after stable arc treatment.

Figure 6-35: The arc tracks, the surface structure inside an arc track after a stable arc run, and the surface structure before arc treatment. The stable run used cathode I at 1.5 cm, 15 slpm, and 150 A.

treatment; the arc was first stable and then unstable. Figure 6-37 shows the difference. During the stable operation the arc remained mainly in the central part of the cathode because of the absence of the argon gas injection while during the unstable operation the arc moved rapidly over the outer surface of the cathode. Figures 6-37 (b) and (c) are two different magnifications of the cathode surface taken in the area labeled “stable” and “unstable” in Figure 6-37 (a). Figure 6-37 (b) shows the structure characteristic after the stable arc treatment. The crystal structure of the original graphite has coarsened due to the thermal treatment by the stable arc. This modification in structure was possible because the arc remained in one location over a considerable length of time giving a high temperature in this regime. Figure 6-37 (c) presents the surface structure after the unstable arc treatment. It is possible to see many circular holes on the cathode surface. These vary in diameter from about 10 μm to about 60 μm and are believed to be cathode spots resulting from operation in the thermofield emission. The cathode spots in Figure 6-36 (a) were found in this area.

6.2.8.2. Total Voltage and Total Voltage FFT Analysis of The Stable and The Unstable Operation

FFT of the total voltage during the stable and the unstable operation was performed using an oscilloscope. The operating conditions of the run for this analysis were an initial interelectrode gap of 3.0 cm and an argon gas flow rate of 4.5 slpm at 150 A. Figure 6-38 shows the total voltage pattern of the run recorded by the data acquisition system. Before the arc duration of about 30 minutes the arc was stable, and after that the arc became unstable.

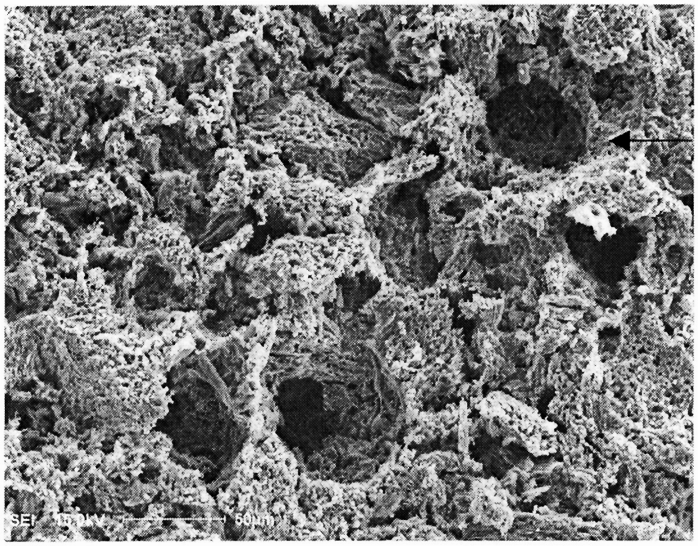

(a): the cathode spots (150A, EXP-29)

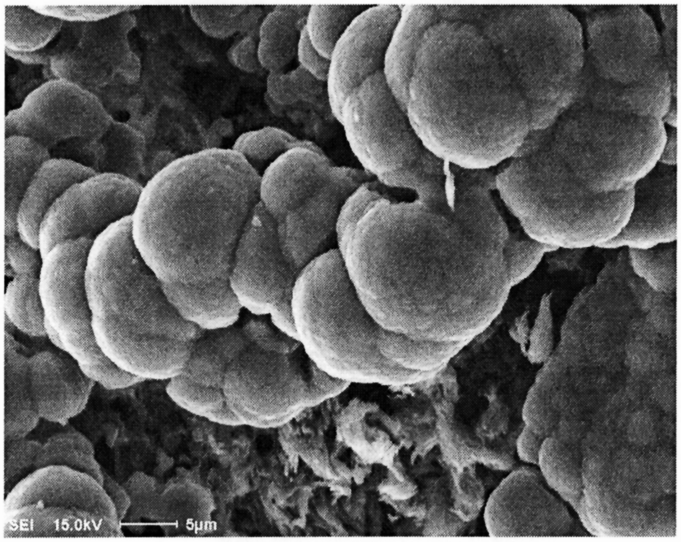

(b): the cauliflower structure (300A, EXP-59)

Figure 6-36: The cathode spots and the cauliflower structure after an unstable run using cathode I for an initial interelectrode gap of 3.0 cm, an argon gas flow rate of 0 slpm, and an arc current of 150 A (EXP-29) and 300 A (EXP-59).

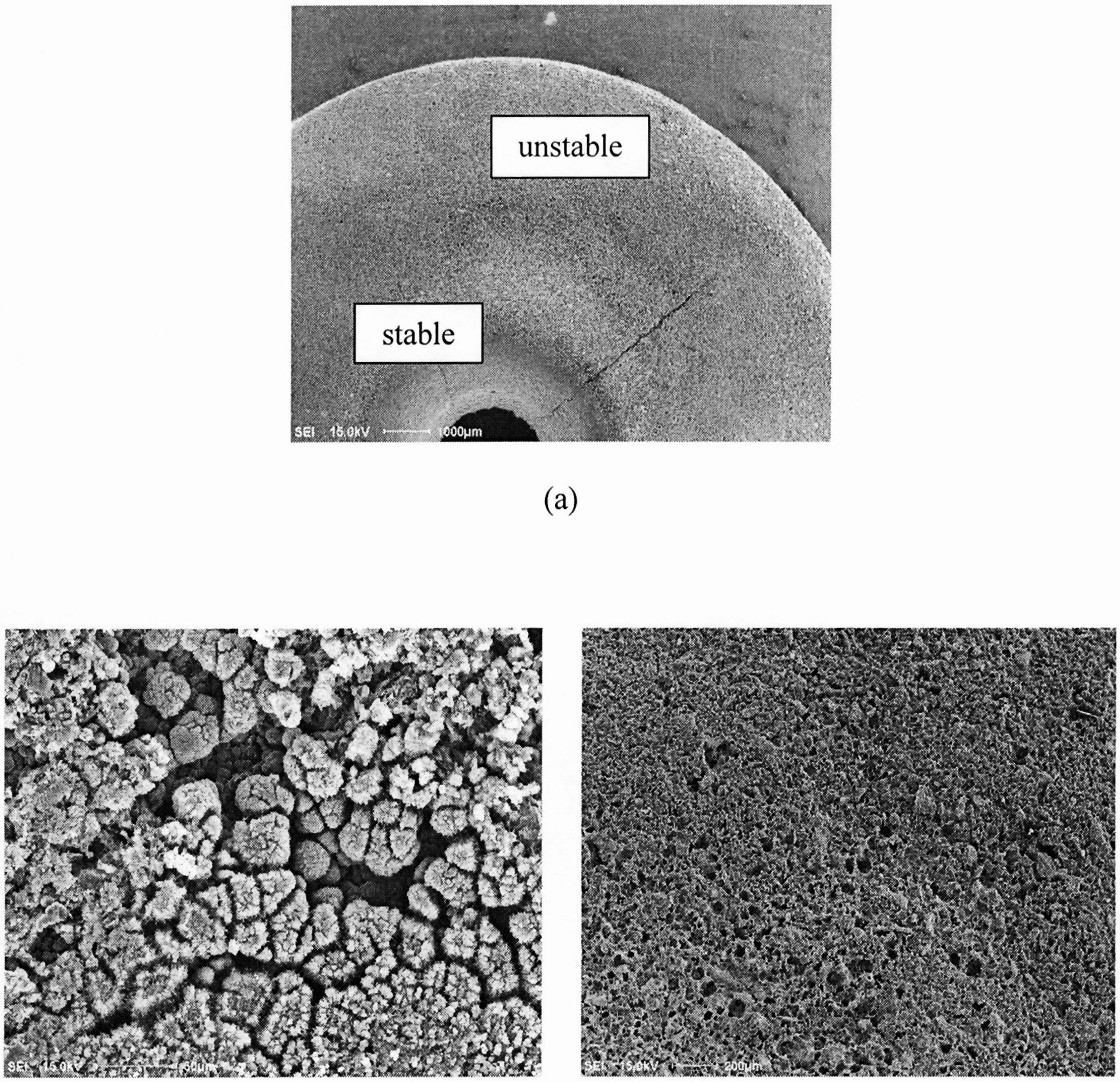

(a)

(b)

(c)

Figure 6-37: SEM micrographs of a cathode after operation using cathode I for an initial interelectrode gap of 3.0 cm, an argon gas flow rate of 0 slpm, and an arc current of 150 A (EXP-29). The macroscopic view of the regions examined is (a); the surface structure after the stable arc treatment is (b) and after the unstable arc treatment is (c).

The FFT waveforms of the total voltage were randomly printed during the stable and the unstable operation using hard copy and the single mode of the scope. The valid range of the FFT waveforms using this scope was determined by standard sine waveforms of 180 Hz and 1 MHz, produced by a signal generator. The 180 Hz signal was chosen for the analysis of a low frequency region, and the FFT waveforms in this region were reliable to 5 KHz. The 1 MHz signal was for the analysis of a high frequency region, and the FFT waveforms in this region were reasonable to 250 MHz.

Firstly, total voltage patterns in a time of the order of subseconds measured by the scope are presented in Figure 6-39. Like the total voltage patterns recorded by the data acquisition system, these total voltage patterns showed a clear difference between the stable and the unstable arc runs. For the stable operation, the voltage signal is a rectified sine wave and is periodic as shown in Figure 6-39 (a). The period of the voltage signal in the stable part is 5.6 ms. This period is the same for the other time scales. Peak to peak voltage (V_{pp}) in this stable part is in the range of 3.0 ~ 4.0 V. Meanwhile, the voltage signals of the unstable operation are irregular waveforms as shown in Figures 6-39 (b), (c), and (d). They resemble saw-tooth waveforms incorporating with several sharp peaks. Ghorui et al. (2000) presented similar voltage patterns; they studied the relationship between the fluctuations of the arc voltage and the arc root movement using copper electrodes and reported that the peaks were associated with the movement of the arc root. They did not mention the arc cathode operation mode, but copper electrodes normally operate in thermofield emission. It seems that the irregular voltage patterns and the peaks of this work are also related to the arc operation in the thermofield emission. In addition,

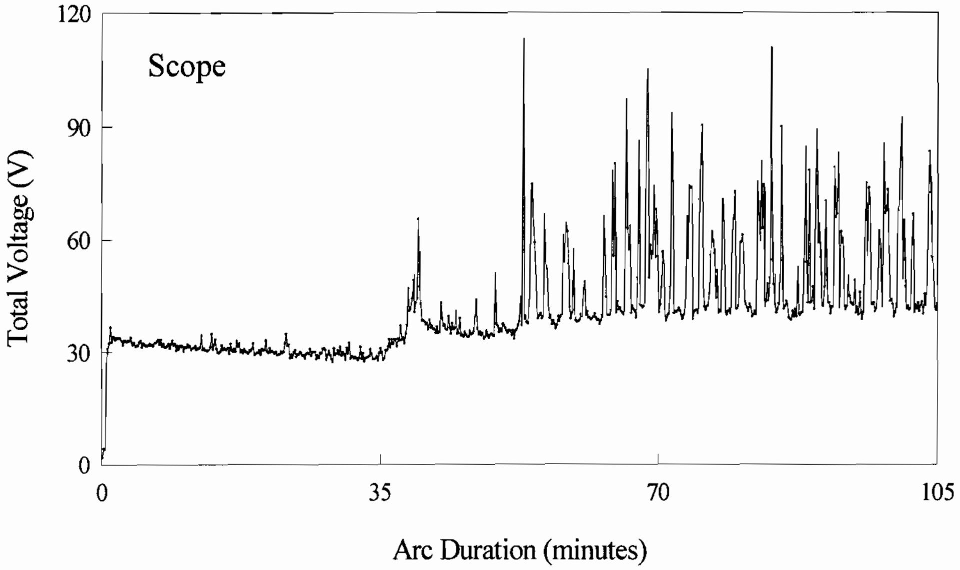

Figure 6-38: Total voltage pattern using cathode I for an initial interelectrode gap of 3.0 cm and an argon gas flow rate of 4.5 slpm at 150 A.

in the unstable operation the negativity of the cathode was increased, i.e. higher total voltage. In Figure 6-39 (a) the voltage of the stable operation is about –30 V; however, some peaks in the unstable operation in Figures 6-39 (b), (c), and (d) reaches about –100 V. Also, the V_{pp} in the unstable operation showed a wider and higher range; it is between about 10 and 60 V in the figures.

The FFT waveforms for the stable and the unstable operation are presented in Figures 6-40 and 6-41, respectively. For the stable arc run, the FFT waveforms show a periodic phenomenon as shown in Figure 6-40. The fundamental frequency is 180 Hz, and the main harmonic frequencies are 0, 360, 540, 720, 900, and 1080 Hz. Ghorui et al. (2000) stated that this harmonic series is a quasi-periodic waveform which is defined as comprising a peak at zero frequency and integral multiples of the fundamental frequency present in the waveform. The fundamental frequency of 180 Hz in the FFT waveforms was the same as the frequency of the total voltage of the stable part, and this quasi-periodic FFT waveform came from the operation of the power supply. In the unstable operation, the FFT waveforms are totally different as shown in Figure 6-41. They showed a continuous broadband noise waveform. This noise waveform includes the fundamental frequency of 180 Hz and higher frequencies that do not exist in the stable arc run. The arrow in Figure 6-41 (a) indicates 180 Hz. Therefore, it is believed that frequencies in this noise spectrum come from both the operation of the power supply and the unstable arc. To find the end point of this continuous broadband noise waveform in this run, the horizontal scale of the scope was increased, and the results are presented in Figure 6-41

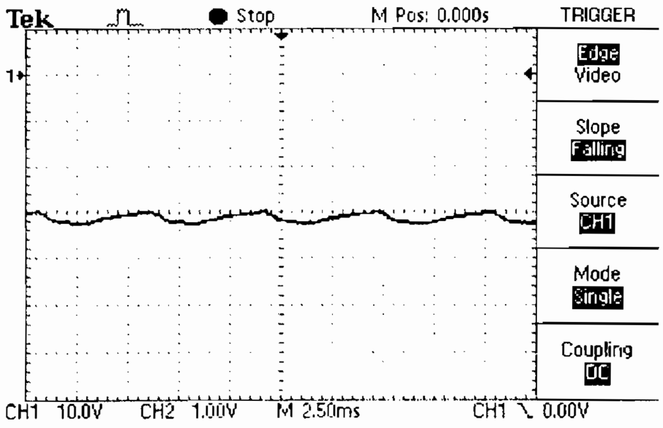

(a)-stable

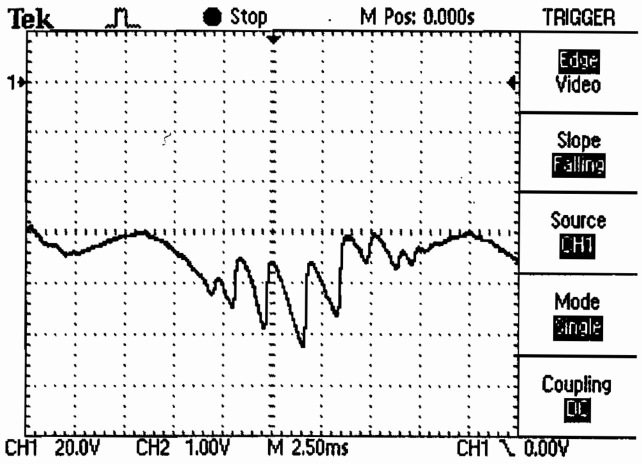

(b)-unstable

Figure 6-39: Total voltage patterns using cathode I for an initial interelectrode gap of 3.0 cm and an argon gas flow rate of 4.5 slpm at 150 A. The 1 indicates 0 V. The horizontal scales of (a) and (b) are 2.5 ms per division. The vertical scale is 10 V per division for (a) and is 20 V per division for (b).

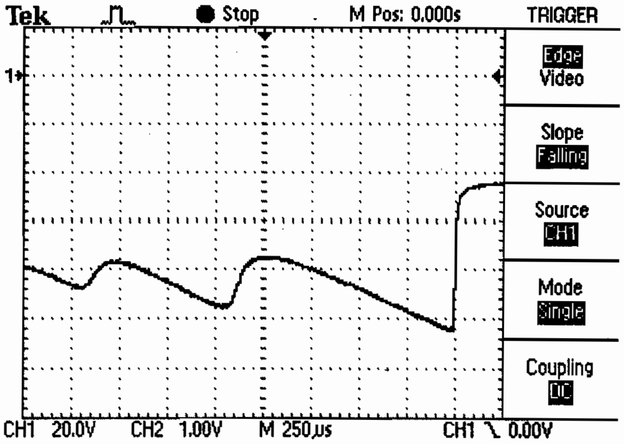

(c)-unstable

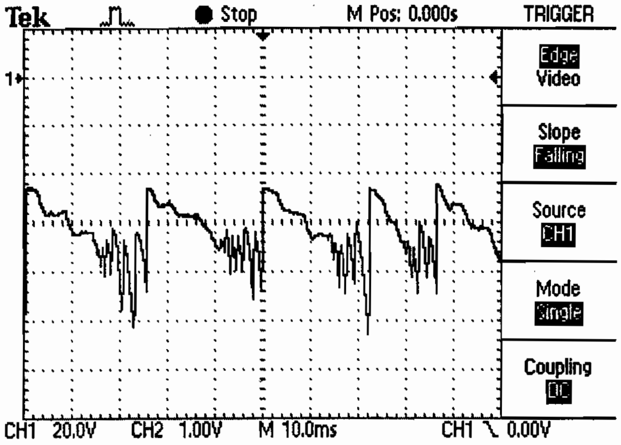

(d)-unstable

Figure 6-39: Total voltage patterns using cathode I for an initial interelectrode gap of 3.0 cm and an argon gas flow rate of 4.5 slpm at 150 A. The 1 indicates 0 V. The horizontal scale is 250µs per division for (c) and is 10 ms per division for (d). The vertical scales of (c) and (d) are 20 V per division. (continued) (d). The continuous broadband noise waveform might end at about 100 kHz for this run. Some frequencies higher than 100 kHz appeared, but they are discrete.

In the stable operation characteristic FFT frequencies associated with the stable arc could not be found because of much stronger intensities of the FFT waveforms from the power supply operation. However, in the unstable operation, it seems that especially, the higher frequencies around 100 kHz in the noise waveform may represent the lifetime scale of the macrospot in the thermofield emission. As discussed in the literature review, the lifetime scale of the macrospot in the thermofield emission regime is much less than 1 ms scale and probably of the order of 1 μs. The higher frequencies of 100 kHz in the unstable operation correspond to a time of the order of 10 μs. Therefore, it could be thought that the higher frequencies might be associated with the extinction and the re-ignition of the macrospot in the thermofield emission regime.

6.2.8.3. Cathode Surface Temperature

The cathode surface temperature for the stable operation could be measured using the single wavelength pyrometer, and the results of these temperature measurements are presented in Table 6-2. The cathode surface temperature at the blackbody hole depended strongly on the arc root position. The color of the blackbody hole of cathode II was bright when the arc was close to the hole and was black when the arc was far away from the hole. For the unstable operation, however, the temperature measurement could not be performed because the arc radiation was too strong to see the color of the hole, and the position of the arc changed very rapidly.

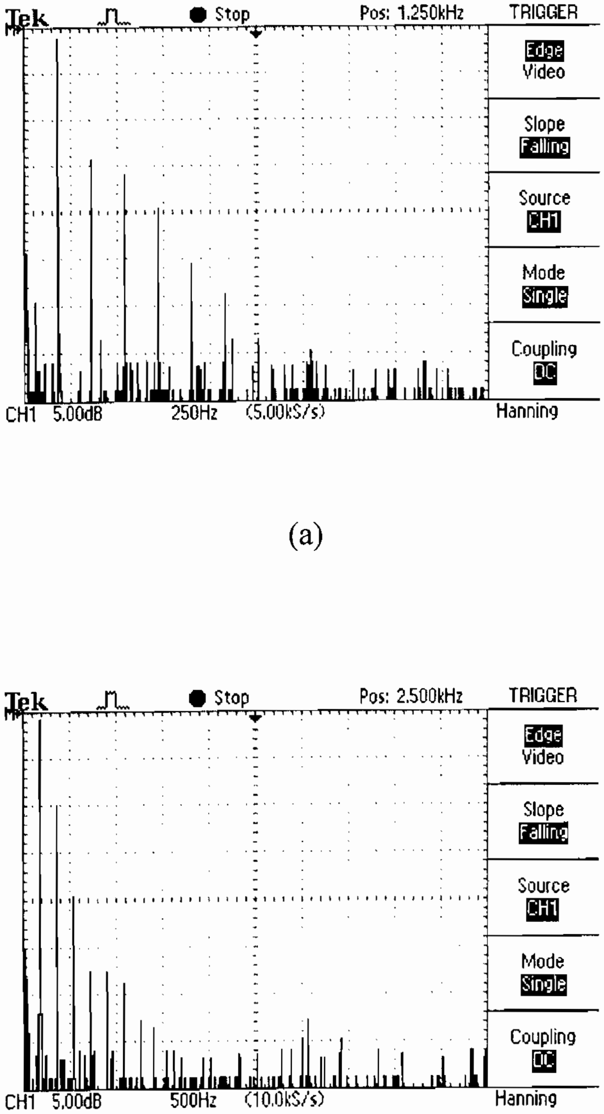

(a)

(b)

Figure 6-40: FFT waveforms of the stable arc run using cathode I for an initial interelectrode gap of 3.0 cm and an argon gas flow rate of 4.5 slpm at 150 A. The horizontal scale is 250 Hz per division for (a) and is 500 Hz per division for (b). The vertical scales of (a) and (b) are 5 dB per division.

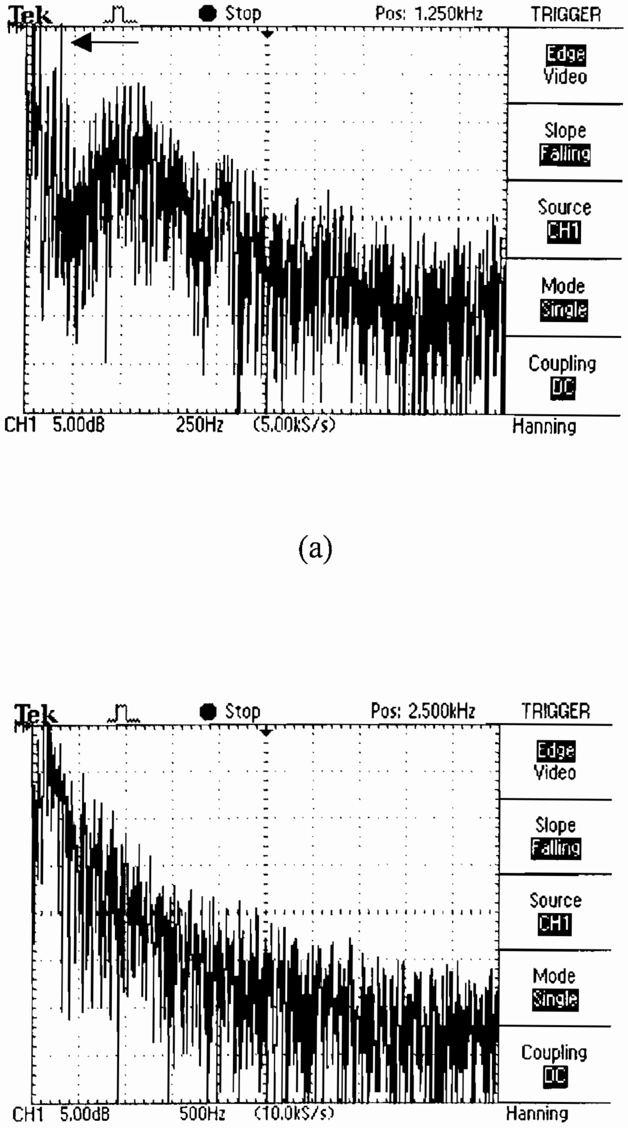

(a)

(b)

Figure 6-41: FFT waveforms of the unstable arc run using cathode I for an initial interelectrode gap of 3.0 cm and an argon gas flow rate of 4.5 slpm at 150 A. The horizontal scale is 250 Hz per division for (a) and is 500 Hz per division for (b). The vertical scales of (a) and (b) are 5 dB per division.

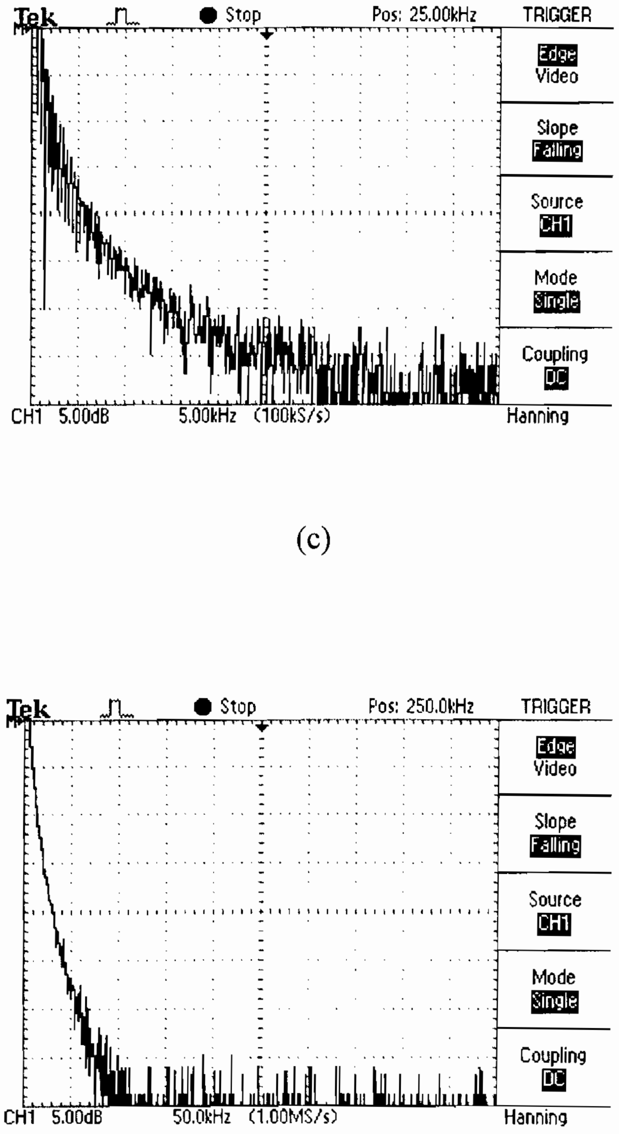

(c)

(d)

Figure 6-41: FFT waveforms of the unstable arc run using cathode I for an initial interelectrode gap of 3.0 cm and an argon gas flow rate of 4.5 slpm at 150 A. The horizontal scale is 5 kHz per division for (c) and is 50 kHz per division for (d). The vertical scales of (c) and (d) are 5 dB per division. (continued)

The stable experimental conditions for this temperature measurement were an initial interelectrode gap of 3.0 cm and an argon gas flow rate of 4.5 slpm at 150 and 300 A. For 150 A the temperature of cathode I at the hole was about 1340 K. When considering the temperature of the thermionic spot estimated at 150 A (4430 K), it could be seen that the temperature gradient from the arc root to the hole was very steep. For 150 A the temperature of cathode II at the hole was between about 1600 ~ 1710 K. Direct comparison between this temperature at 150 A using cathode II and the temperature of 1340 K at 150 A using cathode I could not be done because of the different hole positions. The hole was made just above the cathode tip. Due to the different outer diameter, the hole position of cathode I was 8 mm and that of cathode II was 4 mm from the end of the cathode tip. Therefore, arc pictures were used for direct comparison. The arc pictures taken during stable 300 A runs shows the temperature distribution difference between cathode I and II as presented in Figure 6-42. These pictures are already introduced in Figures 6-12 and 6-18. These pictures of the same exposure time and the similar arc root position were chosen to compare the tip surface colors of the cathodes. The colors of the tips show the temperature difference. As presented in Figure 6-42, the tip of cathode II near the arc root is red and brighter. The red zone of cathode II extends to about 7 mm above the tip; therefore, it reaches to about 11 mm from the end of the cathode tip. Meanwhile, the color just above the cathode I tip, which is 8 mm from the end of the cathode I tip, is black. It indicates that operation of cathode II was at higher temperature. Other red zones of cathode II, which are longer than that of Figure 6-42 (b), can be also seen in Figures 6-18 (a) and (b). This higher temperature of cathode II was due to the smaller diameter of cathode II. That caused less heat dissipation through the conduction from the arc root to the bulk cathode, thus giving the higher temperature. The temperature of cathode II at the hole for 300 A was increased as expected and was between 1760 and 1910 K.

Comparison of the temperature difference between the stable and the unstable operation could not be made using the single wavelength pyrometer because of the rapidly fluctuating arc radiation. This arc radiation also interfered with the temperature measurement with the two-wavelength pyrometer. Therefore, cooling curves after the arc shut down were considered to see the temperature difference between the stable and the unstable arc runs at 150 A. Figures 6-43 and 6-44 present the temperature recording using the two-wavelength pyrometer and the cooling curves after the stable and the unstable operation, respectively. During the stable arc runs, a constant temperature of 2996 K was maintained. That was much higher than the stable part temperature of 1340 K measured by the single wavelength pyrometer at 150 A. The temperature of 2996 K represents the maximum temperature of the two-wavelength pyrometer. It corresponds to an output of 1 V which is the maximum output for this instrument. Thus, during the entire arc operation, the two-wavelength pyrometer showed its maximum temperature because of the arc radiation. In contrast to the constant temperature of 2996 K in the stable operation, in the unstable operation the temperature recording fluctuated greatly as did the total voltage. To avoid the interference of the arc radiation when using the two-wavelengths pyrometer, the starting temperatures of the cooling curves were used to examine the temperature difference between the stable and the unstable operation. The starting temperature after the stable operation was always higher than that after the

Table 6-2: The cathode surface temperature for the stable operation

Cathode Type	Arc Current (A)	Temperature (K)
Cathode I	150	1340 K 1)
Cathode II	150	1600 ~ 1710 K 2)
Cathode II	300	1760 ~ 1910 K 2)

1) Measured at 8 mm from the end of the cathode tip.

2) Measured at 4 mm from the end of the cathode tip.

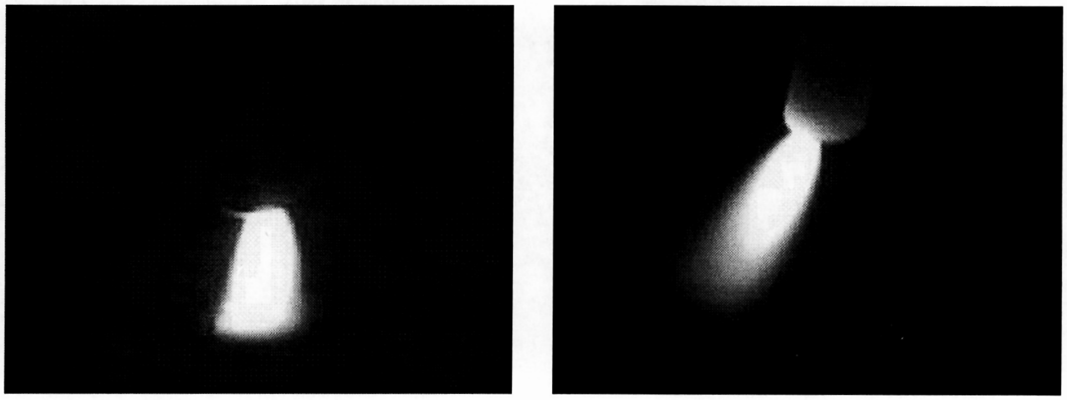

(a) Cathode I

Voltage: 31 V, Exposure:11

(b) Cathode II

Voltage: 41 V, Exposure: 11

Scale 1:1.03

Figure 6-42: Arc pictures taken during stable arc runs to compare the cathode surface temperature between cathode I and II at 3.0 cm, 4.5 slpm, and 300 A.

unstable operation if other operating conditions were the same; an example is shown in Figures 6-43 and 6-44. Thus, although the measurements are approximate because they were taken relatively far from the arc root, it has been shown that the cathode tip is hotter under stable arc conditions. This supports the hypothesis that the stable arc is in the thermionic mode of emission.

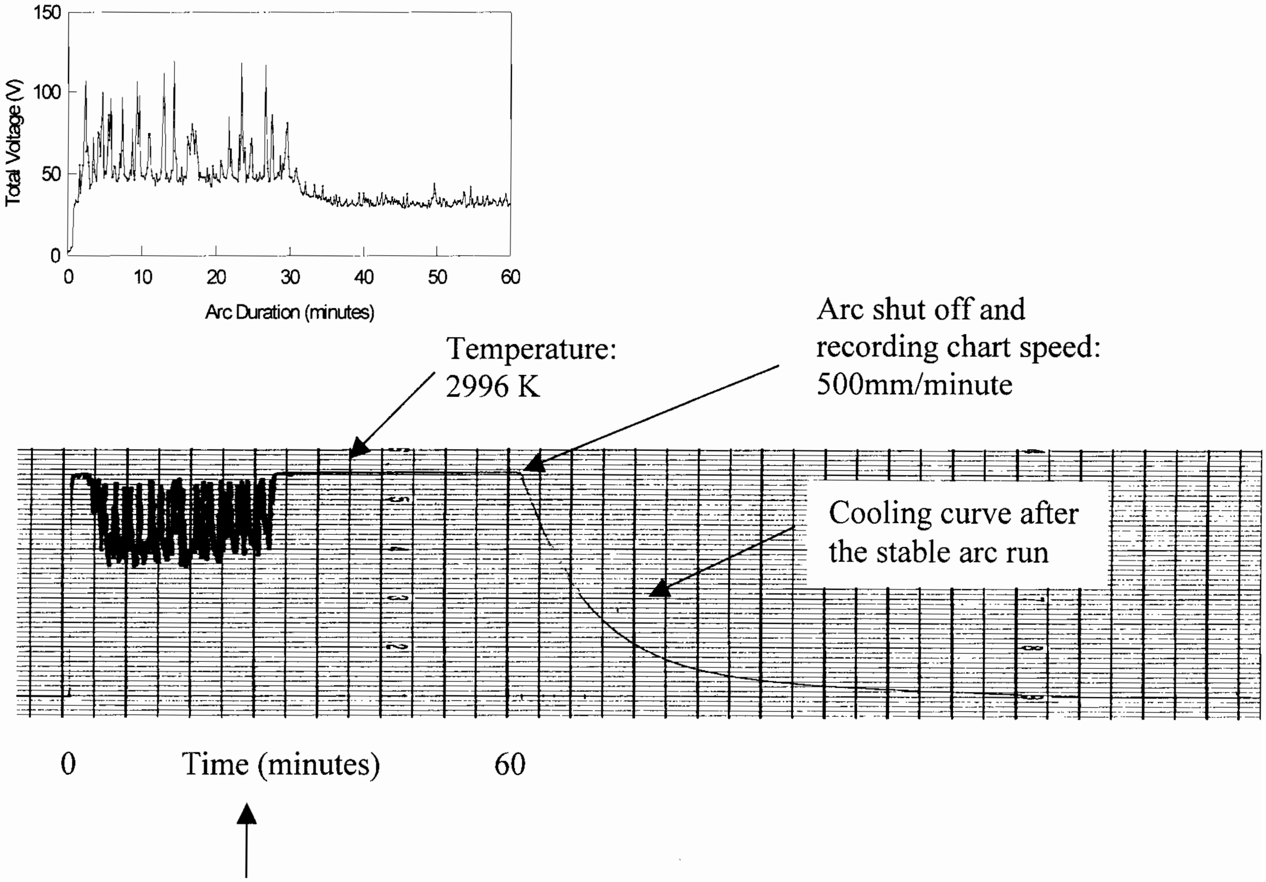

Temperature: 2996 K

Arc shut off and recording chart speed: 500mm/minute

Cooling curve after the stable arc run

Arc operation and recording chart speed: 1 mm/minute

Figure 6-43: The cooling curve after the stable arc run using cathode I for an initial interelectrode gap of 3.0 cm, an argon gas flow rate of 4.5 slpm (the unstable part) and 15 slpm (the stable part), and an arc current of 150 A.

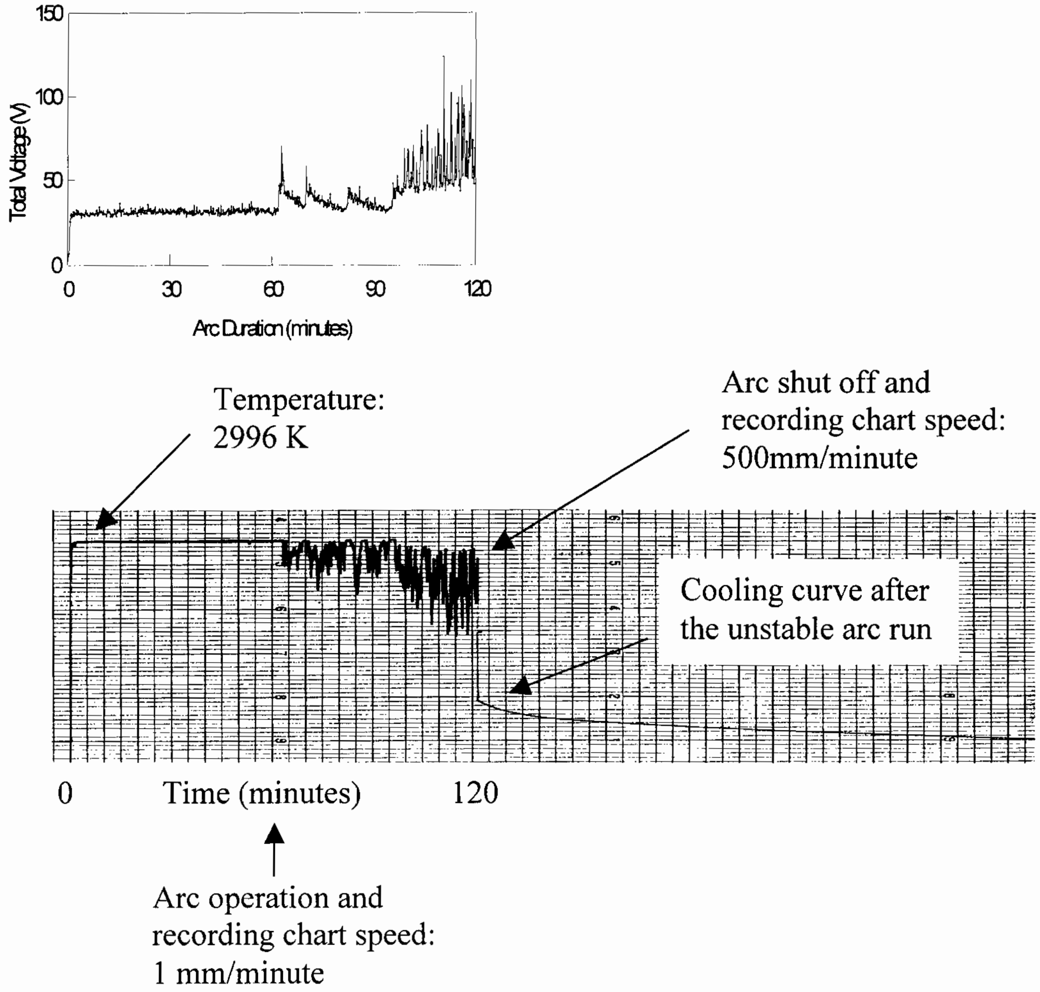

Temperature: 2996 K

Arc shut off and recording chart speed: 500mm/minute

Cooling curve after the unstable arc run

Arc operation and recording chart speed: 1 mm/minute

Figure 6-44: The cooling curve after the unstable arc run using cathode I for an initial interelectrode gap of 3.0 cm, an argon gas flow rate of 0 slpm, and an arc current of 150 A.

6.3. EROSION BEHAVIOR OF THE HOLLOW GRAPHITE CATHODE

Erosion rates of the graphite cathode were measured at 150, 300, and 400 A with variation of the argon gas flow rate and the initial interelectrode gap. The measurement of the erosion rate was performed through weighing the mass loss of the cathode before and after each run. This was determined to ± 0.01 g giving a maximum uncertainty in the erosion measurements of about ± 2 %. By analyzing the erosion rates, general erosion behavior of the cathode using a graphite anode could be understood. Effects of the argon gas flow rate and the initial interelectrode gap on the erosion rate are first presented because these effects were related to the arc stability. This is followed by the relationship between the erosion rate and the arc stability. A correlation model for the erosion rate is introduced last.

In the 150 A experiments, since the arc was ignited by separating the electrodes after the contact, a small amount of graphite from the cathode might have been lost by breakage even though the lowering speed of the cathode was only 0.04 cm per second. Therefore, to find optimal arc duration at 150 A to measure the erosion rate, different arc times were tried. Figure 6-45 shows the effect of run time on the erosion rate for the initial interelectrode gap of 1.5 cm and the argon gas flow rate of 10 slpm at 150 A. All runs in Figure 6-45 were stable, i.e. the same arc cathode operation mode. There is a slight initial decrease in the erosion rate with time, which is probably due to the mass loss on contact; then the erosion rate becomes independent of time after about 80 minutes. Therefore, 120 minutes was determined as the arc duration for 150 A runs. Meanwhile, for 300 and 400 A runs the arc duration was 30 minutes. Those runs did not contain the mass loss due to

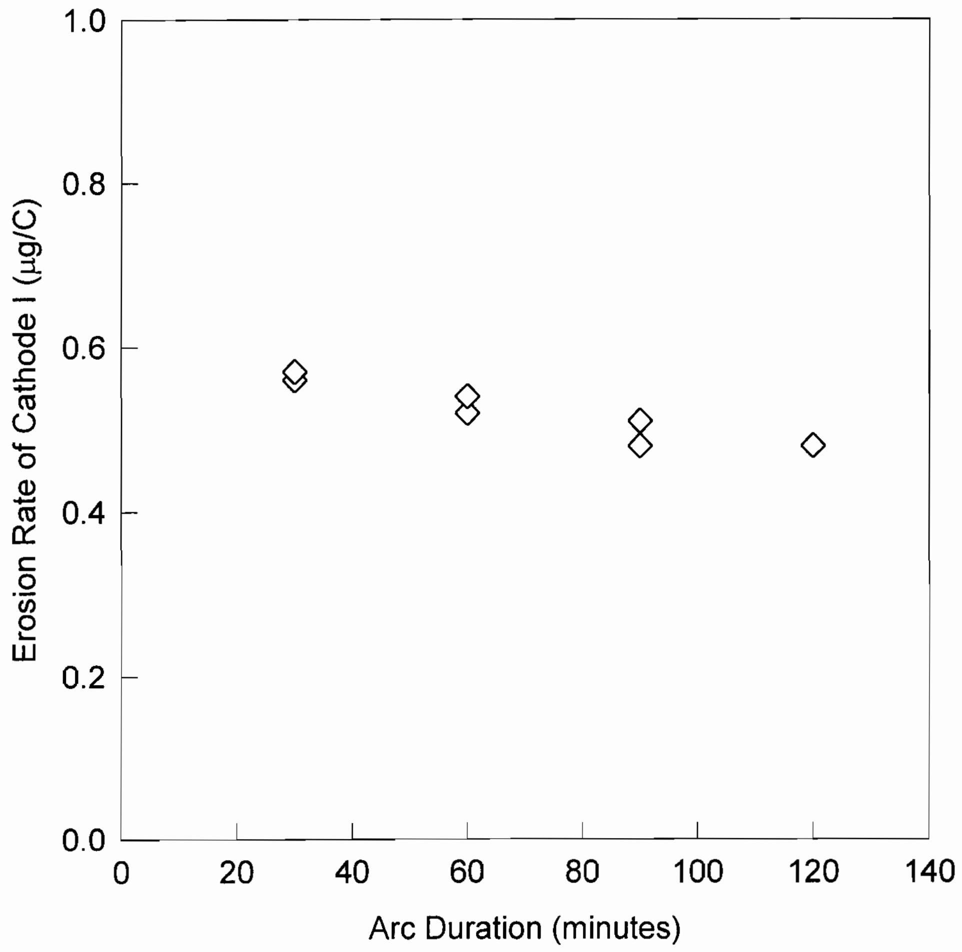

Figure 6-45: Erosion rates of cathode I as a function of time for an initial interelectrode gap of 1.5 cm and an argon gas flow rate of 10 slpm at 150 A.

the contact because of the use of the high frequency arc starter.

6.3.1. Effect of Argon Gas Flow Rate on Erosion Rate

Figure 6-46 presents the erosion rates as a function of the argon gas flow rate at 150 A. Compared with the argon gas flow rates of 10 and 15 slpm runs, the erosion rates for the argon gas flow rates of 0 and 4.5 slpm and the initial interelectrode gap of 1.5 and 3.0 cm runs were much higher. The difference between the lower and the higher argon gas flow rate runs was the mode of the arc cathode operation as discussed in the earlier section. For the higher argon gas flow rates the cathode operated in the thermionic emission regime, while in case of the lower argon gas flow rates the cathode included both the thermionic emission regime for the stable part and the thermofield emission regime for the unstable part. Therefore, it was believed that the unstable arc operation in the thermofield emission regime produced more erosion of graphite from the cathode. It is well known that the current density of the thermofield emission regime is greater than that of the thermionic emission regime; therefore, during the unstable arc operation of the lower argon gas flow rate runs, probably the local heat flux to the cathode spots by the ion bombardment was higher, thus resulting in more erosion of the graphite. Ejection of graphite particles caused by the arc movement would also influence the erosion rate. For the higher argon gas flow rates, the argon gas flow rate affected the erosion rates only slightly. It was believed that this was because the thermionic emission regime was maintained for each complete run. In addition, in Figure 6-46 the erosion rates for the initial interelectrode gap of 3.0 cm at 0 slpm were lower than those for 1.5 cm and 0 slpm. That was due to the shorter arc duration, especially shorter unstable arc duration.

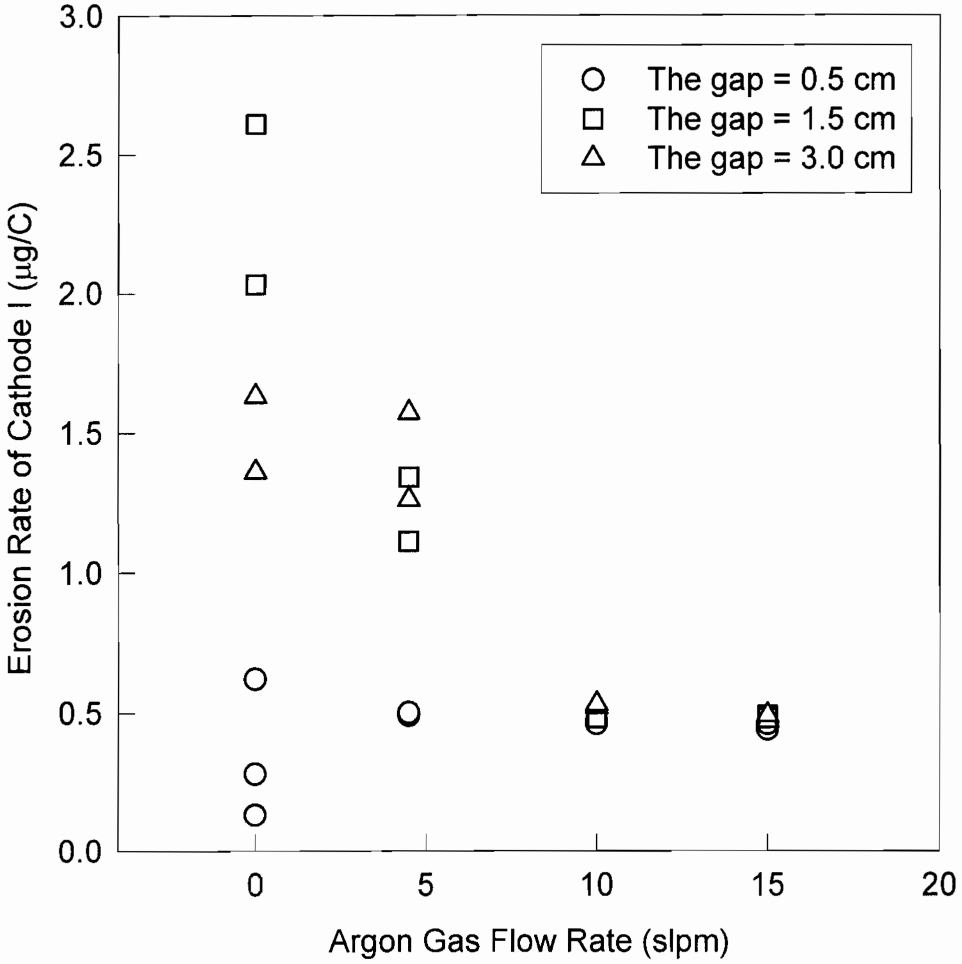

Figure 6-46: Erosion rates as a function of the argon gas flow rate using cathode I for an arc duration of 120 minutes at 150 A. The arc times of the runs at 3.0 cm and 0 slpm were 100 and 105 minutes.

The unstable arc duration for 3.0 cm at 0 slpm were about 49 and 63 minutes and that for 1.5 cm at 0 slpm were about 92 and 70 minutes.

Erosion behavior between 150 and 300 A was quite different, especially at the argon gas flow rate of 0 slpm. Figure 6-47 shows the erosion rates measured at 300 A and Figure 6-48 presents a comparison of the erosion behavior between 150 and 300 A runs at an initial interelectrode gap of 1.5 cm. Even though the highest erosion rate at 150 A was for the argon gas flow rate of 0 slpm, the lowest erosion rate at 300 A was also for the same argon gas flow rate, 0 slpm. The arc was unstable for 300 A and 0 slpm runs, but the erosion rates were lower. It is believed that these lower erosion rates were due to the redeposition of the carbon vapor, which was introduced in the equilibrium compositions. In case of fullerences synthesis using graphite electrodes, it has been reported that vaporized graphite from the electrodes can deposit on the cathode surface, thus reducing the erosion rate of the cathode. Figure 6-49 shows the cathode tip with a great deal of redeposited carbon for an experiment with an argon gas flow rate of 0 slpm and an initial interelectrode gap of 0.5 cm at 300 A. The mass of the cathode after the experiment increased and the erosion rate of this run was –1.30 μg/C. As the argon gas flow rate and the initial interelectrode gap increased, this carbon vapor redeposition became relatively weaker since the higher argon gas flow could wash out graphite species near the arc and the longer interelectrode gap could reduce the redeposition from the anode vapor jets.

The erosion rates for cathode I and II at 300 A as a function of the argon gas flow rate are plotted in Figure 6-50 for comparison. Table 6-3 shows operating conditions and the ΔVs

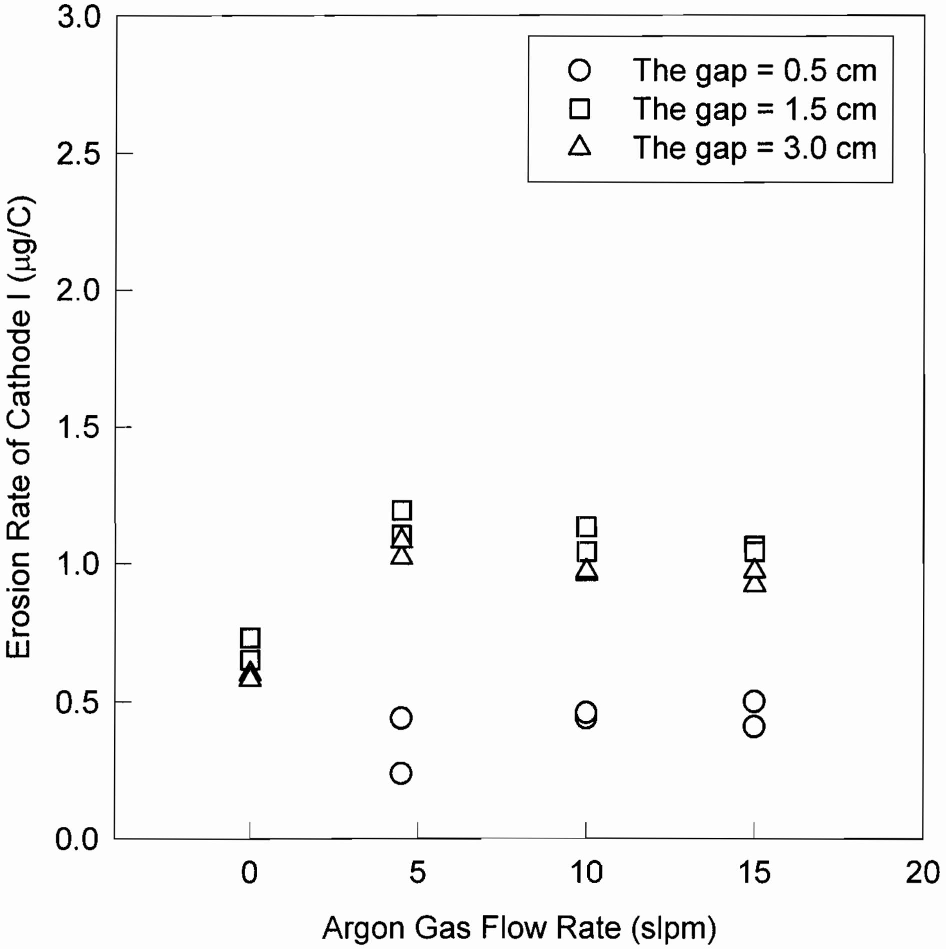

Figure 6-47: Erosion rates of cathode I as a function of the argon gas flow rate for an arc duration of 30 minutes at 300 A.

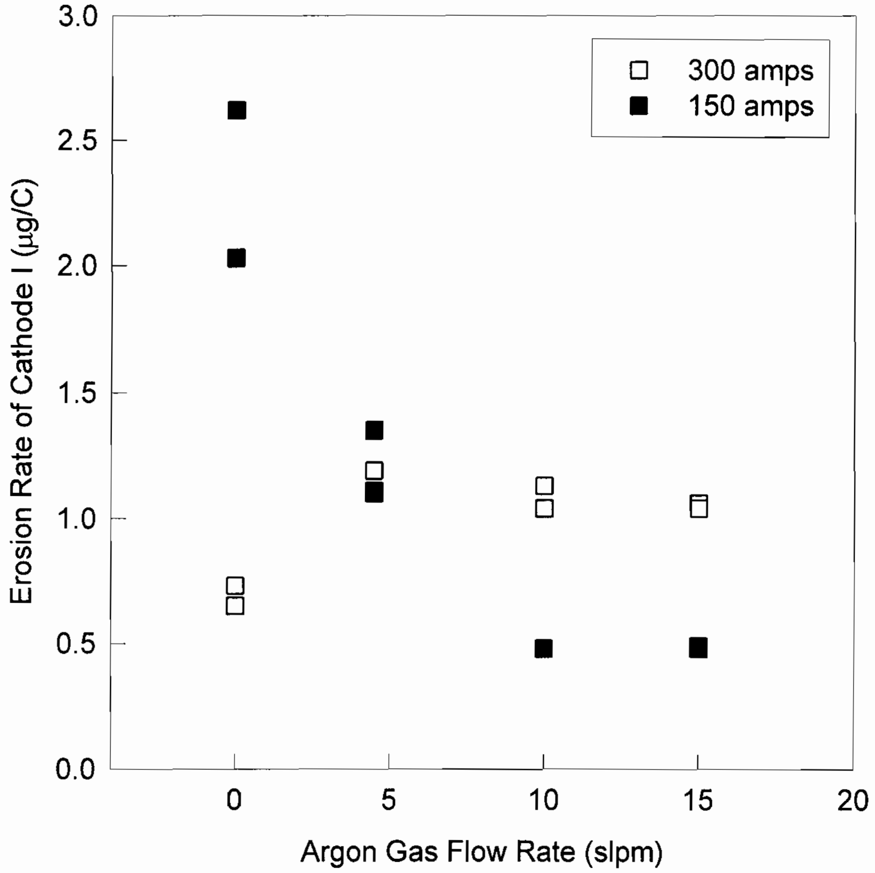

Figure 6-48: Comparison of erosion rates of cathode I between 150 and 300 A runs for an initial interelectrode gap of 1.5 cm, an arc duration of 120 minutes for 150 A runs, and an arc duration of 30 minutes for 300 A runs.

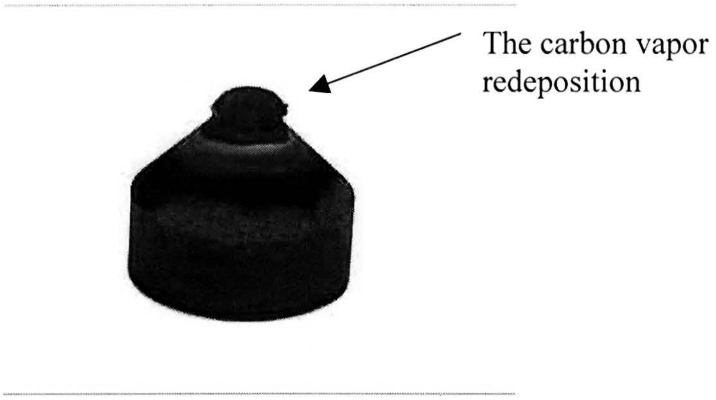

Figure 6-49: The highly redeposited cathode tip with carbon vapor.

of each whole run in Figure 6-50. The runs using cathode II were always stable operations while those using cathode I were stable or unstable according to the operating conditions. Regardless of the initial interelectrode gap change, the erosion rates of cathode I and II at 0 slpm were lower because of the redeposition of the carbon vapor. To compare erosion behavior between cathode I and II, the erosion rates at 15 slpm were considered because the runs were always stable. For the argon gas flow rate of 0 and 4.5 slpm, it was believed that this comparison was not reasonable because those runs included both the stable and the unstable operation. The erosion rates of cathode II at 15 slpm are slightly higher, and it is believed that the reduction of the cathode diameter resulted in higher arc root and cathode bulk temperatures, thus increasing the erosion rates.

Table 6-3: Operating conditions and ΔVs for cathode I & II at 300 A.

Cathode type	EXP-No.	Argon gas flow rate (slpm)	Initial interelectrode gap (cm)	ΔVs (V)
Cathode I	EXP-47&48	0	1.5	6.90 , 8.08
	EXP-59&60	0	3.0	4.45 , 2.49
	EXP-53&54	4.5	0.5	1.20 , 1.29
	EXP-49&50	4.5	1.5	3.40 , 5.01
	EXP-61&62	4.5	3.0	6.62 , 7.28
	EXP-55&56	10	0.5	0.80 , 0.66
	EXP-41&42	10	1.5	2.31 , 2.80
	EXP-63&64	10	3.0	3.06 , 4.77
	EXP-57&58	15	0.5	1.14 , 0.81
	EXP-51&52	15	1.5	2.07 , 1.86
	EXP-65&66	15	3.0	2.61 , 2.86
Cathode II	EXP-74 ~ EXP-83	0,4.5,10,15	0.5,1.5,3.0	0.60 ~ 2.30

6.3.2. Effect of Initial Interelectrode Gap on Erosion Rate

Erosion rates for the argon gas flow rate of 15 slpm at 150 and 300 A were used to study the effect of the initial interelectrode gap on the erosion rate because the arcs were always in the stable regime for these conditions, i.e. the same arc cathode operation mode. Figure 6-51 shows the erosion rates as a function of the initial interelectrode gap for the argon gas flow rate of 15 slpm at 150 A. The erosion rates increased slightly as the initial interelectrode gap increased. It seems that as the initial interelectrode gap increased, the

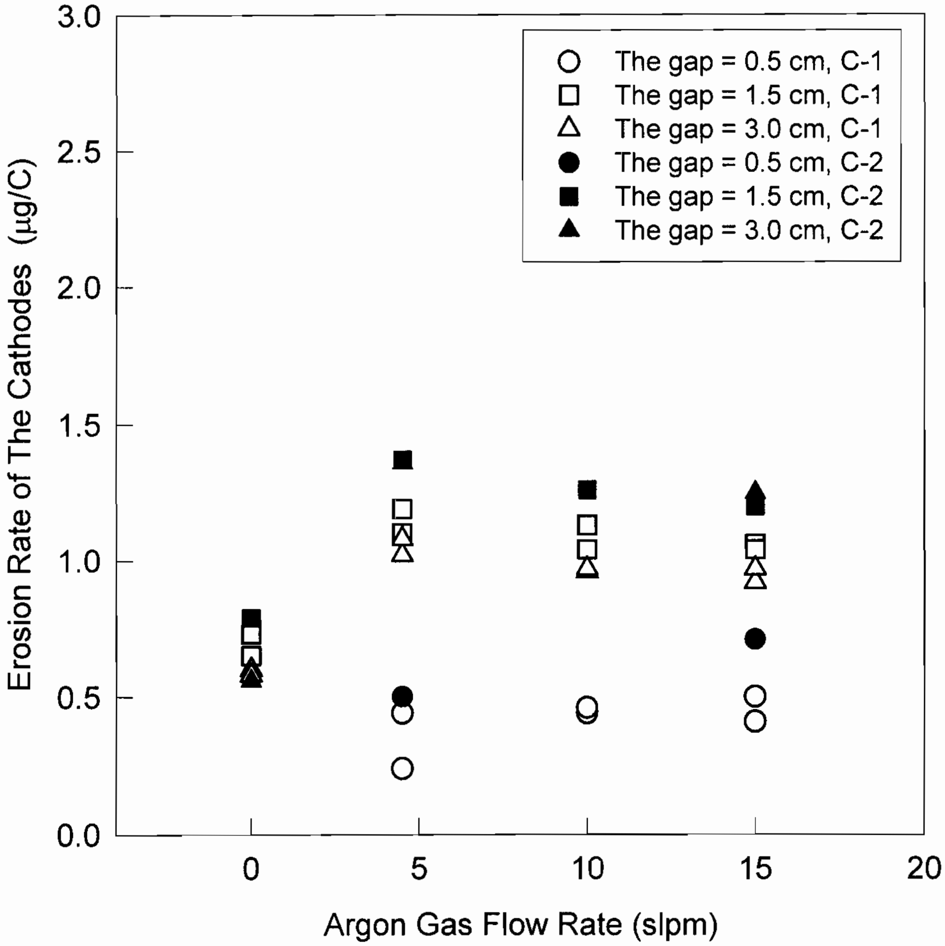

Figure 6-50: Comparison of the erosion rates between cathode I and II for an arc duration of 30 minutes at 300 A. C-1 stands for cathode I and C-2 is for cathode II.

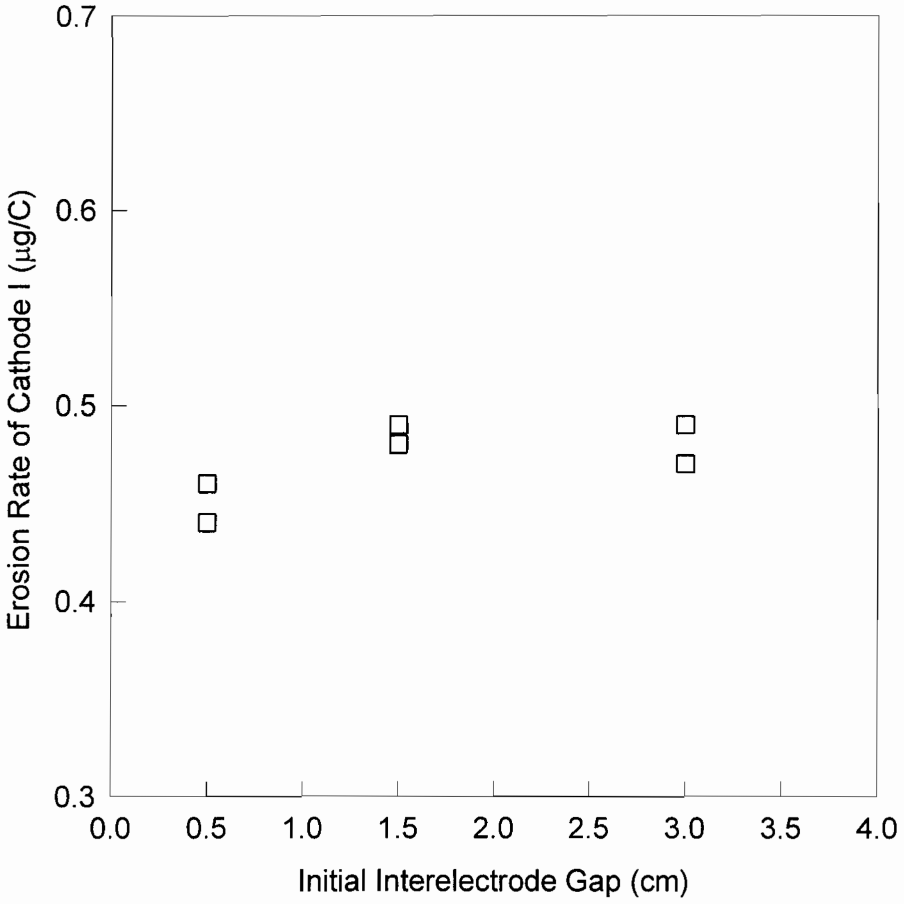

Figure 6-51: Erosion rate of cathode I as a function of the initial interelectrode gap for an argon gas flow rate of 15 slpm, an arc current of 150 A, and an arc duration of 120 minutes.

erosion rate might be affected by two factors: reduction of the carbon vapor redeposition and increase of graphite particles ejection due to the arc movement. Between them, probably the influence of the redeposition of the carbon vapor on the erosion rates was greater. The difference between the minimum and the maximum erosion rates was 0.05 μg/C at the 150 A runs. For the 300 A runs, the difference was much greater, i.e. 0.65 μg/C (see Figure 6-52). It is believed that the big difference between the 150 A runs of 0.05 μg/C and the 300 A runs of 0.65 μg/C was especially due to the redeposition of the carbon vapor for the initial interelectrode gap of 0.5 cm at 300 A. In case of the run at 0.5 cm and 300 A, the redeposition, providing the lowest erosion rate for the 300 A runs, was higher because heat flux to the anode was higher, thus resulting in relatively stronger anode graphite vapor jets.

6.3.3. Effect of Arc Current on Erosion Rate

Figure 6-53 presents the erosion rates as a function of the arc current for an argon gas flow rate of 15 slpm and an initial interelectrode gap of 1.5 cm. These operating conditions were selected for the discussion of this effect because the arc cathode operation mode was the same, i.e. the thermionic emission regime. As the arc current increased, the erosion rates also increased. This was expected because higher arc currents increase the heat flux to the thermionic spot, thus causing the higher erosion rates. This is a well-known phenomenon and is reflected in the traditional empirical models, prepared using graphite electrodes of EAFs, to represent erosion rates as a function of arc currents as discussed in chapter II.

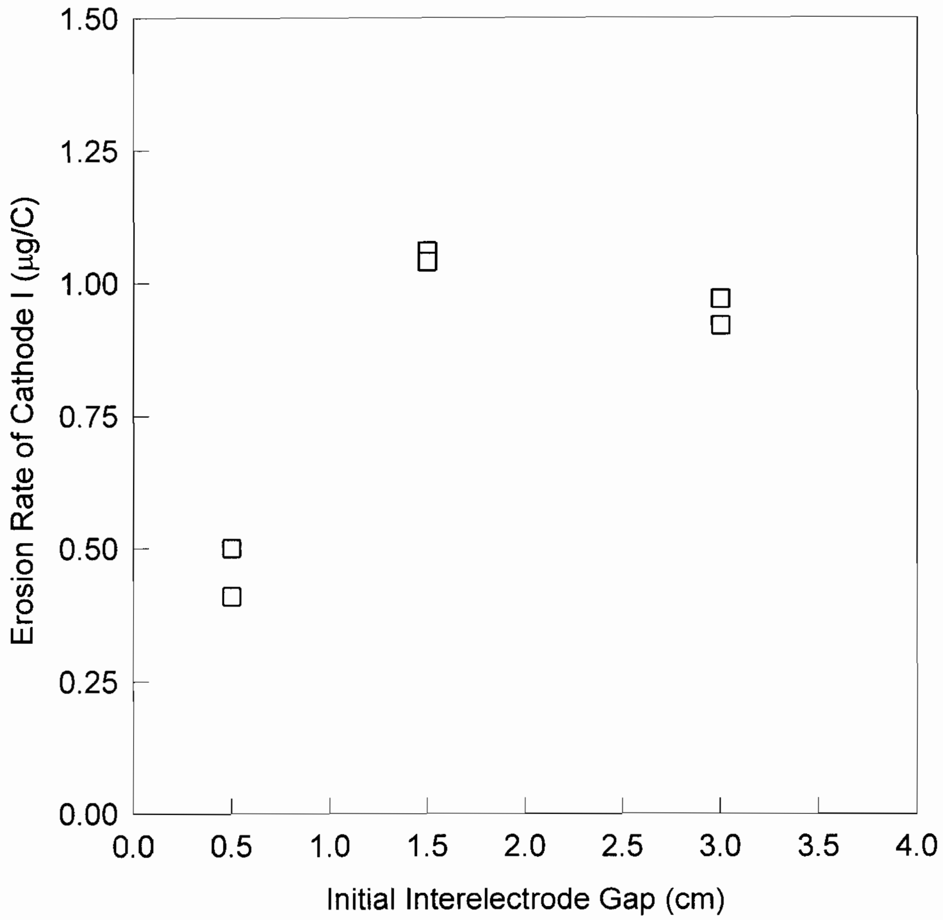

Figure 6-52: Erosion rate of cathode I as a function of the initial interelectrode gap for an argon gas flow rate of 15 slpm, an arc current of 300 A, and an arc duration of 30 minutes.

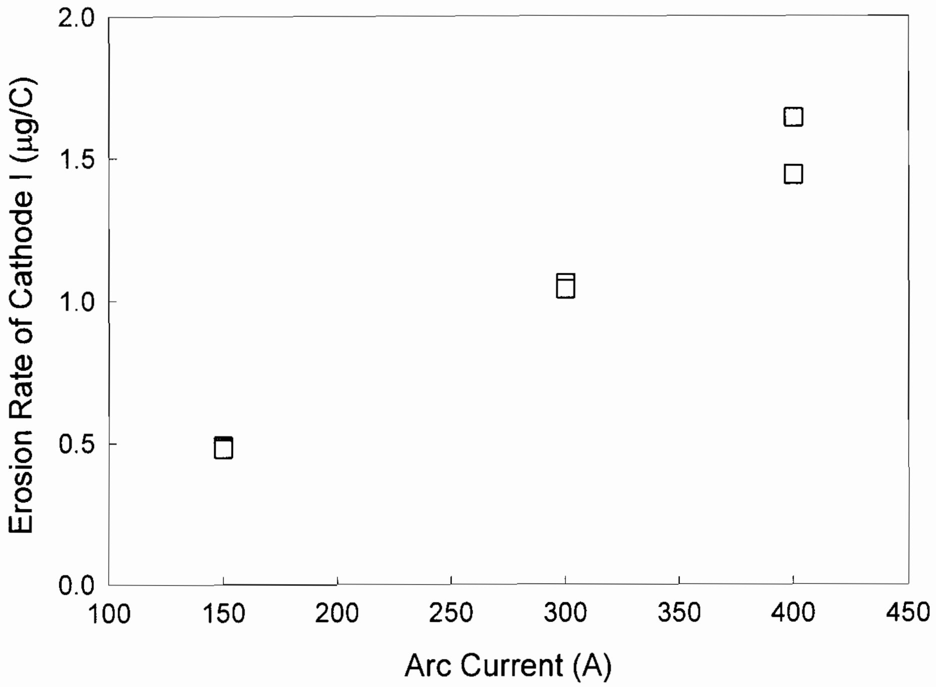

Figure 6-53: Erosion rates of cathode I as a function of the arc current for an argon gas flow rate of 15 slpm, an initial interelectrode gap of 1.5 cm, and an arc duration of 120 minutes for 150 A and 30 minutes for 300 and 400 A.

6.3.4. Effect of The Arc Stability on Erosion Rate

In the previous parts, it was shown that the erosion rates including the unstable arc runs were higher. This means that the arc stability, i.e. the arc cathode operation mode, influenced the erosion rates. In this part, a relationship between the arc stability and the erosion rates is derived, Then, the erosion rates are separated into the stable and the unstable erosion rate to study the effect of the arc stability on the erosion rates. The erosion rates measured for argon gas flow rates of 0 and 4.5 slpm at 150 A were used to investigate this effect because these runs included both the stable and the unstable arc operation. Even though the arcs for the same argon gas flow rate runs at 300 A displayed both the stable and the unstable parts, these erosion rates could not be used due to the strong redeposition of the carbon vapor.

The erosion rates were separated into the stable erosion rate (E_s) and the unstable erosion rate (E_u) using the following mass balance:

Total mass loss of the cathode =
Mass loss of the cathode for the stable arc operation
+ Mass loss of the cathode for the unstable arc operation (6-2)

From the definition of the erosion rate in equation (4-4), the total mass change of the mass balance above can be written as follows:

$$M = E\,t\,I \qquad (6\text{-}3)$$

$$M_s = E_s\,t_s\,I \qquad (6\text{-}4)$$

$$M_u = E_u\,t_u\,I \qquad (6\text{-}5)$$

$$E\,t\,I = E_s\,t_s\,I + E_u\,t_u\,I \tag{6-6}$$

where M is the total mass loss of the cathode (μg); E is the total erosion rate for a whole run (μg/C); t is the total arc duration (seconds); I is the arc current (A); M_s is the mass loss of the cathode for a stable arc run (μg); E_s is the erosion rate for a stable arc run (μg/C); t_s is the arc duration for a stable arc run (seconds); M_u is the mass loss of the cathode for an unstable arc run (μg); E_u is the erosion rate for an unstable arc run (μg/C); t_u is the arc duration for an unstable arc run (seconds). Furthermore, because the arc current was constant, the equation (6-6) could be simplified as follows:

$$E\,(t_s+t_u) = E_s\,t_s + E_u\,t_u \tag{6-7}$$

where E is the total erosion rate for a whole run (μg/C); E_s is the erosion rate for a stable arc run (μg/C); t_s is the arc duration for a stable arc run (seconds); E_u is the erosion rate for an unstable arc run (μg/C); t_u is the arc duration for an unstable arc run (seconds).

Five cases of the separation of the erosion rates into the stable part erosion rate, E_s, and the unstable part erosion rate, E_u, were studied using equation (6-7). Table 6-4 outlines the operating conditions for sets of runs in which both the stable and the unstable regimes were encountered at 150 A. The time for the stable and the unstable operation was determined from the voltage data. The problem, which remained, was to determine E_s for the various operating conditions. For low stability conditions (case I to IV) the time for the stable operation was too short to allow accurate measurements to be made of E_s. The

Table 6-4: Operating conditions* for the separation of the erosion rates into E_s and E_u.

Case	EXP-NO.	Argon gas flow rate (slpm)	Initial interelectrode gap (cm)	Stable arc duration (minutes)	Unstable arc duration (minutes)
Case I	EXP-31	0	0.5	49.18	67.64
Case II	EXP-30	0	1.5	24.98	91.86
	EXP-37	0	1.5	46.86	69.97
Case III	EXP-29	0	3.0	48.50	48.81
	EXP-36	0	3.0	38.84	62.77
Case IV	EXP-10	4.5	1.5	44.94	71.87
	EXP-11	4.5	1.5	39.43	77.27
Case V	EXP-21	4.5	3.0	62.71	54.11
	EXP-22	4.5	3.0	73.11	43.71
	EXP-27	4.5	3.0	50.35	-
	EXP-28	4.5	3.0	59.42	27.28

*) Runs for an arc current of 150 A using cathode I

solution used was to measure E_s under the stable conditions, i.e. at the current of 150 A and an argon gas flow rate of 15 slpm and assumes that this same value could be used for lower argon gas flow rates. This information is summarized in Table 6-5. For case V, E_s was measured directly from a run, which was stable throughout (EXP-27, Table 6-4) by stopping the experiment as soon as the acoustic noise and the voltage increase were detected. Figure 6-54 shows the voltage pattern for that run. The results of the separation of the overall erosion rate into the stable and the unstable erosion rates are summarized in Table 6-6. It is clear that the unstable erosion rates were always much higher than the stable erosion rates. The higher erosion rates in the unstable arc operation means that the arcs in the thermofield emission regime eroded the cathode more.

Table 6-5: The stable part erosion rates*, E_S.

Case	EXP-NO.	Argon gas flow rate (slpm)	Initial Interelectrode gap (cm)	E (μg/C)	E_S (μg/C)
Case I	EXP-14	15	0.5	0.44	0.45
	EXP-16	15	0.5	0.46	
Case II	EXP-12	15	1.5	0.49	0.49
	EXP-13	15	1.5	0.48	
Case III	EXP-25	15	3.0	0.47	0.48
	EXP-26	15	3.0	0.49	
Case IV	EXP-12	15	1.5	0.49	0.49
	EXP-13	15	1.5	0.48	
Case V	EXP-27	4.5	3.0	0.61	0.61

*) Runs for an arc current of 150 A using cathode I

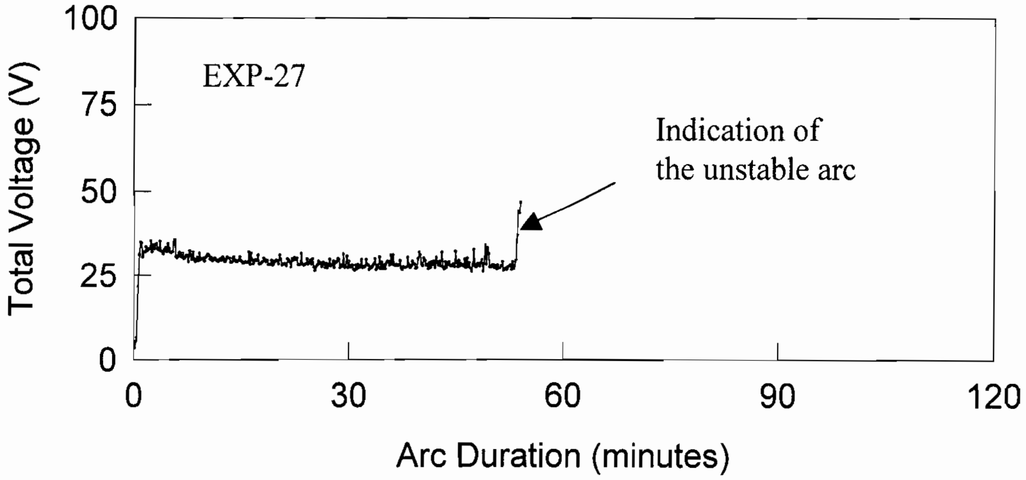

Figure 6-54: The voltage pattern for the experimental determination of E_S using cathode I for an argon gas flow rate of 4.5 slpm and an initial interelectrode gap of 3.0 cm at 150 A.

Table 6-6: The results of the separation of the erosion rates*.

Case	EXP-No.	Argon gas flow rate (slpm)	Initial interelectrode gap (cm)	E (μg/C)	E_s (μg/C)	E_u (μg/C)
Case I	EXP-31	0	0.5	0.62	0.45	0.74
Case II	EXP-30	0	1.5	2.61	0.49	3.19
	EXP-37	0	1.5	2.03		3.06
Case III	EXP-29	0	3.0	1.63	0.48	2.77
	EXP-36	0	3.0	1.36		1.91
Case IV	EXP-10	4.5	1.5	1.34	0.49	1.87
	EXP-11	4.5	1.5	1.11		1.43
Case V	EXP-21	4.5	3.0	1.57	0.61	2.68
	EXP-22	4.5	3.0	1.26		2.35
	EXP-27	4.5	3.0	0.61		0
	EXP-28	4.5	3.0	1.07		2.07

*) Runs for an arc current of 150 A using cathode I

The separate values of the E_u and the E_s are plotted as a function of the ΔV in Figure 6-55. The stable arc region ($\Delta V \leq 3$ V) is given as the open symbols; while the unstable arc region ($\Delta V > 3$ V) is given by the black symbols. The values of E_s are clustered together and are always less than those of E_u. The values for unstable arcs show much more scatter both in E_u and ΔV; therefore, it was difficult to analyze the E_u behavior. However, it was thought that E_u increased as the ΔV increased. As discussed earlier, principally the higher local heat flux to the cathode spots in the thermofield emission might increase the erosion rates. Figure 6-56 presents the erosion rates separated as a function of the ΔV/V. Like Figure 6-55, the E_s are clustered together at the ΔV/V of 0.5 and the E_u are highly scattered.

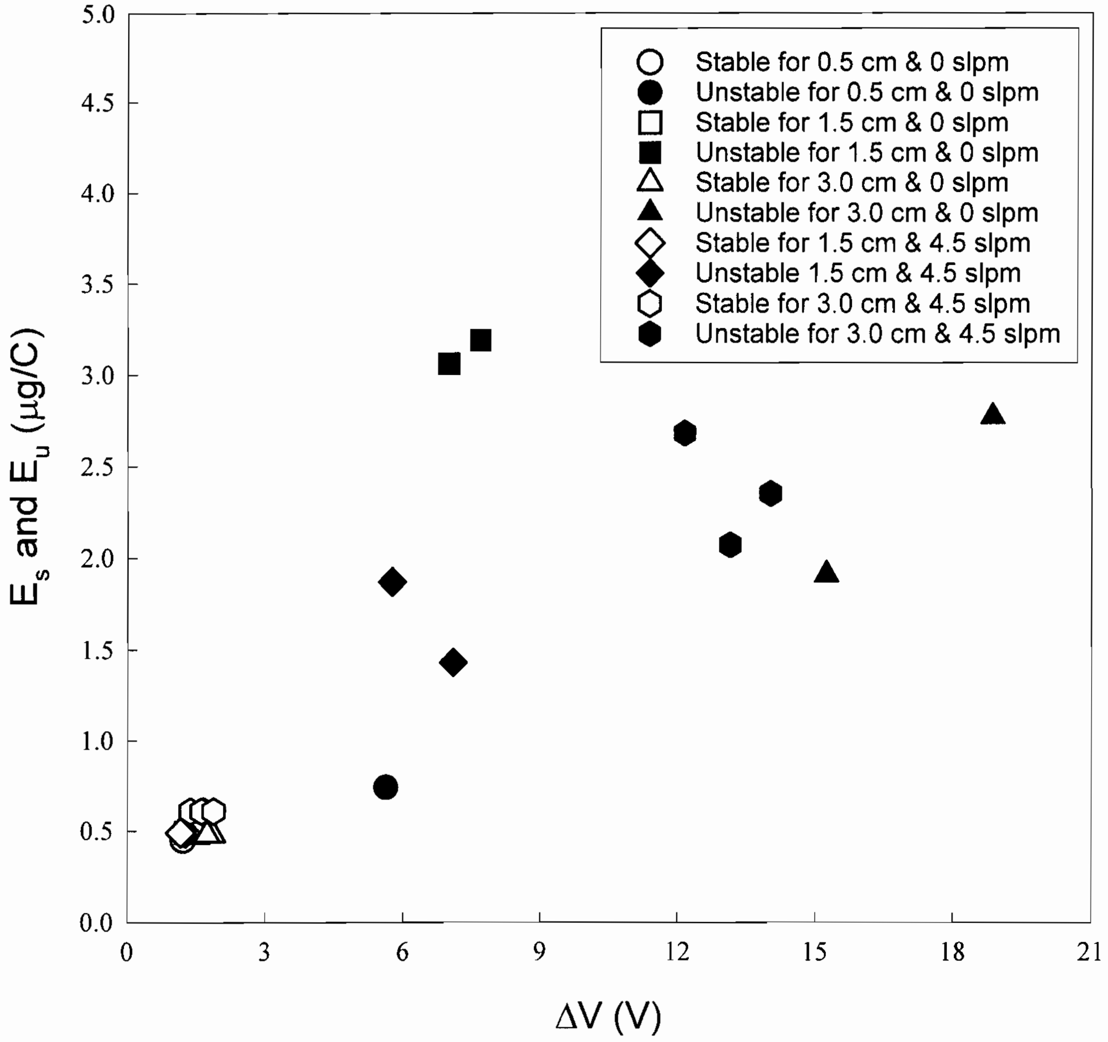

Figure 6-55: Stable part erosion rate (E_s) and unstable part erosion rate (E_u) as a function of ΔV using cathode I for an arc current of 150 A.

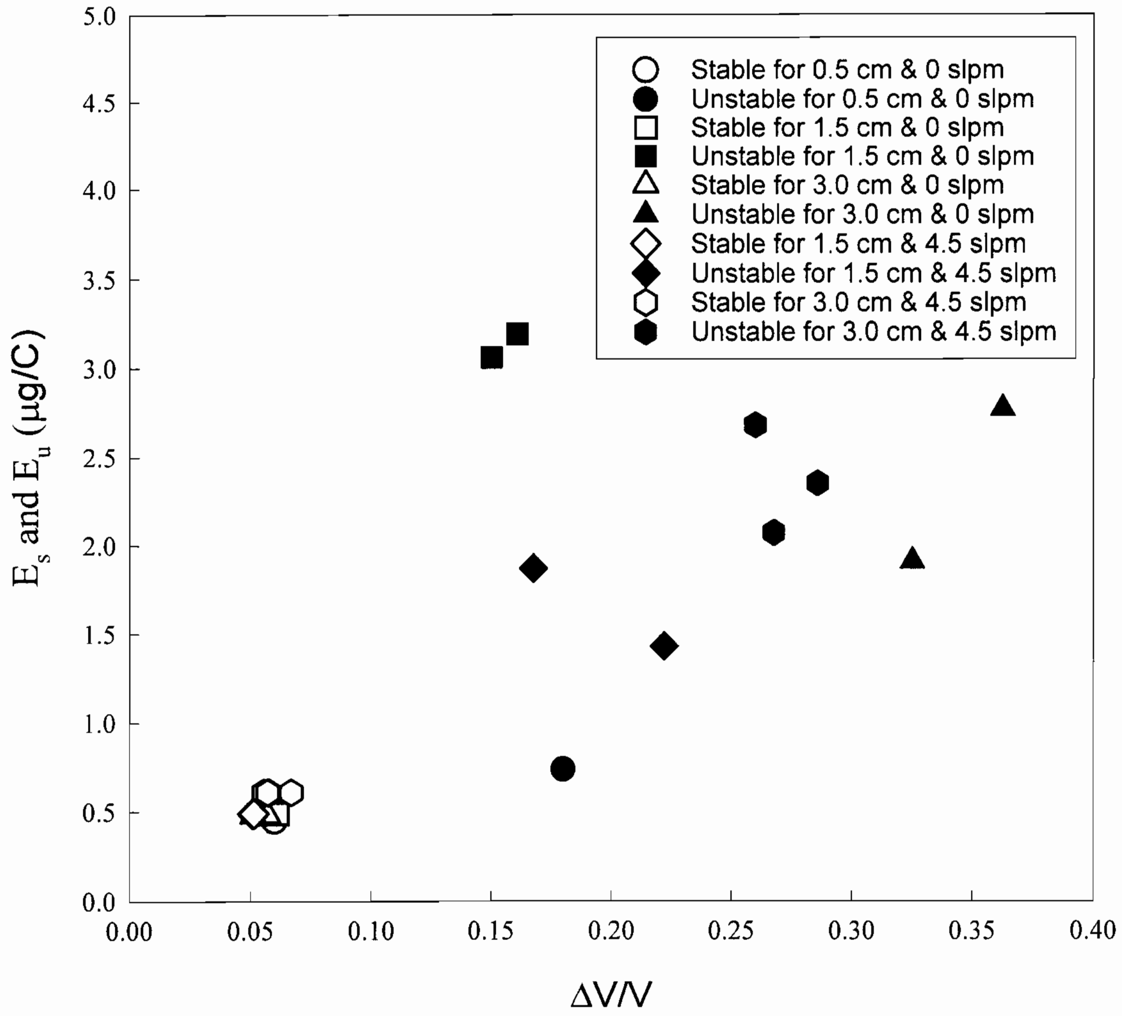

Figure 6-56: Stable part erosion rate (E_s) and unstable part erosion rate (E_u) as a function of ΔV/V using cathode I for an arc current of 150 A.

6.3.5. Comparison of Erosion Rates with Other Work

Erosion rates of this work were compared with those reported by Mentel (1977), Lefort et al. (1993), Drouet et al. (1995), and Neuschutz et al. (1996). The erosion rates of Mentel (1977), Lefort et al. (1993), and this work were obtained at the laboratory scale while the rates of Drouet et al. (1995) and Neuschutz et al. (1996) were obtained at the industrial operation. For this comparison the apparent current density was used primary because operating currents and cathode diameter varied greatly between the laboratory and industrial scale operation. The results are presented in Table 6-7 and procedures to estimate the rates are included in the notes of Table 6-7.

For the laboratory scale, the apparent current densities of Mentel (1977) are much greater than those of this work. The cathode II apparent current density of 375 A/cm^2, marked by **, in this work may be used to distinguish between the thermionic and the thermofield mode of graphite rod cathodes. The apparent current density of more than 375 A/cm^2 is able to indicate the thermionic mode of graphite rod cathodes because the runs at 0 slpm using cathode II in this work were always stable and were in the thermionic mode. For hollow graphite cathodes, however, the thermionic mode can be achieved even if the apparent current density is lower than 375 A/cm^2 due to argon gas injection. This suggests that the arc cathode operation mode of Mentel (1977), who used graphite rod cathodes, was in the thermionic emission regime. The erosion rates of this work and Mentel (1977) in the table were first compared because it was believed that they were in the same arc cathode operation mode, the thermionic emission mode, in argon. At 300 A the erosion rate of Mentel (1977) is higher, probably because of the higher current density. Also, the prevention of the carbon redeposition of Mental (1977) might contribute somewhat to the higher rate. The erosion rates of Mentel (1977) were correlated using the general form of the erosion rates of the graphite electrodes, introduced in chapter 2, as follows:

$$E = 7.5 \times 10^{-7} I^{2.7} \quad (6\text{-}8)$$

where E is the erosion rate (μg/C); I is the arc current (A). The erosion rates in this work were correlated as follows:

$$E = 1.4 \times 10^{-3} I^{1.2} \quad (6\text{-}9)$$

where E is the erosion rate (μg/C) ; I is the arc current (A). Lefort et al. (1993) reported much higher erosion rate than that of this work and even the rate of Mentel (1977) at 300 A. Since Lefort et al. (1993) did not provide information of the atmosphere of their operation, their rates may include some oxidation. Owing to the quite lower current and the current density of Lefort et al. (1993), their operation probably included the thermofield mode, leading to the higher erosion rate. In the table the highest unstable erosion rate of 3.2 μg/C in this work, marked by ***, is presented; the rate was estimated using only the unstable operation. The higher rate of Lefort et al. (1993) than 3.2 μg/C in this work supports the inclusion of the thermofield mode in their operation.

Direct comparison of the erosion rates between the laboratory and the industrial scale was difficult due to the different size of the cathodes and different operating conditions. Their arcs might include the thermionic mode despite operation of the industrial scale because Drouet et al. (1995) and Neuschutz et al. (1996) used argon for the arc stabilization.

Table 6-7: Comparison of erosion rates

	Current (A)	Cross-sectional area of the cathodes (cm^2)	Apparent current density (A/cm^2)	Erosion rates (μg/C)	Remarks
This work [1)]	150 *	2.8	54	0.5	Hollow cathode; Erosion
	300 *	2.8	107	1.1	
	400 *	2.8	143	1.5	
	300 **	0.8	375	1.2	
	150***	2.8	54	3.2	
Mentel (1977) [2)]	297	0.3	980	3.0	Rod cathode; Erosion
	594	0.3	1980	31.7	
	891	0.3	2970	66.7	
	1040	0.3	3467	85.7	
Lefort et al. (1993) [3)]	70	3.1	22	11.4	Rod cathode; Erosion
Drouet et al. (1995) [4)]	2500	81.7	31	85.6	Rod cathode; Consumption
Neuschutz et al. (1996) [5)]	2000	75.4	27	63.9	Hollow cathode; Consumption

Notes:

1) For cathode I, marked by *, the stable erosion rates of EXP-12, 13, 51, 52, 72, 73 operated at 1.5 cm and 15 slpm presented in Figure 6-53 were used; for cathode II, marked by **, the stable erosion rate of EXP-77 operated at 1.5 cm and 15 slpm was used; for the unstable erosion rate, marked by ***, the unstable rate of EXP-30 operated at 1.5 cm and 0 slpm using cathode I was used because the rate was the highest. The outer diameter was 1.91 cm for cathode I and was 1.07 cm for cathode II. The inner diameter was 0.32 cm for both cathodes.

2) The estimation of the erosion rates was introduced in Table 2-3. The diameter of the cathode was 0.615 cm.

3) The erosion rate reported was 0.8×10^{-6} kg/second; it was divided by the current of 70 A, and thus estimating the erosion rate of 11.4 μg/C. The diameter of the cathode was 2 cm.

4) The estimation of the rate was performed as follows. The diameter of the cathode was 10.2 cm.

① Electrode consumption per ton-dross reported: 0.88 kg/ton-dross

② Dross treatment capacity: 0.87 ton-dross/hour

③ Electrode consumption per hour: 0.77 kg/hour = 2.14×10^{-4} kg/second

④ At 2500 A, consumption is 86 μg/C

5) The estimation of the rate was performed as follows. The outer diameter of the cathode was 10 cm and the inner diameter of the cathode was 2 cm.

① Electrode consumption rate reported: 0.46 kg/hour = 1.28×10^{-4} kg/s

② At 2000 A, consumption is 64 μg/C

The rate of Neuschutz et al. (1996) at 2000 A is close to the rate of Mentel (1977) at about 900 A; the rate of Drouet et al. (1995) at 2500 A is about the same to the rate of Mentel (1977) at around 1000 A. Higher erosion rates than the rates of Mentel (1977) at about 900 ~ 1000 A were expected for the experiments of Drouet et al. (1995) and Neuschutz et al. (1996) due to higher currents and the oxidation of graphite. However, the rates of Drouet et al. (1995) and Neuschutz et al. (1996) are on the order of the rates of Mentel (1977) at about 900 ~ 1000 A. Probably this is due to the lower apparent current densities of Drouet et al. (1995) and Neuschutz et al. (1996). Compared with the rates of this work, their rates were much greater, because of much higher currents, the oxidation of graphite and possibly the thermofield mode resulting from the lower current densities.

CHAPTER VII

CONCLUSIONS AND RECOMMENDATIONS

7.1. CONCLUSIONS

1. Characteristics of Arcs at Hollow Graphite DC Cathode

The arc characteristics of the graphite cathode were studied as a function of initial interelectrode gap, argon gas flow rate, and arc currents. As the initial interelectrode gap increased, the total voltage also increased due to an increase of total resistance of the arcs. Higher argon gas flow rates slightly increased the voltage at lower interelectrode gap. At higher interelectrode gap, however, the effect of the argon gas flow rate on the voltage was negligible; it is believed that because of an increase of divergence of argon gas jets at the higher gap, less cooling of the arcs was caused and thus providing the very little effect on the voltage. The voltage increased slightly as the current increased. This voltage-current (V-I) characteristic showed that the arcs in this work are thermal arcs.

2. Arc Stability at a Hollow Graphite DC Cathode

The arc stability, i.e. the mode of the graphite arc cathode operation, was studied as a function of argon gas flow rate, initial interelecrode gap, arc currents, and cathode tip geometry. This mode transition is a spontaneous phenomenon of thermal arcs at the graphite cathode.

Two completely different total voltage patterns were observed. Arcs exhibiting a nearly constant voltage pattern were termed stable arcs. Arcs exhibiting noisy voltage patterns which coincided with rapid arc motion and acoustic noise were termed unstable arcs. It was hypothesized that the stable arcs were in thermionic emission and the unstable arcs were in thermofield emission. The mode transition from the thermionic emission to the thermofield emission occurred at rounder cathode tip geometry and lower argon gas flow rate. The hypothesis was supported by estimation of current densities, FFT of total voltage yielding time scales consistent with cathode spots for the thermofield emission for the unstable arcs, SEM evidence of cathode spots for the unstable arcs and crystal growth indicating higher mean temperature for the stable arcs, and measurements of cathode temperatures showing higher temperatures for the stable arcs.

3. Erosion Behavior of a Hollow Graphite DC Cathode

Erosion rates were measured of the graphite cathode using a graphite anode as a function of argon gas flow rate, initial interelectrode gap, and arc currents. As the argon gas flow rate increased, the erosion rate decreased at 150 A and increased at 300 A and 400 A. These opposite trends were due to the redeposition of the carbon vapor at higher arc currents. The redeposition reduced the erosion rate; especially at shorter initial interelectrode gap, lower argon gas flow rate, and higher arc currents.

Erosion rates of the cathode were strongly influenced by the arc stability at 150 A; as the arc stability increased, the cathode eroded at a lower rate. It is believed that in the thermofield emission regime of the unstable arc operation, the local heat flux to the cathode spots by the ion bombardment is higher, thus resulting in the more erosion of the graphite. The overall erosion rates were separated into stable (E_s) and unstable (E_u) erosion rate. The E_u was always higher than E_s and showed much more scatter.

Erosion of graphite electrodes can be controlled through regulating the arc stability.

Therefore, it is believed that the mode of graphite arc cathode operation may be selected to meet purposes of thermal arc processing using graphite electrodes.

7.2. CONTRUIBUTIONS TO KNOWLEDGE

The followings have been achieved as contributions to knowledge of this study:

1. Study of arc characteristics at a hollow graphite DC cathode.
2. Identification of the stable operation of the graphite cathode with thermionic emission and the unstable operation of the graphite cathode with thermofield emission.
3. Measurements of erosion rates of the graphite cathode using a graphite anode in argon at atmospheric pressure.

7.3. RECOMMENDATIONS FOR FUTURE WORK

The following experimental and theoretical studies are recommended as further work.

1. Arc Core Temperature

Both experimental and theoretical work is needed on arc core temperature as a function of argon gas flow rate. Spectroscopic methods and high speed video photography are believed to be viable techniques for the temperature and temperature distribution measurements.

2. Modeling of Arc Root Temperature

The measurement of arc root temperature is believed to be impractical with present technology; therefore, modeling work is believed to be a better approach to verify variation of the arc root temperature as a function of argon gas flow rate, interelectrode gap, and cathode tip geometry.

3. Experimental work at more than 1000 A for longer arc length is needed.

REFERENCES

Anders, S. and Anders, A., " On Modes of Arc Cathode Operation", IEEE Transactions on Plasma Science, Vol. 19, no. 1, February, pp. 20-24 (1991).

Anders, A. and Jütter, B., "Cathode Mode Transition in High-Pressure Discharge Lamps at Start-Up", Lighting Res. Technol., **22**, (2), pp. 111-115 (1990).

Barcza, N. A., "The Development of Large-Scale Thermal Plasma Systems", Journal of the South African Institute of Mining and Metallurgy, Vol. 86, no. 8, August, pp. 317-333 (1986).

Benilov, M. S., "Heating of Cathodes of High Pressure Arc Discharge", ISPC-14 Praha, Symposium Proceeding, Vol. 1, pp. 55-60 (1999)

Burkhard, R., Hoffelner, W., and Eschenbach, R.C., "Recycling of Metals from Waste with Thermal Plasma", Resources, Conservation and Recycling, Vol. 10, pp. 11-16 (1994).

Chen, G., "Vitrification of Simulated Medium and High Level Canadian Nuclear Waste in a Continuous Transferred Arc Plasma Melter", PhD Thesis, McGill University (1991).

Choi, Hyun-Koo, "Energy Distribution in Transferred-Arc System", PhD Thesis, McGill University (1981).

Cohn, D.R., "Hot and Cold Plasma Processing of Wastes", Selected Topics in Plasma Science and The Environment, edited by Manheimer, W., Sugiyama, L.E., and Stix, T.H., AIP Press, Woodbury, NY, USA, pp. 209-229 (1997).

Coulombe, S., "A Model of the Electric Arc Attachment on Non-Refractory Cold Cathodes", PhD Thesis, McGill University (1997).

Coulombe, S. and Meunier, J.-L., "Thermo-Field Emission: A Comparative Study", J. Phys. D: Appl. Phys. 30, pp. 776-780 (1997).

Coulombe, S. and Meunier, J.-L., "Importance of High Local Cathode Spot Pressure on the Attachment of Thermal Arcs on Cold Cathodes", IEEE Trans. on Plasma Sci., Vol. 25, no. 5, pp. 913-918 (1997).

Counts, D.A., Sartwell, B.D., Peterson, S.H., Kirkland, R., and Kolak, N.P., "Thermal Plasma Waste Remediation Technology: Historical Perspective and Current Trends", US Naval Research Laboratory, NRL/MR/6170-99-8335 (1999).

Desaulniers-Soucy and Meunier, J.-L., "A Study of Magnetically Rotating Arc Stability Using Fluctuations in Voltage, Velocity and Emission Line Intensity", J. Phys. D: Appl. Phys. 28 pp. 2505-2513 (1995).

Dolan, W.W. and Dyke, W.P., "Temperature-and-Field Emission of Electrons from Metals", Physical Review, Vol. 95, no.2, pp. 327 (1954).

Drouet, M. G., Handfield, M., Meunier, J., and Laflamme, C.B., "Dross Treatment in a Rotary Arc Furnace with Graphite Electrodes", JOM, May, pp. 26-27 (1994).

Drouet, M.G., Meunier, J., Laflamme, C.B., Handfield, M.D., Biscaro, A., and Lemire, C., "A Rotary Arc Furnace for Aluminum Dross Processing", Proceedings of the International Symposium on Environmental Technology: Plasma Systems and Applications, Atlanta, GA, USA, October, Vol. II, pp. 539-548 (1995).

Eddy, T.L., "Treating Waste with PAM", JOM, October, pp. 20-21 (1999).

Encyclopedia of Chemical Technology, Kirk and Othemer Eds, Wiley, New York, USA, Vol. 4, pp. 609 (1980).

Encyclopedia of Chemical Technology, Kirk and Othemer Eds, Wiley, New York, USA, Vol. 4, pp. 1039-1040 (1992).

Fauchais, P. and Vardelle, A., "Thermal Plasmas", IEEE Transactions on Plasma Science, Vol. 25, no. 6, December, pp. 1258-1280 (1997).

Ghorui, S., Sahasrabudhe, S. N., Murthy, P. S. S., Das, A. K., and Venkatramani, N., "Experimental Evidence of Chaotic Behavior in Atmospheric Pressure Arc Discharge", IEEE Transactions on Plasma Science, Vol. 28, no. 1, February, pp. 253-260 (2000).

Guile, A.E., " Arc-Electrode Phenomena", Proc. IEE, IEE Reviews, Vol. 118, no. 9R, September, pp. 1131-1154 (1971).

Holm, R., "The Vaporization of the Cathode in the Electric Arc", Journal of Applied Physics, Vol. 20, July, pp. 715-716 (1949).

Holm, R., "Electric Contacts", Springer-Verlag New York, USA, pp. 423-438 (1967).

Holman, J.P., "Experimental Methods for Engineers", McGraw-Hill Inc., USA, pp 315-321 (1989).

Jurewicz, J.W., Lecture Notes of Thermal Plasma Technology, Plasma Technology Research Center (CRTP), McGill University and Sherbrooke University (1997).

Jütter, B., "Properties of Arc Cathode Spots", J. Phys. IV France, **7**, pp. C4-31-C4-45 (1997).

Jütter, B., "Nanosecond Displacement Times of Arc Cathode Spots in Vacuum", IEEE Transactions on Plasma Science, Vol. 27, no. 4, August, pp. 836-844 (1999).

Kaltenhauser, R. H. and Gimbel, F. M., "Coated Electrodes to Reduce Graphite Consumption", Electric Furnace Proceedings, pp. 285-290 (1983).

Kandah, M.I., "Particles Emission Control at Graphite Cathodes in Arc Ion Plating Deposition", PhD Thesis, McGill University (1997).

Kim, George, "The Effects of Low Pressure Nitrogen on Titanium Cathode Sources in TiN Arc-Ion Plating", PhD Thesis, McGill University (1995).

Kimblin, C. W., "Erosion and Ionization in the Cathode Spot Regions of Vacuum Arcs", Journal of Applied Physics, Vol. 44, no. 7, pp. 3074-3081 (1973).

Lefort, A., Parizet, M. J., El-Fassi, S. E., and Abbaoul, M., "Erosion of Graphite Electrodes", Journal of Physics D: Applied Physics, Vol. 26, pp. 1239-1243 (1993).

Lefrank, P. A., Supon, M. F. and Jesberger, T.J., "Performance Evaluation of Graphite Electrodes under Varying Conditions in a Modern Arc Furnace Shop", Electric Furnace Proceedings, pp 297-309 (1983).

Maddever, W.J. and Segsworth, R.S.,"The Influence of Gas Injection Arc Stabilization and Electrode Consumption in Electric Furnaces", Canadian-Metallurgical Quarterly, Vol. 15, no. 1, pp. 49-52 (1976).

Mehmetoglu, M. T., "Characteristics of a Transferred-Arc Plasma", PhD Thesis, McGill University (1980).

Mentel, J., "The Influence of Vaporization upon The Roots of A High Current Arc, Part I Different Forms of Vaporization in the Arc Roots", Applied Physics, Vol. 14, pp. 269-276 (1977).

Mentel, J., “The Influence of Vaporization upon The Roots of A High Current Arc, Part II Spectroscopic Determination of the Composition and Temperature of a Plasma in the Neighbourhood of a Graphite Cathode”, Applied Physics, Vol. 14, pp. 361-366 (1977).

Mentel, J., “The Influence of Vaporization upon The Roots of A High Current Arc, Part III Determination of the Vapour Temperature by Molecular Spectroscopy and Conclusions concerning the Arc-Root Instability”, Applied Physics, Vol. 15, pp. 179-183 (1978).

Meunier, J.-L. and Drouet, M.G., “Experimental Study of the Effect of Gas Pressure on Arc Cathode Erosion and Redeposition in He, Ar, and SF_6 from Vacuum to Atmospheric Pressure”, IEEE Transactions on Plasma Science, Vol. PS-15, no.5, October (1987).

Montgomery, R.W. and Sharp, C.M.H., ”The Effect of the Cathode Geometry on the Stability of Arcs”, J.Phys.D., Ser. 2, Vol. 2, pp. 1345-1348 (1969).

Murphy, E.L. and Good, R.H., “Thermion Emission, Field Emission, and The Transition Region”, Physical Review, Vol. 102, no. 6, pp. 1464-1473 (1956).

Neuschutz, D., “Plasma Processing of Dusts and Residues”, Pure & Applied Chemistry, Vol. 68, no. 5, pp. 1159-1165 (1996).

Neuschutz, D., Stadler, P., and Bebber, H.J., “Arc Heating in the Tundish with a Graphite Electrode in Comparison to a Metallic Plasma Torch”, Steel Research, Vol. 67, no. 11, pp. 475-478 (1996).

Ochs, T.L., Hartman, A.D., and Wright, J.B.,”Improved Arc Stability in Electric Furnace Steelmaking”, Iron and Steel Engineer, May, pp. 26-31 (1989).

Pfender, E., Boulous, M., and Fauchais, P., “Methods and Principles of Plasma Generation”, Plasma Technology in Metallurgical Processing, Iron and Steel Society, pp. 27-47 (1987).

Roine, A., “Outokumpu HSC Chemistry for Windows”, User’s Guide, Outokumpu Research (1994).

Roth, J.R., “Industrial Plasma Engineering”, I.O.P. Publishing, Philadelphia, PA, USA, pp. 352-390 (1995).

Rozelle, P.L., Baranski, J.P., Bitler, J.A., and Exide Corporation, “Introduction to Exide Corporation’s High Temperature Metals Recovery Systems”, Proceedings of the International Symposium on Environmental Technologies: Plasma Systems and Applications, Atlanta, GA, USA, October, Vol. II, pp. 561-582 (1995).

Schwabe, W.E., "The Mechanics of Consumption of Graphite Electrodes in Electric Steel Furnaces", Electric Furnace Proceedings, pp. 140-148 (1971).

Schumacher, R.F., “High-Temperature Vitrificatin of Low-Level Radioactive and Hazardous Wastes”, Proceedings of the International Symposium on Environmental Technologies: Plasma Systems and Applications, Atlanta, GA, USA, October, Vol. II, pp. 461-470 (1995).

Siemroth, P., Schülke, T., and Witke, T., “Microscopic High Speed Investigations of Vacuum Arc Cathode Spots”, IEEE Transactions on Plasma Science, Vol. 23, no. 6, December, pp. 919-925 (1995).

Sommerville, I.D., McLean, A., and Alcock, C.B., “Materials Processing in Plasma Furnaces Equipped with Graphite Electrodes”, Plasma Technology in Metallurgical Processing, Iron and Steel Society, pp. 89-101 (1987).

Szente, R.N., Munz, R.J., and Drouet, M.G., "Electrode Erosion in Plasma Torches", Plasma Chemistry and Plasma Processing, Vol. 12, no. 3, pp. 327-343 (1992).

Themelis, N.J. and Gauvin, W.H., "A Two-Wavelength Pyrometer for Temperature Measurements in Gas-Solids Systems", The Canadian Journal of Chemical Engineering, August, pp.157-161 (1962).

UIE, Electroheat Technologies Committee, and Plasma Processing Working Group, "Arc Plasma Processes; A Maturing Technology In Industry; UIE Arc Plasma Review", Chapter 8 (1988).

Wittle, J.K., Titus, C.H., Hamilton, R.A., Cohn, D.R., Smatlak, D.L., Woskov, P.P., Thomas, P., and Surma, J.E., "DC Graphite Arc Furnace and Diagnostic System for Soils", Hazardous Wastes and Hazardous Materials, Vol. 11, no. 1, pp. 237-248 (1994).

Zhou, X. and Heberlein, J., "Analysis of the Arc-Cathode Interaction of Free-Burning Arcs", Plasma Sources Sci. Technol. Vol. 3, pp. 564-574 (1994).

APPENDICIES

Appendix 1. Estimation of the mass loss of the graphite cathode due to the oxygen in the argon atmosphere of the chamber

Bases:

1) Oxygen concentration in the chamber: 0.1 volume %.
2) Relative humidity in the chamber: 1% at 20 °C.
3) Volume of the chamber: 40 liters.

1. Graphite consumption mass loss due to the oxygen

Step-1: Determination of the moles of the oxygen.

The oxygen volume: 0.04 liters.

The oxygen moles: 0.0017 moles from the ideal gas law.

Step-2: The mass loss due to the oxygen: 4.08×10^{-2} g from $2C + O_2 \rightarrow 2CO$.

- The mass loss may be zero because of the accuracy of the O_2 meter (± 0.5 volume %).

2. Graphite consumption mass loss due to the water vapor

Step-1: Obtain the vapor pressure of water at 20.0 °C from the steam table. The vapor pressure was 17.535 mm Hg.

Step-2: By using the definition of the RH, calculate the partial pressure of the water vapor in the chamber. The partial pressure of the water vapor was 0.17535 mm Hg.

Step-3: By using the definition of the molar humidity, calculate moles of the water vapor in the chamber per mole of dry air.

$$H_n = \frac{mole_{H2O}}{mole_{dryair}} = \frac{p_{H2O}}{P - p_{H2O}}$$

where P is the chamber pressure (760 mm Hg) and p_{H2O} is the partial pressure of the water vapor. The moles of the water vapor was 2.31 x 10^{-4} per mole of dry air.

Step-4: By using the relationship between the absolute humidity and the molar humidity, calculation of the mass of the water vapor, g per g of dry air.

$$H = H_n(\frac{18}{29})$$

The mass of the water vapor was 1.43 x 10^{-4} g per g of dry air.

Step-5: Estimation of the water mass in the chamber.

The mass of the water vapor is 1.43 X 10^{-4} x the mass of dry air. The mass of the dry air in the chamber (48.24 g) was obtained using the ideal gas law. The mass of the water vapor was 6. 90 X 10^{-3} g (3.83 X 10^{-4} moles).

Step-6: The mass loss due to the water vapor: 4.60 x 10^{-3} g from $C + H_2O \rightarrow H_2 + CO$.

3. The mass loss of the graphite cathode due to the oxygen: 4.60 x 10^{-3} ~ 4.54 x 10^{-2} g.

Appendix 2. Operating Conditions

EXP NO.	Relative Humidity and Temperature (%)	(˚C)	O_2 Concentration (volume %)	Total Arc Duration (minutes)	Initial Interelectrode Gap (cm)	Argon Gas Flow Rate (slpm)	Remarks
150 A Experiments (Cathode I, EXP 1 ~ EXP 40)							
EXP-1	-	-	0.40	30.00	1.50	10.00	
EXP-2	-	-	0.40	60.00	1.50	10.00	
EXP-3	-	-	0.40	90.00	1.50	10.00	
EXP-4	-	-	0.20	30.00	1.50	10.00	
EXP-5	-	-	0.20	60.00	1.50	10.00	
EXP-6	-	-	0.20	90.00	1.50	10.00	
EXP-7	-	-	0.20	30.00	1.50	10.00	
EXP-8	-	-	0.20	120.00	1.50	10.00	
EXP-9	-	-	0.20	120.00	1.50	10.00	
EXP-10	-	-	0.20	120.00	1.50	4.50	
EXP-11	-	-	0.20	120.00	1.50	4.50	
EXP-12	-	-	0.20	120.00	1.50	15.00	
EXP-13	-	-	0.20	120.00	1.50	15.00	
EXP-14	-	-	0.20	120.00	0.50	15.00	
EXP-15	-	-	0.10	95.00	0.50	15.00	RF Interference
EXP-16	-	-	0.20	120.00	0.50	15.00	
EXP-17	-	-	0.20	120.00	0.50	10.00	
EXP-18	-	-	0.20	120.00	0.50	10.00	
EXP-19	-	-	0.20	120.00	0.50	4.50	
EXP-20	-	-	0.20	120.00	0.50	4.50	
EXP-21	-	-	0.30	120.00	3.00	4.50	
EXP-22	-	-	0.40	120.00	3.00	4.50	

EXP NO.	Relative Humidity and Temperature		O$_2$ Concentration	Total Arc Duration	Initial Interelectrode Gap	Argon Gas Flow Rate	Remarks
	(%)	(°C)	(volume %)	(minutes)	(cm)	(slpm)	
EXP-23	-	-	0.30	120.00	3.00	10.00	
EXP-24	-	-	0.30	120.00	3.00	10.00	
EXP-25	-	-	0.20	120.00	3.00	15.00	
EXP-26	-	-	0.20	120.00	3.00	15.00	
EXP-27	-	-	0.10	54.00	3.00	4.50	
EXP-28	0.90	20.80	0.10	90.00	3.00	4.50	
EXP-29	0.90	20.30	0.10	100.00	3.00	0.00	Self-Extinguished
EXP-30	0.70	20.70	0.10	120.00	1.50	0.00	
EXP-31	0.60	20.40	0.10	120.00	0.50	0.00	
EXP-32	0.70	20.60	0.10	84.00	3.00	4.50	Arcing
EXP-33	1.80	21.00	0.10	120.00	3.00	4.50/15.00	Changing AR
EXP-34	0.90	20.60	0.10	120.00	3.00	0.00	Anode Thread
EXP-35	0.90	20.80	0.10	60.00	3.00	4.50/15.00	Changing AR
EXP-36	0.80	20.70	0.10	105.00	3.00	0.00	Self-Extinguished
EXP-37	1.10	20.80	0.10	120.00	1.50	0.00	
EXP-38	0.70	20.80	0.10	120.00	0.50	0.00	
EXP-39	1.00	20.90	0.10	180.00	0.5/3.0/0.5	0.00	Changing Gap
EXP-40	1.30	20.50	0.10	120.00	0.50	0.00	
300 A Experiments (Cathode I, EXP 41 ~ EXP 68)							
EXP-41	1.30	20.70	0.10	30.00	1.50	10.00	
EXP-42	1.20	20.90	0.10	30.00	1.50	10.00	
EXP-43	1.30	20.50	0.10	60.00	1.50	10.00	
EXP-44	1.40	21.00	0.10	60.00	1.50	10.00	
EXP-45	0.90	20.20	0.10	10.00	1.50	10.00	

EXP NO.	Relative Humidity and Temperature (%)	(˚C)	O_2 Concentration (volume %)	Total Arc Duration (minutes)	Initial Interelectrode Gap (cm)	Argon Gas Flow Rate (slpm)	Remarks
EXP-46	0.90	20.70	0.10	10.00	1.50	10.00	
EXP-47	1.00	20.80	0.10	30.00	1.50	0.00	
EXP-48	1.00	20.50	0.10	30.00	1.50	0.00	
EXP-49	0.90	20.90	0.10	30.00	1.50	4.50	
EXP-50	0.80	20.90	0.10	30.00	1.50	4.50	
EXP-51	1.30	20.70	0.10	30.00	1.50	15.00	
EXP-52	1.20	20.80	0.10	30.00	1.50	15.00	
EXP-52-1	0.90	20.30	0.10	3.00	0.50	0.00	3 Minutes Run
EXP-53	1.30	22.70	0.10	30.00	0.50	4.50	
EXP-54	1.40	21.10	0.10	30.00	0.50	4.50	
EXP-55	1.90	20.80	0.10	30.00	0.50	10.00	
EXP-56	1.40	20.80	0.10	30.00	0.50	10.00	
EXP-57	1.40	20.80	0.10	30.00	0.50	15.00	
EXP-58	1.70	20.80	0.20	30.00	0.50	15.00	
EXP-59	1.50	21.10	0.10	30.00	3.00	0.00	
EXP-60	2.10	20.70	0.10	30.00	3.00	0.00	
EXP-61	1.30	20.70	0.20	30.00	3.00	4.50	
EXP-62	2.10	20.60	0.20	30.00	3.00	4.50	
EXP-63	2.00	20.40	0.20	30.00	3.00	10.00	
EXP-64	1.90	20.90	0.20	30.00	3.00	10.00	
EXP-65	1.70	20.40	0.20	30.00	3.00	15.00	
EXP-66	1.90	20.60	0.20	30.00	3.00	15.00	
EXP-67	1.50	20.60	0.10	40.00	3.00	4.50	
EXP-68	0.80	20.70	0.10	60.00	3.00	4.5/15/4.5	Changing AR

EXP NO.	Relative Humidity and Temperature (%)	(˚C)	O_2 Concentration (volume %)	Total Arc Duration (minutes)	Initial Interelectrode Gap (cm)	Argon Gas Flow Rate (slpm)	Remarks
400 A Experiments (Cathode I, EXP 69 ~ EXP 73)							
EXP-69	1.60	21.20	0.10	21.50	1.50	0.00	
EXP-70	1.20	21.20	0.10	30.00	1.50	0.00	
EXP-71	1.30	21.00	0.10	30.00	1.50	0.00	
EXP-72	1.10	20.80	0.10	30.00	1.50	15.00	
EXP-73	1.70	21.10	0.10	30.00	1.50	15.00	
300 A Experiments (Cathode II, EXP 74 ~ EXP 83)							
EXP-74	2.20	20.80	0.10	30.00	0.50	15.00	
EXP-75	1.30	21.10	0.10	30.00	0.50	4.50	
EXP-76	1.80	20.90	0.10	30.00	0.5/0.7	0.00	Changing Gap
EXP-77	2.30	21.10	0.10	30.00	1.50	15.00	
EXP-78	2.10	21.20	0.10	30.00	1.50	10.00	
EXP-79	2.10	20.50	0.10	30.00	1.50	4.50	
EXP-80	1.20	20.80	0.10	30.00	1.50	0.00	
EXP-81	2.60	21.30	0.10	30.00	3.00	0.00	
EXP-82	2.20	21.20	0.10	30.00	3.00	4.50	
EXP-83	2.80	21.30	0.10	30.00	3.00	15.00	
300 A Experiments (Cathode I, EXP 84)							
EXP-84	1.40	21.30	0.10	60.00	3.00	4.50	

Appendix 3. Erosion Rate of The Graphite Cathode

EXP NO.	Arc Duration (minutes)	Arc Current (A)	Mass Change of The Graphite Cathode			Erosion Rate (μg/C)
			Before EXP (g)	After EXP (g)	Mass Change (g)	
EXP-1	30.00	147.66	130.96	130.77	0.19	0.71
EXP-2	60.00	148.64	131.07	130.79	0.28	0.52
EXP-3	90.00	149.18	130.78	130.39	0.39	0.48
EXP-4	30.00	147.95	130.85	130.70	0.15	0.56
EXP-5	60.00	149.32	131.30	131.01	0.29	0.54
EXP-6	90.00	149.06	131.53	131.12	0.41	0.51
EXP-7	30.00	146.12	132.16	132.01	0.15	0.57
EXP-8	120.00	147.20	131.03	130.52	0.51	0.48
EXP-9	120.00	147.25	131.00	130.49	0.51	0.48
EXP-10	120.00	147.81	130.98	129.55	1.43	1.34
EXP-11	120.00	147.27	131.14	129.96	1.18	1.11
EXP-12	120.00	147.97	132.13	131.61	0.52	0.49
EXP-13	120.00	147.29	130.30	129.79	0.51	0.48
EXP-14	120.00	148.06	131.00	130.53	0.47	0.44
EXP-16	120.00	147.23	131.47	130.98	0.49	0.46
EXP-17	120.00	147.03	131.89	131.39	0.50	0.47
EXP-18	120.00	147.72	130.91	130.42	0.49	0.46
EXP-19	120.00	148.41	131.28	130.76	0.52	0.49
EXP-20	120.00	147.05	130.75	130.22	0.53	0.50
EXP-21	120.00	148.59	131.28	129.60	1.68	1.57
EXP-22	120.00	146.50	131.28	129.95	1.33	1.26
EXP-23	120.00	147.08	131.35	130.80	0.55	0.52
EXP-24	120.00	148.57	131.15	130.58	0.57	0.53

EXP NO.	Arc Duration (minutes)	Arc Current (A)	Mass Change of The Graphite Cathode			Erosion Rate (μg/C)
			Before EXP (g)	After EXP (g)	Mass Change (g)	
EXP-25	120.00	147.37	131.10	130.60	0.50	0.47
EXP-26	120.00	147.82	131.12	130.60	0.52	0.49
EXP-27	54.00	147.79	132.03	131.74	0.29	0.61
EXP-28	90.00	146.70	131.63	130.78	0.85	1.07
EXP-29	100.00	146.25	131.04	129.61	1.43	1.63
EXP-30	120.00	146.70	132.04	129.28	2.76	2.61
EXP-31	120.00	147.22	131.65	130.99	0.66	0.62
EXP-34	120.00	145.54	130.60	129.46	1.14	1.09
EXP-36	105.00	145.94	131.34	130.09	1.25	1.36
EXP-37	120.00	145.38	130.79	128.67	2.12	2.03
EXP-38	120.00	149.07	130.90	130.76	0.14	0.13
EXP-40	120.00	149.26	130.92	130.61	0.31	0.28
EXP-41	30.00	299.56	131.14	130.53	0.61	1.13
EXP-42	30.00	299.85	130.80	130.24	0.56	1.04
EXP-43	60.00	300.41	131.01	129.80	1.21	1.12
EXP-44	60.00	300.07	131.53	130.39	1.14	1.06
EXP-45	10.00	301.98	130.50	130.31	0.19	1.05
EXP-46	10.00	302.48	131.72	131.47	0.25	1.38
EXP-47	30.00	297.91	130.92	130.57	0.35	0.65
EXP-48	30.00	298.80	131.35	130.96	0.39	0.73
EXP-49	30.00	299.26	131.47	130.83	0.64	1.19
EXP-50	30.00	298.53	130.14	129.55	0.59	1.10
EXP-51	30.00	299.64	130.53	129.96	0.57	1.06
EXP-52	30.00	298.09	130.51	129.95	0.56	1.04
EXP-53	30.00	301.46	131.86	131.73	0.13	0.24
EXP-54	30.00	299.89	130.98	130.74	0.24	0.44

EXP NO.	Arc Duration (minutes)	Arc Current (A)	Mass Change of The Graphite Cathode			Erosion Rate (μg/C)
			Before EXP (g)	After EXP (g)	Mass Change (g)	
EXP-55	30.00	300.16	130.50	130.26	0.24	0.44
EXP-56	30.00	300.40	131.47	131.22	0.25	0.46
EXP-57	30.00	300.38	131.03	130.81	0.22	0.41
EXP-58	30.00	300.65	131.73	131.46	0.27	0.50
EXP-59	30.00	297.89	131.43	131.11	0.32	0.60
EXP-60	30.00	298.98	130.83	130.52	0.31	0.58
EXP-61	30.00	294.22	130.87	130.33	0.54	1.02
EXP-62	30.00	293.05	131.13	130.56	0.57	1.08
EXP-63	30.00	295.81	131.00	130.49	0.51	0.96
EXP-64	30.00	297.14	132.15	131.63	0.52	0.97
EXP-65	30.00	294.51	130.93	130.44	0.49	0.92
EXP-66	30.00	297.35	132.23	131.71	0.52	0.97
EXP-67	40.00	292.57	130.87	130.02	0.85	1.21
EXP-69	21.50	388.69	131.21	130.84	0.37	0.74
EXP-70	30.00	386.95	130.81	130.27	0.54	0.78
EXP-71	30.00	387.89	130.50	129.95	0.55	0.79
EXP-72	30.00	386.47	131.73	130.73	1.00	1.44
EXP-73	30.00	383.76	131.42	130.29	1.13	1.64
EXP-74	30.00	298.46	46.13	45.75	0.38	0.71
EXP-75	30.00	299.70	46.31	46.04	0.27	0.50
EXP-77	30.00	296.41	46.42	45.78	0.64	1.20
EXP-78	30.00	299.13	45.72	45.04	0.68	1.26
EXP-79	30.00	296.05	43.85	43.12	0.73	1.37
EXP-80	30.00	297.06	46.17	45.75	0.42	0.79
EXP-81	30.00	295.32	46.33	46.03	0.30	0.56
EXP-82	30.00	298.00	46.24	45.51	0.73	1.36

EXP NO.	Arc Duration (minutes)	Arc Current (A)	Mass Change of The Graphite Cathode Before EXP (g)	After EXP (g)	Mass Change (g)	Erosion Rate (μg/C)
EXP-83	30.00	293.29	46.22	45.56	0.66	1.25
EXP-84	60.00	287.63	131.29	129.71	1.58	1.53

Appendix 4. Separation of The Overall ΔV into Stable and Unstable ΔV

EXP NO.	Arc Duration (minutes)	The Gap (cm)	AR Flow Rate (slpm)	Arc Current (A)	The Overall V & ΔV		Stable V, ΔV, ΔV/V, & Time				Unstable V, ΔV, ΔV/V, & Time			
					V (V)	ΔV (V)	V (V)	ΔV (V)	ΔV/V	s-time (minutes)	V (V)	ΔV (V)	ΔV/V	u-time (minutes)
EXP-1	30.00	1.50	10.00	147.66	24.76	0.99	24.76	0.99	0.04	26.88				
EXP-2	60.00	1.50	10.00	148.64	24.74	1.66	24.74	1.66	0.07	56.87				
EXP-3	90.00	1.50	10.00	149.18	17.64	1.16	17.64	1.16	0.07	86.98				
EXP-4	30.00	1.50	10.00	147.95	25.00	1.09	25.00	1.09	0.04	26.95				
EXP-5	60.00	1.50	10.00	149.32	24.80	2.48	24.80	2.48	0.10	56.90				
EXP-6	90.00	1.50	10.00	149.06	22.28	2.01	22.28	2.01	0.09	86.99				
EXP-7	30.00	1.50	10.00	146.12	24.59	1.02	24.59	1.02	0.04	26.92				
EXP-8	120.00	1.50	10.00	147.20	24.09	2.01	24.09	2.01	0.08	116.98				
EXP-9	120.00	1.50	10.00	147.25	25.35	1.61	25.35	1.61	0.06	116.97				
EXP-10	120.00	1.50	4.50	147.81	30.67	6.53	24.81	1.27	0.05	44.94	34.35	5.76	0.17	71.87
EXP-11	120.00	1.50	4.50	147.27	28.80	7.26	22.71	1.17	0.05	39.43	31.92	7.09	0.22	77.27
EXP-12	120.00	1.50	15.00	147.97	25.63	1.80	25.63	1.80	0.07	116.98				
EXP-13	120.00	1.50	15.00	147.29	25.30	1.65	25.30	1.65	0.07	116.97				
EXP-14	120.00	0.50	15.00	148.06	21.28	1.02	21.28	1.02	0.05	117.00				
EXP-15	95.00	0.50	15.00	145.32	21.82	1.01	21.82	1.01	0.05	66.13				
EXP-16	120.00	0.50	15.00	147.23	17.46	1.37	17.46	1.37	0.08	116.99				
EXP-17	120.00	0.50	10.00	147.03	22.86	2.44	22.86	2.44	0.11	116.86				
EXP-18	120.00	0.50	10.00	147.72	20.73	1.42	20.73	1.42	0.07	116.96				
EXP-19	120.00	0.50	4.50	148.41	19.13	2.63	19.13	2.63	0.14	116.98				
EXP-20	120.00	0.50	4.50	147.05	20.90	2.74	20.90	2.74	0.13	116.98				
EXP-21	120.00	3.00	4.50	148.59	34.83	13.64	24.80	1.38	0.06	62.71	46.45	12.15	0.26	54.11
EXP-22	120.00	3.00	4.50	146.50	35.90	13.41	27.99	1.62	0.06	73.11	49.09	14.03	0.29	43.71
EXP-23	120.00	3.00	10.00	147.08	28.57	3.07	27.55	1.41	0.05	79.69	30.73	4.29	0.14	37.31
EXP-24	120.00	3.00	10.00	148.57	32.10	3.51	30.77	1.38	0.04	76.87	34.64	4.76	0.14	39.95
EXP-25	120.00	3.00	15.00	147.37	29.67	2.12	29.67	2.12	0.07	116.99				
EXP-26	120.00	3.00	15.00	147.82	29.75	2.21	29.75	2.21	0.07	116.99				
EXP-27	54.00	3.00	4.50	147.79	29.00	1.66	29.00	1.66	0.06	50.35				
EXP-28	90.00	3.00	4.50	146.70	34.71	12.36	28.07	1.88	0.07	59.42	49.12	13.15	0.27	27.28
EXP-29	100.00	3.00	0.00	146.25	42.24	16.60	32.43	1.86	0.06	48.50	52.02	18.86	0.36	48.81
EXP-30	120.00	1.50	0.00	146.70	42.64	12.04	23.58	1.28	0.05	24.98	47.78	7.69	0.16	91.86
EXP-31	120.00	0.50	0.00	147.22	26.46	7.27	19.64	1.22	0.06	49.18	31.42	5.63	0.18	67.64

EXP NO.	Arc Duration (minutes)	The Gap (cm)	AR Flow Rate (slpm)	Arc Current (A)	The Overall V & ΔV		Stable V, ΔV, ΔV/V, & Time				Unstable V, ΔV, ΔV/V, & Time			
					V (V)	ΔV (V)	V (V)	ΔV (V)	ΔV/V	s-time (minutes)	V (V)	ΔV (V)	ΔV/V	u-time (minutes)
EXP-32	84.00	3.00	4.50	146.04	35.99	12.52	28.67	1.43	0.05	42.26	48.93	12.95	0.26	23.86
EXP-34	120.00	3.00	0.00	145.54	38.33	12.31	31.31	1.46	0.05	58.66	45.39	14.23	0.31	58.03
EXP-36	105.00	3.00	0.00	145.94	41.95	13.57	33.98	1.74	0.05	38.84	46.89	15.25	0.33	62.77
EXP-37	120.00	1.50	0.00	145.38	38.11	11.76	25.41	1.56	0.06	46.86	46.60	7.00	0.15	69.97
EXP-38	120.00	0.50	0.00	149.07	17.73	0.93	17.73	0.93	0.05	116.85				
EXP-40	120.00	0.50	0.00	149.26	19.38	2.01	19.38	2.01	0.10	116.99				
EXP-41	30.00	1.50	10.00	299.56	29.44	2.31	29.44	2.31	0.08	26.84				
EXP-42	30.00	1.50	10.00	299.85	29.97	2.80	29.97	2.80	0.09	27.34				
EXP-43	60.00	1.50	10.00	300.41	29.35	2.19	29.35	2.19	0.07	56.84				
EXP-44	60.00	1.50	10.00	300.07	28.68	2.84	28.68	2.84	0.10	56.84				
EXP-45	10.00	1.50	10.00	301.98	26.19	1.38	26.19	1.38	0.05	6.84				
EXP-46	10.00	1.50	10.00	302.48	26.69	2.25	26.69	2.25	0.08	6.84				
EXP-47	30.00	1.50	0.00	297.91	29.56	6.90	25.02	0.95	0.04	17.73	38.41	4.44	0.12	8.95
EXP-48	30.00	1.50	0.00	298.80	31.82	8.08	25.29	1.54	0.06	14.38	39.43	5.51	0.14	12.30
EXP-49	30.00	1.50	4.50	299.26	28.87	3.40	26.56	1.15	0.04	3.81	29.27	3.50	0.12	22.87
EXP-50	30.00	1.50	4.50	298.53	33.27	5.01	27.86	0.73	0.03	6.99	35.18	4.44	0.13	19.69
EXP-51	30.00	1.50	15.00	299.64	28.92	2.07	28.92	2.07	0.07	26.84				
EXP-52	30.00	1.50	15.00	298.09	27.85	1.86	27.85	1.86	0.07	26.84				
EXP-53	30.00	0.50	4.50	301.46	24.30	1.20	24.30	1.20	0.05	26.84				
EXP-54	30.00	0.50	4.50	299.89	22.62	1.29	22.62	1.29	0.06	26.84				
EXP-55	30.00	0.50	10.00	300.16	24.13	0.80	24.13	0.80	0.03	26.84				
EXP-56	30.00	0.50	10.00	300.40	24.04	0.66	24.04	0.66	0.03	26.84				
EXP-57	30.00	0.50	15.00	300.38	24.64	1.14	24.64	1.14	0.05	26.84				
EXP-58	30.00	0.50	15.00	300.65	25.52	0.81	25.52	0.81	0.03	26.84				
EXP-59	30.00	3.00	0.00	297.89	38.90	4.45					38.90	4.45	0.11	26.84
EXP-60	30.00	3.00	0.00	298.98	36.28	2.49	36.28	2.49	0.07	26.84				
EXP-61	30.00	3.00	4.50	294.22	40.28	6.62	35.18	1.37	0.04	12.30	44.59	6.23	0.14	14.38
EXP-62	30.00	3.00	4.50	293.05	39.84	7.28	34.84	1.50	0.04	13.09	44.84	7.33	0.16	13.09
EXP-63	30.00	3.00	10.00	295.81	36.07	3.06	34.97	1.57	0.04	19.22	38.82	4.03	0.10	7.46
EXP-64	30.00	3.00	10.00	297.14	35.78	4.77	33.41	1.45	0.04	13.92	38.20	5.69	0.15	13.76
EXP-65	30.00	3.00	15.00	294.51	32.95	2.61	32.95	2.61	0.08	26.84				
EXP-66	30.00	3.00	15.00	297.35	34.11	2.86	34.11	2.86	0.08	27.34				
EXP-67	40.00	3.00	4.50	292.57	39.74	8.26	33.07	1.64	0.05	16.44	45.03	7.53	0.17	20.74

EXP NO.	Arc Duration (minutes)	The Gap (cm)	AR Flow Rate (slpm)	Arc Current (A)	The Overall V & ΔV		Stable V, ΔV, ΔV/V, & Time				Unstable V, ΔV, ΔV/V, & Time			
					V (V)	ΔV (V)	V (V)	ΔV (V)	ΔV/V	s-time (minutes)	V (V)	ΔV (V)	ΔV/V	u-time (minutes)
EXP-69	21.50	1.50	0.00	388.69	33.41	7.74	27.16	0.85	0.03	10.21	41.38	4.61	0.11	7.97
EXP-70	30.00	1.50	0.00	386.95	33.83	6.72	26.66	0.68	0.03	6.71	36.27	6.07	0.17	19.97
EXP-71	30.00	1.50	0.00	387.89	32.66	5.99	27.42	1.02	0.04	13.35	37.60	4.28	0.11	13.83
EXP-72	30.00	1.50	15.00	386.47	30.15	1.87	30.15	1.87	0.06	27.34				
EXP-73	30.00	1.50	15.00	383.76	30.71	2.20	30.71	2.20	0.07	26.84				
EXP-74	30.00	0.50	15.00	298.46	28.12	0.60	28.12	0.60	0.02	27.34				
EXP-75	30.00	0.50	4.50	299.70	26.78	0.90	26.78	0.90	0.03	27.84				
EXP-77	30.00	1.50	15.00	296.41	32.67	0.81	32.67	0.81	0.02	26.84				
EXP-78	30.00	1.50	10.00	299.13	33.48	0.84	33.48	0.84	0.03	27.34				
EXP-79	30.00	1.50	4.50	296.05	33.75	0.90	33.75	0.90	0.03	27.34				
EXP-80	30.00	1.50	0.00	297.06	32.16	1.93	32.16	1.93	0.06	27.34				
EXP-81	30.00	3.00	0.00	295.32	42.92	2.30	42.92	2.30	0.05	27.34				
EXP-82	30.00	3.00	4.50	298.00	42.16	1.41	42.16	1.41	0.03	27.34				
EXP-83	30.00	3.00	15.00	293.29	38.70	1.30	38.70	1.30	0.03	26.84				
EXP-84	60.00	3.00	4.50	287.63	48.92	12.94	34.42	1.57	0.05	12.42	52.98	11.75	0.22	44.76

Note: The Definition of Standard Deviation

$$s = \left[\frac{1}{n-1} \sum_{i=1}^{n} \left(x_i - \bar{x} \right)^2 \right]^{0.5}$$

where s is the standard deviation; n is the number of the data; x_i is the data; $\bar{x}$ is the average of the data.